Dropwise Condensation in Refrigerants: Experimental Setup Design

Setup Design and Verification for Estimating the Heat Transfer Coefficient in Dropwise Condensation

Master Thesis

Ruben Caan

Delft University of Technology

TU Delft

Dropwise Condensation in Refrigerants: Experimental Setup Design

Setup Design and Verification for Estimating the Heat Transfer Coefficient in Dropwise Condensation

by

Ruben Caan

to obtain the degree of Master of Science

at the Delft University of Technology,

to be defended publicly on Monday January 22, 2026 at 10:00 AM.

Student number:	5169178	
Project duration:	April 23, 2025 – January 22, 2026	
Thesis committee:	Dr. E. Zanetti,	TU Delft, daily supervisor, chair
	Prof. dr. K. Hooman,	TU Delft
	Prof. dr. R. Pecnik,	TU Delft

Cover: Condensate Droplets on a Lubricant Infused Surface (Modified) [1].

An electronic version of this thesis is available at http://repository.tudelft.nl/.

TU Delft

Abstract

Fluorinated refrigerants, widely used in refrigeration cycle applications, cause significant greenhouse gas emissions. In view of reducing environmental impact, natural refrigerants are applicable as an alternative. However, their imposed risks (flammability, toxicity & high pressure systems) raise safety concerns. These refrigeration cycle applications utilize a condensation process. By increasing the heat transfer coefficient, the damage potential can be reduced by decreasing the size of the condenser in its applications. Dropwise condensation has proven to significantly enhance the heat transfer coefficient relative to traditional filmwise condensation in steam applications. However, little research is conducted into the experimental heat transfer coefficient of dropwise condensation in refrigerants. Therefore, a setup is designed to estimate the heat transfer coefficient experimentally on different promoter layers. For derivative estimation, the total heat transfer rate, condensation wall temperature, and saturation temperature are needed. The optimal solution available to estimate these parameters is based on Fourier's law of conduction in a designed test-section. Here, condensation takes place on one side and cooling on the other, causing heat transfer and a temperature gradient. By measuring the temperature at different points, the total heat transfer rate and wall temperature can be estimated. To supply saturated vapour, a pressurised loop is designed, including an evaporator, post-condenser, pump and coolant supply. While verifying the function of the test-section in a computational model, the resulting performance align with expectations. However, the one-dimensional model for estimation the heat transfer coefficient based on Fourier's law of conduction, is not sufficient in accurately estimating the wall temperature. A temperature gradient occurs on the condensation surface, whereas the estimation-model assumes a homogenous temperature. Therefore, the heat transfer coefficient of condensation will be severely underestimated at increased saturation and coolant temperatures.

Preface

Welcome to the beginning of my thesis. This work represents the result of both academic and personal development throughout my studies and concludes my student career. From a young age, I was deeply fascinated by large construction machinery, a curiosity which eventually led me to Mechanical Engineering and later to specialize in Process and Energy. This was driven by my growing interest in developing engineering solutions for environmental and emission-related challenges. Therefore, I am motivated to apply my engineering skills to contribute to ongoing efforts addressing these global issues.

This research focuses on reducing the climate impact of refrigerants by enhancing the heat transfer coefficient of their condensation processes, eventually reducing safety concerns for climate friendly alternatives. This work aims to improve the understanding and experimental expertise of dropwise condensation, thereby contributing to safer and more effective applications of natural refrigerants. Researching this topic proved to be both challenging and rewarding; while gaining a fundamental understanding of the underlying physical mechanisms required effort, transferring this knowledge into a (real-life) experimental setup was satisfying. These efforts represent steps toward estimating the heat transfer coefficient during dropwise condensation of natural refrigerants.

Without the contributions of many individuals, this thesis would not have been possible. I would like to sincerely thank my supervisor, Dr. E. Zanetti, whose guidance, availability, thoughtful feedback shaped this work. I am grateful for his trust and continued investment throughout the project. I also wish to thank the lab supervisor, Gert-Jan, for his encouragement, humour, and invaluable assistance with the practical and logistical aspects design. Special thanks to the lab technicians -Daniel, Martijn, Bart, Michel and Bart- for their work during the construction of experimental components and for their enjoyable communication. I am also thankful to Qu and Zhaopeng for their guidance in the experimental measurments. Special thanks to Maarten for his thorough feedback on the report. Most importantly, I thank my partner, Selma, for her unwavering patience and belief in my abilities. I am deeply grateful to my family for their continuous support, and to my friends, who made my student life both memorable and enjoyable.

Statement about the use of AI:LLM: To comment on the honesty of my work, I want to make a short statement about the usage of Artificial Intelligence (AI), specifically Large Language Models (LLM): LLMs were used to assist in the generation and structuring of python scripts for numerical calculations and plotting, only after the relevant physical models and governing equations were independently derived and determined by me. Moreover, LLMs were employed to explore new approaches to the topic when progress was limited, and to assist me in finding alternative sentence structures or synonyms in this report. All academic reasoning, approaches, decisions and interpretation of results remain entirely my own responsibility.

Ruben Caan
Delft, January 2026

Contents

List of Figures

List of Tables

Nomenclature

Abbreviations

Abbreviation	Definition
CA	Contact angle
CFC	Chlorofluorocarbons
DWC	Dropwise Condensation
EU	European Union
FQLS	Fluorinated quasi-liquid surface
FWC	Filmwise Condensation
GWP	Global warming potential
HCFC	Hydrochlorofluorocarbon
HCFO	Hydrochlorofluoroolefin
HFC	Hydrofluorocarbon
HFO	Hydrofluoroolefin
HTC	Heat transfer coefficient
HVAC	Heating, ventilation and air-conditioning
LIS	Lubricant infused surface
NCG	Non-condensible gasses
ODP	Ozone-depletion potential
PID	Proportional-integral-derivative
P&ID	Process & instrumentation diagram
PTFE	Polytetrafluoroethylene
RC	Refrigeration cycle
SEM	Scanning electron microscope

Symbols

Symbol	Definition	Unit
A	Area	$[\mathrm{m}^2]$
c_p	Specific heat at constant pressure	$[\mathrm{J}/(\mathrm{kg\,K})]$
c_v	Specific heat at constant volume	$[\mathrm{J}/(\mathrm{kg\,K})]$
D	Diameter	$[\mathrm{m}]$
g	Gravitational constant	$[\mathrm{m}/\mathrm{s}^2]$
HTC	Heat transfer coefficient	$[\mathrm{W}/(\mathrm{m}^2\,\mathrm{K})]$
h	Heat transfer coefficient	$[\mathrm{W}/(\mathrm{m}^2\,\mathrm{K})]$
h_{fg}	Latent heat of vapourisation	$[\mathrm{J}/\mathrm{kg}]$
Ja	Jacob number	[-]
k	Thermal conductivity	$[\mathrm{W}/(\mathrm{m\,K})]$
L	Length	$[\mathrm{m}]$
m	Mass	$[\mathrm{kg}]$
$\dot{m}$	Mass flow rate	$[\mathrm{kg}/\mathrm{s}]$
n	Droplet size distribution smaller than effective radius	[-]
N	Droplet size distribution larger than effective radius	[-]
Nu	Nusselt number	[-]
P	Pressure	$[\mathrm{bar}]$, $[\mathrm{Pa}]$

Symbol	Definition	Unit
q	Heat flux	$[\mathrm{W/m}]$
$\dot{Q}$	Heat transfer rate	$[\mathrm{W}]$
R	Thermal resistance	$[\mathrm{K/W}]$
r	Radius	$[\mathrm{m}]$
Re	Reynolds number	[-]
t	Time	$[\mathrm{s}]$
T	Temperature	$[^\circ\mathrm{C}]$, $[\mathrm{K}]$
U	Internal energy	$[\mathrm{J/kg}]$
U	Overall heat transfer coefficient	$[\mathrm{W/(m^2\,K)}]$
u	Uncertainty	[-]
x	Variable	[-]
Greek		
α	Inclination angle	$[^\circ]$
γ	Interfacial surface energy	$[\mathrm{J/m^2}]$
γ	Free surface energy	$[\mathrm{mJ/m^2}]$
Γ	Mass flow per unit width	$[\mathrm{kg/(s\,m)}]$
δ	Promoter layer thickness	$[\mathrm{m}]$
δ	Film thickness	$[\mathrm{m}]$
ε	Error	[-]
θ	Contact angle	$[^\circ]$
μ	Dynamic viscosity	$[\mathrm{Pa\,s}]$
ν	Kinematic viscosity	$[\mathrm{m^2/s}]$
ρ	Density	$[\mathrm{kg/m^3}]$
Φ	Heat transfer rate	$[\mathrm{W}]$
Sub/super-script		
$\prime$	Modified	
$\bar{}$	Averaged	
a	Advancing	
atm	Atmospheric	
$coolant$	coolant	
D	Droplet	
e	Effective	
F	Free	
$film$	Film	
g	Gas	
i	Index	
l	Liquid	
max	Maximum	
min	Minimum	
N	End of index	
net	Net	
P	Pressure	
r	Receding	
rod	Rod	
s	Solid	
sat	At saturation	
$surface$	Surface	
T	Temperature	
tot	Total	
v	Vapour	
w	Wall	

P&ID symbols

Symbol	Definition
CF	Charge fitting
CV	Check valve
EH	Electrical heater
ES	(Electrical) Energy sensor
HV	Hand valve
LS	Level sensor
PCD	Post condenser
PI	Pressure indicator
PP	Pump
PS	Pressure sensor
RV	Relief valve
TB	Thermal bath
TK	Tank
TS	Temperature sensor
VF	Vacuum fitting

1

Introduction

The relevancy of the topic of experimental dropwise condensation will be introduced in this chapter. The general background of this research will be explained in Section 1.1, by giving societal and theoretical background to dropwise condensation and its development potential regarding refrigerant-legislation. Moreover, the research gab is found and the associated research objectives are listed in Section 1.2. Then the outline of this thesis and secondary products are shortly discussed in Section 1.3.

1.1. Background

Condensation is a heat transfer process in which a fluid transitions from vapour to liquid, releasing energy in the process. It is a fundamental process in a wide spread of applications, such as desalination, power plants, cooling of electronics, refrigeration, and heating, ventilation and air-conditioning (HVAC) [2]. In refrigeration and HVAC systems, a vapour compression refrigeration cycle (RC) is utilized to transfer heat from a low temperature heat source to a high temperature heat sink. Condensation is where the energy is released from the working fluid to the heat sink.

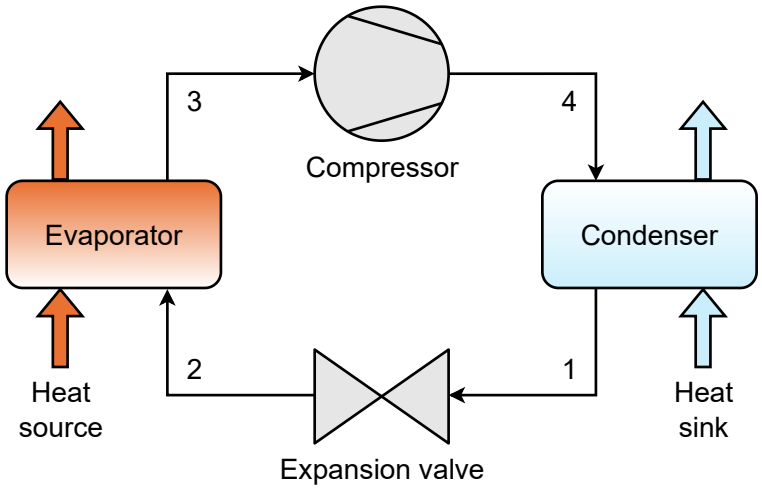

Figure 1.1: Schematic of a refrigeration cycle: (1) High pressure liquid, expanded to (2) low pressure liquid; Then evaporated by taking energy from the heat source to (3) low pressure vapour which is compressed to raise the saturation temperature in (4) high pressure vapour. This is then condensed by rejecting energy to the heat sink to return to (1) high pressure liquid (adapted from [3, 4]).

Figure 1.1 shows such a refrigeration cycle. Depending on the temperatures of the heat source and sink, a suitable working fluid, referred to as a refrigerant, is applied [5]. Historically, whichever refrigerant suited was applied, the emphasis on safety and durability was introduced later, giving rise to

synthetic substances[6, 7]. Such refrigerants are chlorofluorocarbons (CFCs), hydrochlorofluorocarbon (HCFCs) & hydrofluorocarbons (HFCs). However, these proved to cause ozone-layer depletion and were consequently banned globally under the Montreal-protocol (1987) and the Kyoto-protocol (1997). Temporary substitutes also fall within CFCs, HCFCs & HFCs, while these cause significantly less ozone depletion, they have a high global warming potential (GWP) [8, 7].

As of 2017, such fluorinated refrigerants were responsible for 7.8% of the global greenhouse gas emissions. 37% of this are direct emissions of these substances into the environment, while the rest are indirect emissions (e.g. transport, manufacturing) [9]. Therefore many legislators are restricting the use of these harmful refrigerants [10]; the European Union (EU) is phasing CFCs, HCFCs & HFCs out completely and transitioning to substances with a low GWP [11, 12].

Table 1.1: Historic events related to the use of (synthetic) refrigerants [6, 7, 8, 9, 10, 11, 12].

Event	Year/period	Explanation
First use of refrigerants	1800s	During this time they used which ever fluid worked and was available. Most fluids were toxic, flammable, and/or highly reactive.
Synthetic refrigerants	1930s	Shifting to fluoro-chemicals to enhance safety, durability and performance. Giving rise to CFCs and later HCFCs.
Montreal & Kyoto Protocols	1987	Due to proven Ozone Layer depletion, CFC refrigerants were banned. Temporary substitutes, like HCFC & HFC, are scheduled to be phased out by the years 2020-2030 & 2025-2040 respectively.
GWP legislation	2024	Due to causing significant global greenhouse gas emissions, legislators (such as EU) are phasing out refrigerants with a high global warming potential by 2050. Thereby shifting back to natural refrigerants and the associated risks like toxicity, flammability, and high pressure systems.

The historic context is summarized in Table 1.1. The future requires replacement refrigerants to be applied in (existing) refrigeration and HVAC systems. Alternative substances must have a very low ozone-depletion potential (ODP), be chemically stable within a system, have low toxicity, and be compatible with the materials of the system [13]. Viable options are: (1) HFCs with low GWP; (2) hydrofluoroolefins (HFOs) and hydrochlorofluoroolefins (HCFOs); or (3) natural refrigerants [10, 14]. However, requirements of the next-generation refrigerants may be conflicted. As substances with low GPW and no ODP may be toxic (ammonia), flammable (hydrocarbons), or require high working pressures (CO_2), thus raising safety concerns [7, 13, 15, 16, 17].

To increase the safety of existing systems or systems in development, the amount of refrigerant in the system (i.e., charge) can be reduced. However, to achieve this, the thermal conductance of the heat transfer process needs to increase, for example by increasing the heat transfer coefficient (HTC). As an increased HTC allows for less heat transfer area for the same heat transfer, thereby reducing the amount fluid needed to fill the heat exchanger. Not only does this save refrigerant, but also heat exchanger material, making the overall system more compact. Thus, increasing the HTC will lead to safer, smaller, and cheaper refrigeration and HVAC systems.

In a condenser two distinct modes of condensation on a cooled surface are possible (Figure 1.2), filmwise condensation (FWC) and dropwise condensation (DWC)[18]. In FWC, vapour is condensed on the surface and the condensate flows down. Here, a film of liquid condensate is created, completely wetting the surface [19]. If the surface has been treated so the condensate does not wet the surface [20], DWC can occur, as firstly reported by Schmidt et al. [21]. Here an increase in HTC was reported of 5-7 fold when compared to FWC. Others reported an order of magnitude increase over FWC when

applying DWC properly [22]. Given DWC's great potential in condensation processes, many scholars have consequently researched its theory [23, 24], developed models [22, 25, 26], and conducted experiments [27, 28, 29].

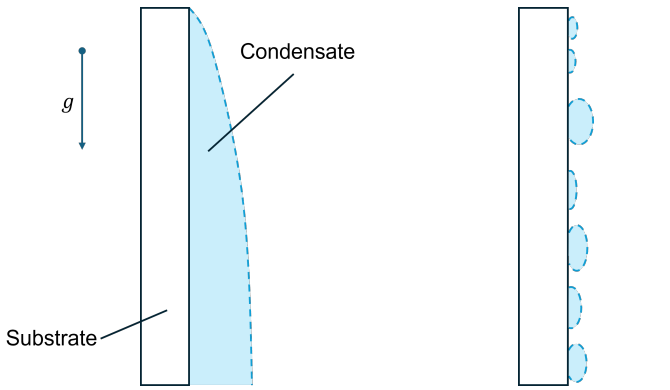

(a) Filmwise condensation **(b)** Dropwise condensation

Figure 1.2: Visualization of condensation modes on a vertical surface (adapted from Khan et al. [30]).

As DWC does not form a continuous liquid film on the surface as in FWC [31], the thermal resistance is reduced, thereby increasing the HTC [19]. Instead, droplet growth starts on a molecular level with drop formation at nucleation sites. As condensation continues, the drops grow and coalescence until a critical size is reached. When external forces are greater than the adhesion forces and the drops depart of the surface. While departing, they clean the surface in their tracks, clearing nucleation sites and allowing renewal of the process (cyclic process) [2, 18, 32].

Depending on the substrate, DWC can be promoted with a non-wetting coating or nanostructures on the surface [2]. This alters the free surface energy between the surface and liquid condensate, preferably resulting in a three-phase contact angle above 90° [33]. Some factors that influence DWC are, among others, nucleation site density, departure rate, and the presence of non-condensible gasses (NCGs) [32].

El Fil et al. [2] summarized the current research on DWC and concluded the following. Theories about the mechanism of DWC are comprehensive, and it can be modelled if the relevant condensate and surface properties are known. Also, many scholars conducted experiments on the matter, finding various HTCs. However, the majority of studies are focussed on steam as the working fluid. This has a high surface tension, which helps by achieving DWC. The HTC in steam condensation is already high, therefore the need for DWC is questionable. Condensation processes of refrigerant and hydrocarbons have lower HTCs, and should therefore benefit from enhanced HTC provided by DWC [32]. Consequently, the safety of systems with natural refrigerants can be enhanced by reducing the required fluid charge.

1.2. Research objectives

From the background presented above, it is concluded that research into dropwise condensation of refrigerants is needed to enhance safety by reducing refrigerant charge of refrigeration and HVAC systems. Obtaining the HTC of refrigerants in DWC is of crucial importance for the design of safer systems. Therefore the main research question of this work formulated as:

"What is the optimal solution to experimentally estimate the heat transfer coefficient of a (dropwise) condensation process of a refrigerant?"

To answer the main research question, the following sub-questions have been formulated to be answered in the process:

1. What equipment is needed to facilitate an experimental estimation of the heat transfer coefficient of condensation?
2. How can the setup be verified and how is the heat transfer coefficient estimated?

3. What are assumptions and inputs into modelling dropwise condensation?
4. How can the contact angle of the chosen refrigerant be measured?

1.3. Research outline

In the next chapters, the main research question and its sub-questions will be answered. This is written in the following outline. First the topic of DWC is extensively researched in literature and summarized in Chapter 2. This will give insight in the theory, modelling, and factors that enhance DWC. Additionally, it will show that limited experimental research has been conducted and its results. Then, in Chapter 3, the design for an experimental setup to estimate the HTC in DWC of a refrigerant is discussed. Here, several options are explored and the optimal for the requirements is chosen and its design is shown in detail. Chapter 4 describes the methodology for measuring the contact angle of water on experimental surfaces, the verification of the setup with the help of computational modelling, and one dimensional estimation of the HTC and its uncertainty. After this, Chapter 5 goes into the results of the static and dynamic contact angle measurements, the verification of the setup and the uncertainty analysis. Then, the results are extensively discussed in Chapter 6. From which recommendations for further research will follow in Chapter 7. Finally, Chapter 8 concludes this work.

2

Literature review

This chapter summarizes all relevant literature about DWC for this thesis. First different theories on the mechanism of DWC are discussed in Section 2.1. Next droplet shapes on the surface are shown in Section 2.2. Then the steps in modelling the HTC in FWC is shown in Section 2.3. Whereafter the approach(s) in modelling DWC are discussed in Section 2.4. Then favourable surface properties for achieving DWC are shown in Section 2.5. More general enhancement factors of the HTC in DWC are elaborated on in Section 2.6. Lastly, advancements in achieving DWC and enhancing the HTC in refrigerants is discussed in Section 2.7.

2.1. Dropwise condensation theories

In DWC, the drops naturally occur on the cooled surface. After they have grown to a critical size, the drops depart of the surface, taking other droplets with them. Now the surface is free and new drops can form and the cycle repeats [2, 18, 32]. This process starts on nano- to microlevel, different theories exists about the precise mechanism of the creation of droplets on the surface:

- Film break-up theory: This describes vapour condensation in filmwise mode, forming a very thin film. When a critical thickness is reached, the film ruptures due to interfacial instabilities and small droplets form. Here droplets are solely seen as liquid carriers, as condensation only occurs on the cooled surface [2, 33].
- Nucleation sites theory: Drops form similarly to vapour bubbles in boiling, in a nucleation process. Nucleation sites are randomly distributed among the surface. Here the initial condensation can occur, forming nano-size independent droplets on the cooled surface. The condensation process continues on the droplet surface, allowing the drops to grow. When a critical size is reached, the drops begin to coalesce and depart [2, 19, 20, 33].
- Adsorption theory: Yongji et al. [29] suggested a theory that combines the nucleation site theory and the existence of a thin film on the cooled surface. Heat transfer occurs at the surface of the drops and on the bare surface, resulting in drop growth. Drops can form at the nucleation sites and adsorb the liquid from the condensate film. This allows the drops to grow and eventually depart once a critical size is reached. This theory has now been accepted by a large number of academics [33].

Several scholars conducted experimental research into the mechanisms of dropwise condensation. McCormick and Westwater [34] concluded, with the help of photographic evidence, that drops repeatedly nucleated on certain spots on the surface. These spots were cavities, solid nanoparticles, erosion pits, scratches and other nano surface variations. Thus supporting the nucleation site theory.

Umur and Griffith [27] concluded that there is no observable liquid film on the surface between the drops. Thereby also supporting the nucleation site theory. However, this only excludes the existence of an observable monolayer, a nanofilm may still exist.

As argued by Kim and Kim [22] and Khandekar and Muralidhar [19], after initial nucleation, a droplet grows due to direct condensation on the droplet surface, adsorption of the liquid surface film and coalescence with other drops. The drops are held together by capillary forces and are subject to gravity. Once the drop has grown to a critical size, where the body forces are greater than the capillary forces, the drop starts to depart. Depending on the fluid, the surface, and its inclination, the critical size varies [33].

2.2. Droplet Morphology

The shape of a droplet (morphology) on the surface is strongly dependent on the surface energy difference between the substrate and the fluid. The contact angle is the result of this difference and can be determined for an ideal surface as [2]:

$$\cos\theta = \frac{\gamma_{s,g} - \gamma_{s,l}}{\gamma_{l,g}} \tag{2.1}$$

Here, γ is the interfacial surface energy, in $[\mathrm{J}/\mathrm{m}^2]$. Its subscript denotes the interface between which phases; l is for liquid phase, s is for solid phase, g is for gaseous phase.

Generally, the state of condensation is dependent on the balance between surface tension forces, thus the contact angle (θ) between the surface and the interface of the drop. FWC is preferred on surfaces where the contact angle is less than 90° ($\theta < 90°$). DWC can develop on surfaces if the contact angle is greater than 90° ($\theta > 90°$) [22, 33].

In DWC on an inclined surface, gravity is constantly pulling the liquid drops down. This is resisted by the adhesion of the droplet to the surface. However, as a result of the inclination angle (α) two distinct angles exist: the receding contact angle (θ_r) shows where the droplet moves away and the advancing contact angle (θ_a) shows where the droplet advances over the surface. All angles (Figure 2.1) are a result of the adhesion to the surface, and are therefore factors in determining the wetting of the surface and critical departure size of the drop [2, 19, 32, 33].

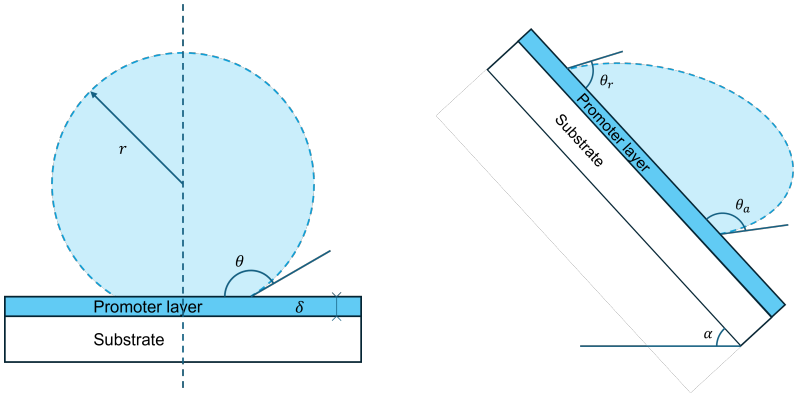

(a) Flat surface **(b)** Inclined surface

Figure 2.1: Visualization of droplet contact angles between the surface and the fluid interface (adapted from Hu et al. [33]).

The receding and advancing angle are by rule different. The fact that such a distinction and difference exists is referred to as the contact angle hysteresis ($\Delta\theta$). This, is mathematically defined as the difference between the contact angle at the advancing side and the receding side ($\Delta\theta = \theta_a - \theta_r$)[35]. Physically, the hysteresis shows how 'sticky' the droplet is to the surface as a consequence of the surface inhomogeneity, surface roughness & surface impurities [19]. A low hysteresis means that the droplet moves more easily over the surface.

When a droplet exists on a real surface (non-smooth), the roughness of the surface influences the wetting properties. Wenzel [36] argued that drops can be fully emerged in the nanostructures on the surface, referred to as the Wenzel-state. He related the apparent contact angle to this surface roughness and the normal contact angle. Cassie and Baxter [37] found that drops can rest on top of nanos-

tructures on the surface, referred to as the Cassie-state, and this can results in an increased contact angle.

Between the Wenzel- and Cassie-state, partial wetting exists. Here the drop partly rests on the nanostructures but also wets the cavities beneath. The different morphologies are shown in Figure 2.2. Partial wetting and the Cassie-state are more favourable for drop departure, as the adhesion forces are smaller than the Wenzel-state [2, 19, 33].

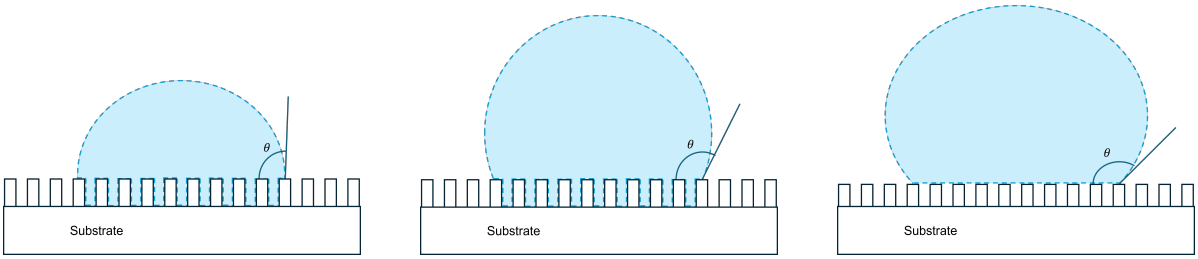

(a) Wenzel-state **(b)** Partial wetting **(c)** Cassie-state

Figure 2.2: Droplet morphology on non-smooth surfaces (adapted from El Fil et al. [2]).

Depending on the drop state, the thermal resistance may differ in determining the heat flux and HTC. Multiple scholars determined the resulting heat flux through a droplet for different states. These are all summarized by El Fil et al. [2] and should be applied accordingly.

2.3. Modelling of filmwise condensation

Nusselt theory describes the modelling of the HTC in FWC [18, 31]. Here, HTC modelling should account for the added thermal resistance resulting from the liquid film on the surface. On a vertical wall, the thickness of the liquid film varies depending on the condensation rate. The average HTC ($\bar{h}$, in [$\mathrm{W/(m^2\,K)}$]) can be determined by Equation (2.2), assuming the effects of fluid acceleration and heat convection are negligible (i.e., Nusselt-assumptions).

$$\bar{h} = 0.943 \left[\frac{h_{\mathrm{fg}} g \left(\rho_l - \rho_v\right) k_l^3}{L \left(T_{\mathrm{sat}} - T_w\right) \nu_l} \right]^{1/4} \tag{2.2}$$

Here, h_{fg} is the latent heat of vapourisation [$\mathrm{J/kg}$], g is the gravity constant [$\mathrm{m/s^2}$], ρ_l is the density [$\mathrm{kg/m^3}$] of the liquid, ρ_v is that of the vapour. The thermal conductivity of the condensate is denoted by k_l [$\mathrm{W/(m\,K)}$], L is the length-scale of the wall (height, [m]), T_{sat} is the saturation temperature [K], T_w is the wall surface temperature [K], and ν_l represents the kinematic viscosity of the fluid [$\mathrm{m^2/s}$].

Equation (2.2) applies for a vertical plate. When modelling vertical circular disks the length scale (L) should be changed to the effective length scale (L_e, in [m]). This is approximated by $L_e = 0.817D$, where D is the diameter of the disk [m] [28].

In liquids with relatively low enthalpy of phase change, a modified latent heat applies (h'_{fg}). This corrects for the subcooling term, given by:

$$h'_{\mathrm{fg}} = h_{\mathrm{fg}} + \frac{3}{8} c_{p,l} \left(T_{\mathrm{sat}} - T_w\right) \tag{2.3}$$

Here, $c_{p,l}$ is the specific heat capacity at constant pressure for the liquid condensate [$\mathrm{J/(kg\,K)}$].

Equation (2.2) is only applicable for non-turbulent regimes. If the film dynamics are turbulent ($Re > 30$), the film starts to show wavy behaviour, thus resulting in a varying film thickness. Then equations related to the Reynolds number are needed to determine the average HTC, as described by Incropera et al. [31].

2.4. Dropwise condensation modelling approaches

As DWC is a discrete phase transition process, modelling is different compared to the modelling of FWC. Here, drops grow at random sites on the surface, after which they will coalesce and depart from the surface. This makes it difficult to model in computational fluid mechanics, therefore scholars established a heat transfer model of a single droplet and used a statistical method to predict the overall surface HTC [20, 33].

According to the adsorption theory, heat transfer takes place on the free area of the condensation surface and on the surface of the drops. Both heat transfer routes need to be addressed accordingly, as both result in condensate (droplets) forming on the surface.

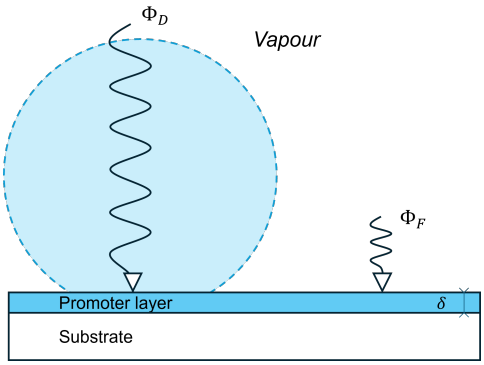

Figure 2.3: Schematic diagram of heat transfer routes to the exposed surface (Φ_F) and through a single droplet (Φ_D) on a smooth surface (adapted from Hu et al. [33], not scaled).

Figure 2.3 visualises these heat transfer routes. The total heat transfer taking place is the sum of the heat transfer to the free surface and to the droplets ($\Phi_{tot} = \Phi_F + \Phi_D$, in [W]). This allows for determining the average HTC of condensation to the substrate ($\bar{U}_{\mathrm{tot}}$ in [$\mathrm{W/(m^2\,K)}$]):

$$\bar{U}_{\mathrm{tot}} = \frac{\Phi_{\mathrm{tot}}}{A_{\mathrm{tot}} \Delta T} \tag{2.4}$$

Here, A_{tot} is the total condensation area (in [$\mathrm{m^2}$]) and ΔT the temperature difference between the vapour and the substrate (in [K]). The found average HTC also includes the promoter layer.

For the free surface (Φ_F), only the convective heat transfer and the conductance through the promoter surface has to be taken into account. For the promoter layer, the thermal conductivity and thickness are needed. For convection an average HTC for the vapour to the surface is needed, possibly determined by applying Nusselt Theory.

For the heat transfer route through the droplets (Φ_D), a method is described by Bortolin et al. [32] and Hu et al. [33]. This includes the heat transfer through a single drop on a smooth surface, taking into account the thermal resistance of conduction, interface and curvature of the drop. By a statistical method, this is then extrapolated over the whole surface to predict the overall HTC through droplets.

The single drop heat transfer (q_D) combines the interfacial thermal resistance (vapour-to-interface), the thermal resistance due to internal conduction and the thermal resistance of the promoter layer. All are dependent on the radius (r) of the droplet, and its contact angle with the surface (θ). Therefore the heat transfer changes while the drop grows in size due to condensation. In addition, the interfacial resistance includes a interfacial HTC, dependent on concentration of NCGs in the vapour and thermodynamic properties, such as: specific ideal gas constant, vapour specific volume, enthalpy of vapourisation, surface tension and saturation temperature [38].

The growth of a droplet starts from a thermodynamically defined minimum size (r_{min}) [39, 26]. Once a certain (effective) size is reached (r_e), estimated from the nucleation site density, the droplet starts to coalesce with droplets within reach [40]. This allows the growth to accelerate, next reaching the critical size at which the droplet starts to depart (r_{max})[22].

Not every condensate drop on the surface is the same size and is not always in the same locations, While the system differs on small time scales, over a large period of time it is statistically in steady state, laying the basis for the drop size distribution model. Le Fevre and Rose [41] applied this first. As the growth differs over the radius until departure, two distinct size distributions are needed: A droplet size distribution for drops larger than the effective radius ($N(r)$ for $r_e \leq r \leq r_{\max}$) and one for droplets smaller than the effective radius ($n(r)$ for $r \leq r_e$). Please refer to literature by Bortolin et al. [32] and Hu et al. [33] for determining the size distributions. The total heat transfer over the droplets (Φ_D) is related to the droplet size distribution by integrating over the radius, from the minimum radius to the maximum radius with according size distribution. This is then multiplied by the droplet covered surface area (A_D in [m^2]):

$$\Phi_D = A_D \left(\int_{r_{\min}}^{r_e} q_D(r) n(r) dr + \int_{r_e}^{r_{\max}} q_D(r) N(r) dr \right) \tag{2.5}$$

This model assumes a uniform heat transfer over the whole surface of the drop. However, as Chavan et al. [38] argues, most heat transfer at the three-phase contact line. Reaching increased heat fluxes up to four orders of magnitude compared to elsewhere. To include this into the model, empirical relations are used to find the heat transfer through a single drop. These include the Biot number (based on the interfacial heat transfer coefficient, base radius and thermal conductivity) and the Nusselt number (based on the Biot number and the contact angle), defined at different Biot numbers. Then the heat transfer through a single droplet is determined and applied to the the statistical approach shown above.

2.5. Surface properties

To limit the wetting of condensate on the surface, especially with low surface tension fluids, surface modifications can be applied to promote DWC. The difference in surface and liquid free energy ($\Delta\gamma$) gives the mode of condensation. This difference is calculated as:

$$\Delta\gamma = \gamma_l - \gamma_s \tag{2.6}$$

Here, γ_l and γ_s are the free surface energy of the liquid condensate and the surface, respectively, in [$\mathrm{mJ/m^2}$]. FWC is formed if $\Delta\gamma \leq 0\mathrm{mJ/m^2}$, DWC and FWC can coexist when $0 < \Delta\gamma \leq 33.3\mathrm{mJ/m^2}$. If $\Delta\gamma > 33.3\mathrm{mJ/m^2}$, DWC is formed [33].

To lower the surface free energy, literature proposes two options. The first consists of modifications to the surface chemistry of a given substrate by applying a thin coating over the condensation surface. The second approach is modifying the surface morphology [32].

2.5.1. Coating

Metals, such as aluminium, copper and steel, are frequently used in heat transfer applications. However, condensation on these surfaces are in FWC mode due to the high surface free energy of the metals. To obtain DWC, a coating can be applied to reduce the surface free energy, while maintaining the favourable properties of these metals, e.g., thermal conductivity. Several options are available: Polymeric coatings, self-assembling monolayers, ion implantation and electroplating of noble metals [32, 42].

- Polymeric coatings: Materials such as parylene, silicones and polytetrafluoroethylene (PTFE, e.g., teflon), are effective coatings to enhance DWC. Improving the HTC 1.6-28.6 times compared to FWC [30]. However, durability of these coatings comes at the cost of the thickness, possibly raising the thermal resistance and eliminating DWC's advantages over FWC [28, 43].
- Self-assembling monolayers: Here molecules with a functional side (hydrophobic) and reactive side (adhesion) align on the surface. The reactive side adheres to the substrate, while the functional is directed towards the vapour, creating a coating thickness of a single molecule. These show significant durability and HTC enhancement in DWC [30].
- Ion implantation: Here the surface of the substrate is hit with high energy ions. Thereby altering the structure of the surface in a very thin layer, thus changing its properties [44]. This can make a

material significantly more hydrophobic. This method creates a very durable surface, sustaining DWC for a very long time [30]. Moreover, this method can increase the nucleation site density as well [2].

- Noble-metal electroplating: Even though noble metals are high in surface free energy, they are great at promoting DWC in water. This is explained by the weak bondings between water and the surface due to the lack of surface oxides. Noble metals do not corrode, and thus form no oxide layer on the surface. These layers can be formed by electroplating, and prove to be very durable coatings. For low surface tension fluids, like refrigerants, the difference in free surface energy would not be sufficient to support dropwise condensation [28, 30, 45].

2.5.2. Surface micro and nano structures

Nature uses nanostructures to create natural hydrophobic surfaces, for example, this is found on lotus leafs and cicada wings [33, 46]. By creating a Cassie or partial wetting state (Figure 2.2) with the help nanostructures to turn naturally hydrophilic surfaces to hydrophobic.

Nanostructures on the surface exist in different shapes, such as nano-wires, -cones, -rods, -sheets and -blocks. These can be applied by different methods, like (laser) etching, oxidation, spray, electro-deposition, etcetera [33, 47, 48]. Nam and Ju [49] achieved control over the wettability by oxidising a copper substrate, reporting contact angles from 10° to 170°. Luo et al. [50] reported improvement of the contact angle to 130° by precisely laser etching a copper surface to obtain a Cassie-state. Both researches refer to the contact angle of water.

To achieve a hydrophobic properties on a copper substrate, graphene coating on etched surfaces can promote DWC of steam [51]. However, the graphene coating has to be treated to reduce the oxygen groups in the graphene, for example with an chemical or thermal reduction process [32]. Graphene has additional favourable properties such as high thermal conductivity, anti-corrosion and the ability be applied in a thin layer [46]. However, the application to a copper surface is a comprehensive process with many steps (chemical vapour deposition). But it is able to improve the transfer of up to 4 times compared to bare copper [52].

2.6. Heat transfer enhancement factors

As mentioned previously, the departure of drops restarts the droplet nucleation and growth process. Here most of the heat transfer takes place. To enhance heat transfer, an increased departure rate is needed. Parameters such as surface inclination and vapour velocity assist the departure of droplets of the surface by decreasing the maximum droplet radius ($r_{\max}$) [32, 53, 54].

Other factors can influence the HTC negatively. Such as the presence of NCG. These can form an additional thermal resistance barrier on the condensible surface [55]. As mentioned, the amount of NCGs present influences the interfacial HTC negatively, thus decreasing the heat flux through a drop. Moreover, when nanostructures are present on the surface, NCG can accumulate within these structures, raising the thermal resistance. However, research showed that in most cases, DWC with NCG present is still more efficient than FWC in the same conditions [2, 55].

The degree of subcooling also influences the formation and promotion of DWC. This is the temperature difference (ΔT) between the vapour at saturation temperature and the surface on which it condensates (also referred to as cooling intensity). At low subcooling, DWC has a much higher heat flux compared to FWC. However, if the subcooling increases, the increased heat flux can cause the surface to flood and the performance to drop to FWC [2]. DWC stays more stable at lower degrees of subcooling [20].

2.7. Advancements in dropwise condensation of refrigerants

As mentioned previously, most research conducted in DWC is focussed on water [2]. However, DWC for refrigerants has great potential in increasing safety in refrigeration and HVAC systems. This section focusses on surface modifications possible for low surface tensions fluids, and experiments conducted in literature in this field.

2.7.1. Surface modification for low surface tension fluids

Water has an advantageous high surface tension ($58.8\mathrm{mN/m}$ at $100°$ [56]), therefore a surface that repels it is relatively easy to fabricate. However, the surface tension of low ODP and GWP refrigerant is much lower. For example, the surface tension of R1233zd(E)[1] is only $14.3\mathrm{mN/m}$ at $27°$, and lowering as temperature increases [57]. (Super)Hydrophobic surfaces perform poorly with low surface tension fluids, to resolve this, (super)omniphobic surfaces are needed. With a super low surface free energy, repelling even low surface tension fluids off the surface [58].

Whereas hydrophobic surfaces can be created by utilising a low surface energy coating or applying nanostructures to the surface. Omniphobic surfaces require both to improve surface anti-wetting properties for polar and non-polar fluids [58]. For example, only applying nanostructures to a copper substrate did not improve the HTC compared to bare copper surface [59].

When a nanostructure has been applied to a surface, a low surface tension fluid can flood the porous structure. This will decrease the departure rate of drops or even wet the surface [60]. To promote DWC on nanostructured surfaces, the surface can be infused by a low surface tension lubricant. Such lubricant infused surfaces (LIS) become smooth but are able to repel low surface tension fluids [61, 62].

2.7.2. Experiments in DWC with low surface tension fluids

Recent experimental research into DWC with low surface tension fluids have been summarized in the table below. Various surface treatments - including omniphobic promoter layer - were applied to possibly enhance the HTC of condensation.

Table 2.1: Experimental research in HTC enhancement using DWC in low surface tension fluids.

Fluid(s)	Substrate	Surface treatment	HTC enhancement (compared to bare surface)	Study
R1233zd(E)	Copper & Aluminium	Edged surface (nanostructures)	No HTC improvement for copper, slight improvement for aluminium	[59]
Ethanol, Hexane, Pentane & R1233zd(E)	Copper, Aluminium	Parylene-C layer, Silane top layer, with adhesion enhancement layers[2]	Significant HTC improvement, 260% for ethanol up to 688% for R1233zd(E)	[62]
Ethanol	Copper with silicone layer	PFPE[3] & FQLS[4] coating, including microchannels	HTC improvement by 100-500%	[63]
Ethanol, hexane & pentane	Substrate independent	Polymer coating	HTC improvement by 400-800%	[64]
Among others: pentane, hexane, ethanol & toluene	Aluminium	Fluorosilane coating and LIS (Krytox oil)	HTC improvement of ~500% with clean fluorosilane, with LIS sporadic improvement (max ~500%)	[60]

[1] No ODP and GWP of 1
[2] This coating layer up can be applied to most metallic surfaces
[3] Short for Perfluoropolyether
[4] Short for Fluorinated quasi-liquid surface

Fluid(s)	Substrate	Surface treatment	HTC enhancement (compared to bare surface)	Study
Ethanol & Hexane	Copper	LIS with 3 types of oil (2xKrytox & Fomblin), nanostructures created by copper oxidation	HTC improvement by 50-150%	[61]

3

Setup design

This chapter discusses the design of the experimental setup to determine the HTC in DWC in a refrigerant. First, the formal objectives are set in Section 3.1. Next, the requirements are shown in Section 3.2. After, Section 3.3 shows the chosen refrigerants. Then, Section 3.4 discusses the design possibilities along with the chosen approach and completed design. Then, the process to facilitate the condensation process is shown in Section 3.5. Next, the expected setup dynamics are discussed in Section 3.6. Lastly, Section 3.8 shows photos of the manufactured parts to be mounted in the setup.

3.1. Objectives

As posed before, current research lacks the achievement of DWC in low surface tension fluids and literature shows little results in terms of the associated quantification of the heat transfer coefficient. Therefore the objectives of the setup are the following:

1. Achieve DWC in a low surface tension fluid, preferably a fluid relevant for low-GWP regulation and HVAC systems.
2. Determine the heat transfer coefficient of the condensation process occurring, and visually validate the form of condensation.
3. Determine the heat transfer coefficient of condensation on different surface coatings.

3.2. Design requirements

To achieve the objectives of the setup, requirements are set to comply the setup to. Later, this is used to verify the function of the completed setup design. The design requirements are be found below.

Table 3.1: List of setup design requirements.

Requirement	Context
Different surfaces	It should be possible to test a variety of different surfaces to see which achieves the highest heat transfer coefficient.
Visual on condensation process	To validate that DWC is occurring, a visual of the condensation surface should be possible.
Results uncertainty	The HTC is determined from measured parameters. The measurements should allow for a feasible uncertainty.
Different fluids	The setup should first be validated with a low surface tension refrigerant at lower pressures. Then, the setup should be able to handle other fluids, such as natural refrigerants.

Requirement	Context
Uniform temperature	The condensation surface should have a (close to) homogeneous temperature profile, this way an accurate estimation of the HTC can be made.
Maximum vapour temperature	To prevent degradation of coatings, the maximum temperature of the vapour is $60\,^{\circ}\mathrm{C}$.
Degree of subcooling	The HTC can differ if the subcooling varies. To test for this, the degree of subcooling should be a controlled parameter.
Symmetric condensation surface	As the condensate flows down, is should not be funnelled into one spot before leaving the condensation surface. This change the condensation mode locally to FWC. To prevent this, a symmetric condensation surface is needed.
Mass flow control	The vapour velocity can be of influence to the HTC, to minimize its effects, the mass flow rate of the vapour should be controlled.
Regulate saturation pressure & temperature	The saturation pressure (and thus temperature) should be controlled to determine the HTC at different pressures.
NCG presence	The presence of NCGs influences the HTC negatively, therefore these should be taken out of the setup as much as possible.
Safety	To ensure the well-being of the experimentalist/operator and associates in the lab-area, a external party of the project should consider it safe.
Small form-factor	To allow for ease of handling and minimization of heat losses, the setup should be of a small form-factor.
Manufacturability	It is preferred to keep the outsourcing of manufacturing and machining of parts ot a minimum.
Costs	Costs of fabrication and maintenance should be minimized.

3.3. Refrigerant choice

As mentioned in the requirements, at first a harmless conventional refrigerant should be used to validate the function of the setup. Afterwards, natural refrigerants should be used to find the HTC of condensation of different surface coatings. However, caution is required as most natural refrigerant are high in damage potential, such as flammability, toxicity, and high pressure.

The harmless refrigerant R245fa is suitable. Its saturation temperature to pressure allows for a low pressure system, as the $60\,^{\circ}\mathrm{C}$ limitation results in maximum $4\,\mathrm{bar}$ of absolute pressure. Moreover, its surface tension is very low, allowing for purposely experimenting with suitable coatings.

In the future, R717 (Ammonia, NH_3) would be interesting as a working fluid. Due to it being a natural refrigerant, it could be used in household/industrial applications. Therefore, R717 is also partly considered during the setup design. However, when applying this fluid, extra caution is needed due to its flammability and toxicity. Other natural refrigerants could also be used in the future.

In the table below additional properties of R245fa and R717 can be found together with a comparison to water. Figure 3.1 & Figure 3.2 show the saturation curve and Mollier diagram respectively, please refer to Chapter A for the background of these figures.

Table 3.2: Thermophysical properties of refrigerants compared to water ($P_{atm} = 1.013\mathrm{bar}$) [65].

Property	Water	R245fa	R717
Chemical formula	H_2O	$CHF_2CH_2CF_3$	NH_3

Property	Water	R245fa	R717
Boiling temperature at P_{atm} [°C]	100.1	15.2	−33.2
Critical temperature [°C]	374.1	154.0	132.6
Critical pressure [bar]	220.6	36.5	113.6
Enthalpy of vapourization [kJ/kg]	2256.5	196.8	1369.7
Viscosity at 25 °C [mPa s]	0.89	0.44	0.13
Surface tension at 25 °C [mN/m]	72.1	13.7	20.5
GWP100 [kg CO_2-eq/kg] [66]	N/A	962	0

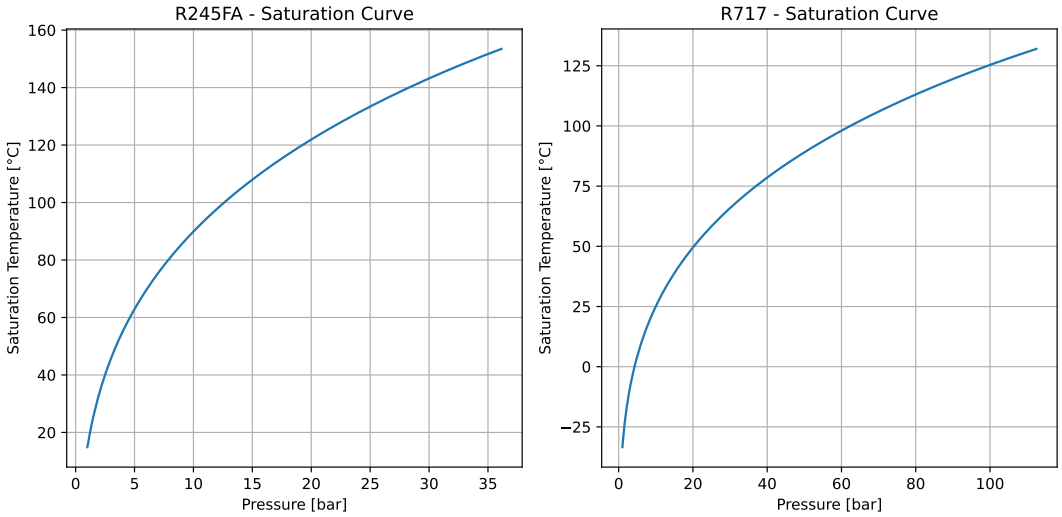

Figure 3.1: Saturation curve of R245fa and R717 [65].

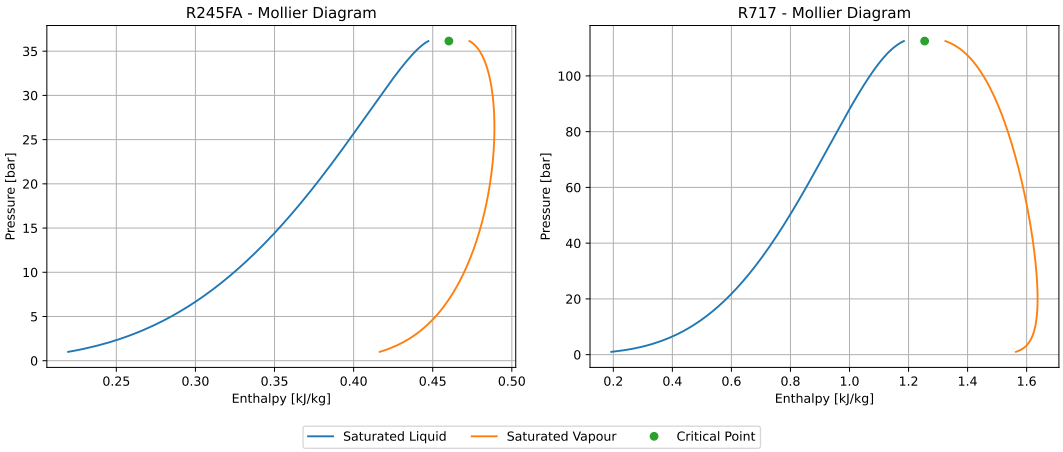

Figure 3.2: Mollier diagram of R245fa and R717 [65].

To comply with the maximum vapour temperature with regards to coating degradation, for R245fa 4 bar is the limit, for R717 it is $20 - 25$ bar. With view of component pressure ratings, it the system pressure

rating is set at $20\ \mathrm{bar}$.

3.4. Test-section design

The test-section is where the condensation process takes place. This section will explain the design choices of the test-section and show how the HTC should be determined. As condensation releases heat to the surface on which condensation takes place, the substrate should be cooled to prevent it from increasing in temperature. Therefore, a coolant loop is required.

3.4.1. Determining the heat transfer coefficient of condensation

Determining the heat transfer coefficient of the condensation process is the objective of the setup. This can be determined from the basic equation for heat transfer, as shown below.

$$\dot{Q} = UA\Delta T \tag{3.1}$$

Here $\dot{Q}$ (in [W]) is the heat transfer taking place, U (in $[\mathrm{W/(m^2\,K)}]$) is the overall HTC, A (in $[\mathrm{m^2}]$) is the area and ΔT (in [K]) is the temperature difference.

In Equation (3.1), the overall heat transfer coefficient (U) combines all the thermal resistances the heat transfer goes through, therefore the HTC of condensation is also part of this value. If the total heat transfer ($\dot{Q}$) can be determined, the overall HTC can be backtracked . When all the thermal resistances are known, the HTC of condensation results. To determine the heat transfer ($\dot{Q}$), the three options below are available:

Option 1: The energy increase of the coolant can be measured in terms of temperature increase. As shown below:

$$\dot{Q} = \dot{m}c_p\Delta T \tag{3.2}$$

Here $\dot{m}$ (in $[\mathrm{kg/s}]$) is the mass flow rate, c_p (in $[\mathrm{J/(kg\,K)}]$) is the specific heat of the fluid, and ΔT (in [K]) is the temperature difference. As the energy increase is directly related to the heat flow, the HTC can be determined. This method effectively allows for the use of a simple plate or tube heat exchanger design, where the temperature of the coolant is measured at inlet and outlet.

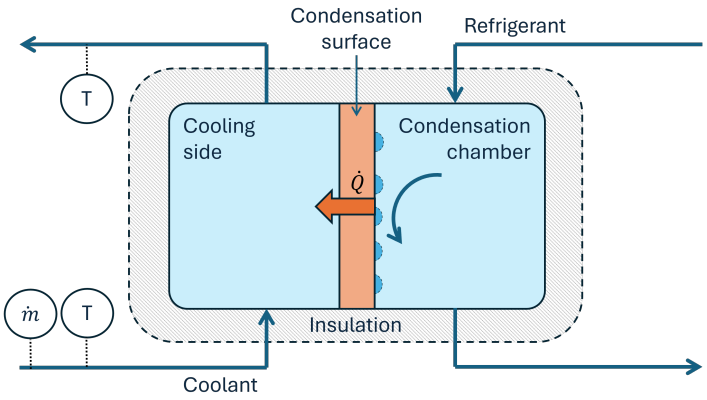

Figure 3.3: Conceptual solution to measure the heat transfer by measuring the change in internal energy of the coolant; the coolant loop is on the left, here the temperatures are measured at the inlet and outlet. Also the mass flow is measured here, in this case at the inlet. On the right is the condensation chamber, saturated vapour enters from the top, condensation takes place on the condensation surface and it and left over vapour are removed from the bottom.

A design like this is shown in Figure 3.3. The mass flow of the coolant must allow for a measurable temperature difference. This results in a temperature profile between the inlet and outlet of the coolant. Therefore applying the correct ΔT in Equation (3.1) can prove to be an issue. As there is no homogeneous coolant temperature.

This method also requires an accurate flow sensor to measure $\dot{m}$, which can be unreliable for small flow rates. It also gives difficulty in changing the condensation surface, as coolant and refrigerant and separated by one plate and mixing of the two should be prevented.

Option 2: The heat transfer due to condensation can be measured in terms of latent heat of vapourisation of the fluid and the amount condensate forming:

$$\dot{Q} = \dot{m} h_{fg} \tag{3.3}$$

Here, $\dot{m}$ (in $[\mathrm{kg/s}]$) is the amount of liquid condensate forming, h_{fg} (in $[\mathrm{J/kg}]$) is the latent heat of vapourisation.

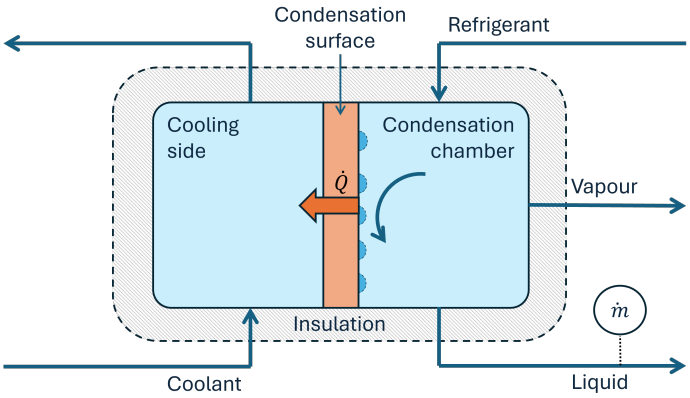

Figure 3.4: Conceptual solution to measure the heat transfer by measuring the formation rate of liquid condensate; the coolant loop is on the left. Saturated vapour enters the condensation chamber (right) at the top. Condensate formed on the condensation surface flows down into the liquid outlet at the bottom. Here, the mass flow of liquid condensate forming is measured. The surplus of saturated vapour is removed via an other way, in this case on the side.

Figure 3.4 shows a design in which the liquid condensate forming over time is measured. In principle, condensation takes on the condensation surface, however, it can also occur on the walls of the whole chamber. Therefore there is a large uncertainty about the amount of condensation taking place on the tested surface. Moreover, if the surface is small, the amount of condensation is also small, therefore harder to measure certainly.

Option 3: According to Fourier's law of conduction the heat transfer can also be calculated as:

$$\dot{Q} = \frac{kA\Delta T}{L} \tag{3.4}$$

Here, k (in $[\mathrm{W/(m\,K)}]$) is the thermal conduction coefficient of the material, A (in $[\mathrm{m^2}]$) is the cross-sectional area of the direction of the heat flow, ΔT (in $[\mathrm{K}]$) is the measured temperature difference, and L (in $[\mathrm{m}]$) is the distance over which the temperature difference is measured.

When using Fourier's law, the area and the distance between temperature measurements can be chosen in the design-phase. If a material with a high coefficient of conduction is chosen, the radial temperature distribution is close to homogeneous, especially when applying insulation.

Figure 3.5 shows a design based on Fouriers law of conduction. As mentioned, this design allows for a homogeneous temperature of the condensation surface, and also for different surfaces. To limit the costs and form-factor, the condensation surface is decreased compared to the other options.

Preferred design approach: Due to the nature of option 1, it does not comply to the homogeneous condensation surface requirement. Moreover, integrating a swappable surface can prove to be difficult.

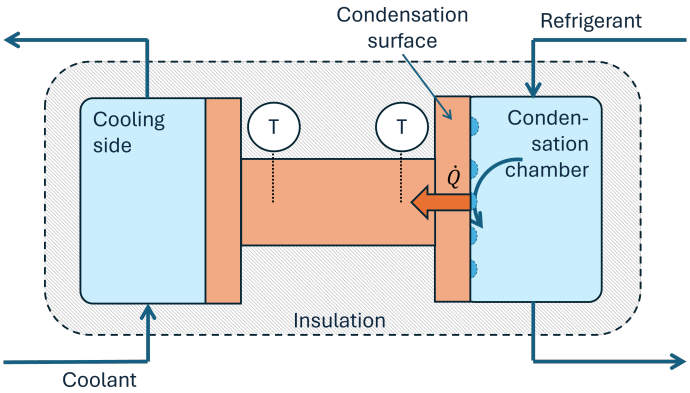

Figure 3.5: Conceptual solution to measure the heat transfer by Fourier's law of conduction; the coolant loop is again on the left. Condensation takes place on the right, where saturated vapour flows in from the top. The liquid condensate forming on the condensation surface and the saturated vapour surplus are removed from the bottom. Heat flows from the condensation surface to the coolant through a rod. Here, a temperature difference occurs and is measured between measurement points.

Also, accurate measurements of the flow can be hard, as accurate flow meters for small flows are expensive.

Option 2 allows for a simple design, but measuring the amount of condensation certainly is challenging as condensate can also form on other surfaces than the test surface. Therefore heat transfer into the test-surface will be overestimated.

Option 3 allows for the most design variability to measure a temperature difference accurately and reliably. From Equation (3.4), the cross sectional area A and distance between measurements L can be chosen. However, the thermal conductivity coefficient should be measured/calibrated beforehand. This makes option 3 the most promising design option, and will therefore be explored in the next phase.

While determining the geometry of the test-section, the following should be taking in to account beforehand:

- Materials: To achieve effective heat transfer from the condensation side to the cold side, high thermal conductivity materials are preferred. This decreases thermal resistance and prevents heat congestion in the chosen geometry. Copper can be machined and is chemically compatible with R245fa. For R717 aluminium can be used.
- Calibration: The coefficient of thermal conductivity can differ between sources. Therefore a method of calibrating the material should be considered[1].
- Circular measurement section: While measuring the heat transfer by conduction, an axisymmetric cross-section is preferred. This makes the temperature inside the geometry also axisymmetric. Therefore, the orientation of the temperature holes are not important.
- Temperature measurement swappable surface: The connection between the measurement section and the swappable surface has a (unknown) thermal resistance. Therefore, a temperature difference in the swappable surface is needed to backtrack the condensation surface temperature.
- Thermal paste: The swappable surface and the measurement section should be connected with as little thermal resistance as possible. Therefore thermal paste is needed and it should be squeezed effectively.

3.4.2. Heat transfer and geometry calculations

To design a geometry of the test section in which Fourier's law of conduction is used, first the expected heat transfer should be determined, then the appropriate geometric distances/parameters are chosen.

[1] Using Fourier's law of conduction, the thermal conductivity can be calibrated by setting the heat transfer rate ($\dot{Q}$). For this a heating pad can be used, the smallest available size is $50\,\mathrm{mm} \times 50\,\mathrm{mm}$. This limits the size of the condensation surface.

Modelling HTC in FWC: The objective is to achieve DWC, when this is not achieved FWC will occur. This should still be measurable by the setup. Therefore FWC mode acts as a baseline for the geometry choices.

To determine the HTC in FWC, Nusselt theory is applied as discussed in Section 2.3 [18, 31]. Specifically looking at different surface subcooling temperatures and saturation pressures. How this method is applied is shown in detail in Chapter A.

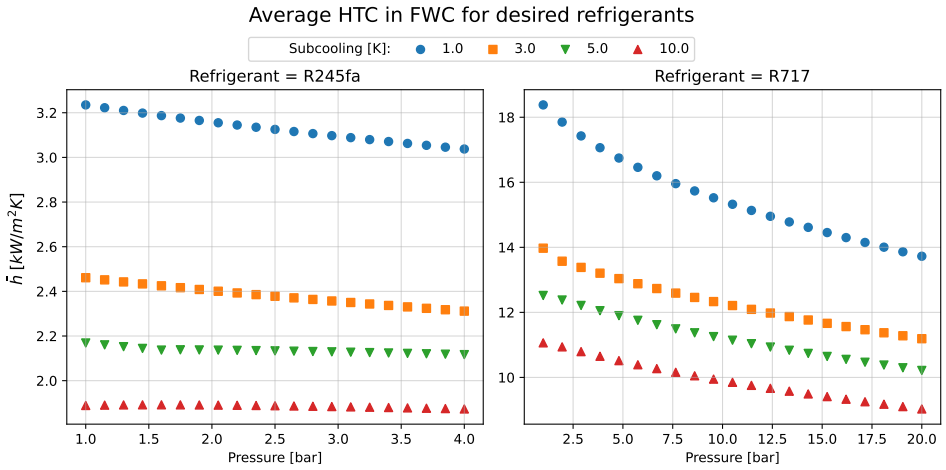

Figure 3.6: Modelled average HTC in FWC of R245fa & R717 at different saturation pressures

The fluid properties in Equation (2.2) differentiate with pressure (P, in [bar]), therefore the expected average HTC differs with pressure. Moreover, the degree of subcooling also influences the HTC but is a design choice. Therefore the expected average HTC in FWC is modelled for different subcooling temperatures.

Figure 3.6 shows that the expected HTC in R245fa is much lower than the expected HTC of R717. Therefore, the geometry must be designed for the lowest expected HTC. The subcooling of the surface should be small to decrease the effect, but sufficient to allow for effective condensation. Therefore, the test section should be designed for roughly $3\,\mathrm{K}$–$5\,\mathrm{K}$ of subcooling. This means that the minimum expected HTC of FWC is approximately $2.2\,\mathrm{kW/(m^2\,K)}$.

Appropriate cross-section and distance: To determine the heat transfer using Fourier's law of conduction Equation (3.4), an appropriate cross-section and distance between the temperature measurements must be chosen. The exact method is shown in Chapter A. First the total heat transfer is determined for different HTC's, here the HTC of FWC serves as a baseline. Then the expected measured temperature difference is determined for different distances and cross-section diameters. Its result is shown in Figure A.8. To allow for a temperature measurement device, the minimum diameter is set at $25\,\mathrm{mm}$, its maximum is the same as the width of the condensation surface ($50\,\mathrm{mm}$).

To measure the temperature difference effectively, the desired minimum temperature difference has been set to roughly $5\,\mathrm{K}$. That means that a diameter of $35\,\mathrm{mm}$ and distance of $60\,\mathrm{mm}$ should be sufficient for the minimum expected HTC. This also allows for enhanced manufacturability, as space is not as tight and the diameter allows for structural integrity.

3.4.3. Resulting test section design

While taking the above in consideration, the following design resulted. The test-section contains two main components: the swappable surface, including the condensation surface at which the surface modification can be applied. And, the measurement section in which the heat transfer is measured. The geometry is shown in Figure 3.7, its dimensions are shown in Chapter A. The features of the swappable condensation surface and the measurement section are shown in Table 3.3.

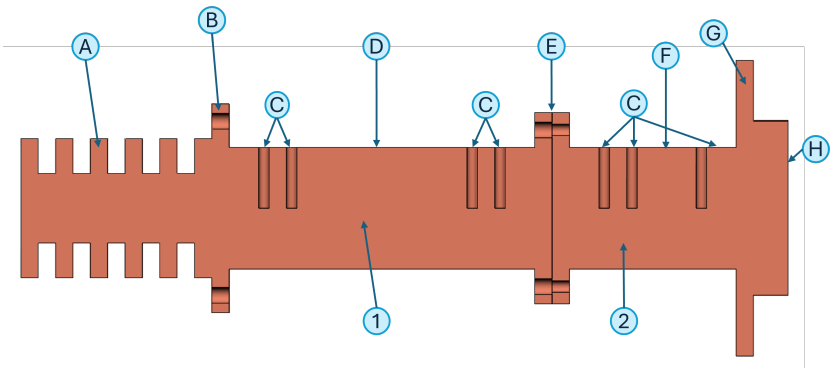

Figure 3.7: Lengthwise cross-section of the swappable condensation surface and measurement section with its features (Table 3.3).

Table 3.3: Features of the swappable condensation surface and measurement section.

Feature	Description
A	Fins for increased surface area to enhance cooling.
B	Bolt flange to attach the measurement section to the cooling chamber.
C	Holes to the rods center for temperature sensors. The the swappable condensation surface (2) to backtrack the condensation surface temperature. In measurement section (1) to measure the temperature difference and determine the heat transfer according to Fourier's law of conduction Equation (3.4).
D	Reduced diameter ($35\,\mathrm{mm}$) rod where the heat transfer is determined by temperature measurements.
E	Bolt flange to attach the swappable condensation surface to the measurement section.
F	Reduced diameter ($35\,\mathrm{mm}$) rod where the temperature is measured.
G	Flange for attachment to the condensation chamber.
H	Square condensation surface ($50\,\mathrm{mm} \times 50\,\mathrm{mm}$)

To facilitate the swappable surface and the measurement section, two chambers are needed. First the condensation chamber, the construction should withstand the refrigerant(s) at pressure. On the other side a cooling chamber is needed. Figure 3.8 shows the components of the condensation chamber and the cooling chamber. The components of the whole test-section are described in Table 3.4.

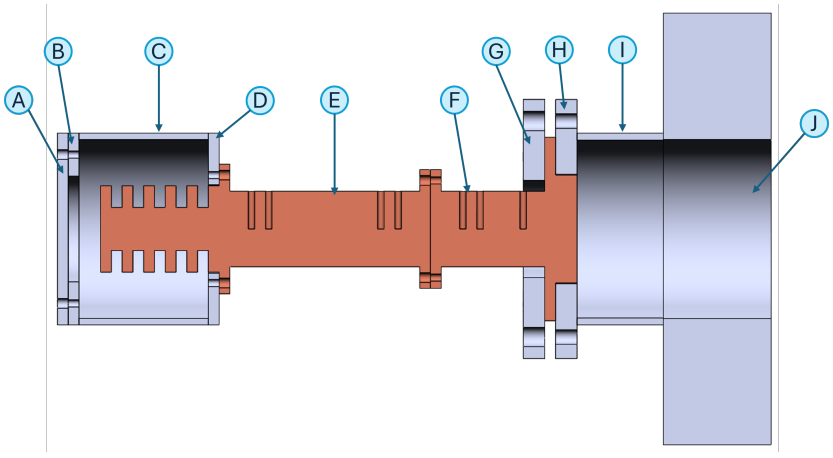

Figure 3.8: Lengthwise cross-section of the test-section with all its components (Table 3.4).

Table 3.4: Components of the test section.

Component	Description
A	Cooling chamber closing plate.
B	Bolt hole closing flange.
C	Cooling chamber tube.
D	Bolt hole flange to attach measurement section to.
E	Measurement section for determining the heat transfer.
F	Swappable condensation surface.
G	Bolt on squeeze flange, split in two parts to fit over the swappable surface to measurement attachment flange.
H	Weld on bolt hole flange to attach squeeze flange to.
I	Condensation chamber tube.
J	View glass with weld flange.

3.5. Process design

To facilitate the test-section with saturated vapour for in the condensation chamber and coolant in the cooling chamber, an auxiliary loop needs to be designed. First a conceptual design is discussed, then the full design and overall Piping & Instrumentation diagram (P&ID) are shown.

3.5.1. Conceptual setup design

In principle, on one side of the test section sufficient cooling must be available. The coolant loop is relatively simple, a source of coolant with temperature control is needed. This allows for setting the degree of subcooling of the condensation surface depending on pressure and/or fluid.

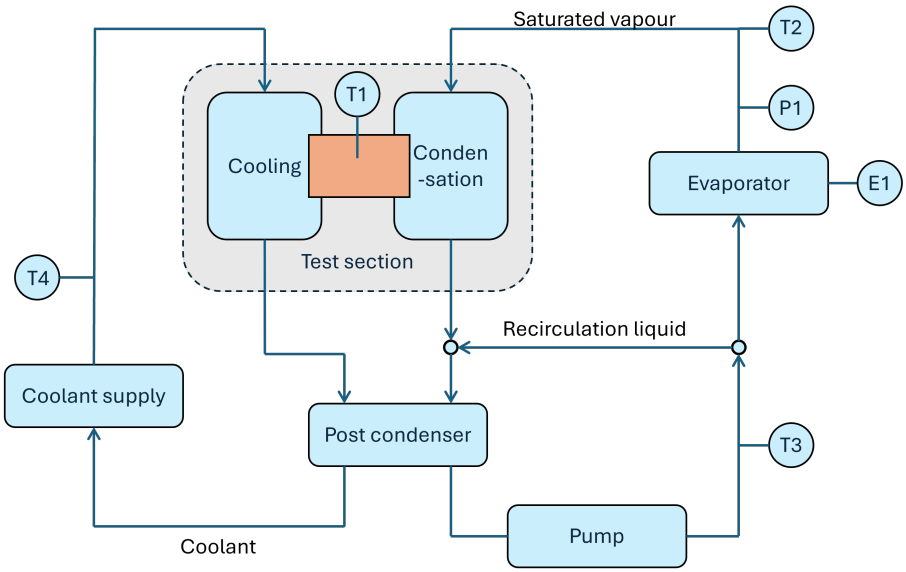

Figure 3.9: Conceptual flow diagram of components auxiliary to the test-section; A coolant loop supplies cooling to the test section and the post-condenser (left), also its temperature is measured. The pressurised side (right) facilitates saturated vapour. The post-condenser handles the surplus of vapour, a pump circulates the liquid, an evaporator supplies saturated vapour. The test-section connects the pressurised side to the cooling side (instrumentation in Table 3.5).

Figure 3.9 shows the conceptual process diagram of the setup. On the condensation chamber side, an oversupply of saturated vapour should be available. This means an evaporation process is needed that supplies saturated vapour. Not all vapour condensates, therefore a post-condenser is needed to make

sure all vapour condenses back to liquid. It can then be supplied back to the evaporation process by a pump. In addition, the amount of saturated vapour needed can be different per fluid or pressure. To control the subsequent vapour velocity, the supply to the evaporator should be controlled. Therefore, a flow controlled circulation loop is required. The instrumentation for measurements are explained in Table 3.5.

Table 3.5: Instrumentation of the conceptual P&ID (Figure 3.9)

Sensor	Description
T1	Temperature sensors in the swappable condensation surface and measurement section.
T2	Temperature sensor in the saturated vapour. This serves as a control to the pressure sensor (P1).
T3	Temperature sensor in liquid refrigerant.
T4	Temperature sensor in fresh coolant supply. This allows for heat transfer calculations in the cooling chamber.
P1	Pressure sensor to determine the saturation properties of the fluid and to control the energy input.
E1	Energy input measurement, this way the rate of evaporation can be determined[2].

3.5.2. Full setup process and instrumentation diagram and considerations.

After the conceptual auxiliary design loop, a full process and instrumentation diagram (P&ID) is designed and shown in Figure 3.10.

As shown, the evaporator is integrated in a liquid reservoir. This allows the supply of saturated vapour to the condensation chamber. The evaporator creates a hot spot and (superheated) vapour bubbles, these heat the liquid in the reservoir. Essentially creating a buffer zone to ensure the supply of saturated vapour.

When swapping the condensation surface, the condensation chamber can be isolated by *HV01* & *HV02*. By coupling a vacuum pump to *VF01* or *VF02* the NCG's can be reduced. This is also needed after swapping the surface. The operator knows the pressure of the system with the help of *PI01* & *PI02*. The thermal bath (*TB*) allows for temperature control of the coolant. And *NV* and *CV* give control over the amount of flow and its direction.

3.6. Setup dynamics

This section elaborates the simulation of the heat flow within the setup. Therefore it explains how the setup would behave when attempting to find the HTC in R245fa.

First the heat transfer due to condensation at different HTC is modelled. This will determine a number of specifications, such as the amount of vapour required, the evaporator power needed, the size of the PCD, and the desired temperature coolant.

The the coolant temperature is limited to $5\,^{\circ}\mathrm{C}$, if this limit is reached the desired coolant temperature is set to this limit[3]. Then the new total heat transfer is determined with the addition of the HTC in question, this allows for backtracking the condensation surface temperature.

For R245fa, the pressure is set from $1\,\mathrm{bar}$–$4\,\mathrm{bar}$. The desired subcooling of the condensation surface is set to $3\,\mathrm{K}$. For R717, the pressure is set from $7\,\mathrm{bar}$–$20\,\mathrm{bar}$, with the same desired subcooling. The simulation is run several HTC's: $2.2\,\mathrm{kW/(m^2\,K)}$, $5\,\mathrm{kW/(m^2\,K)}$, $10\,\mathrm{kW/(m^2\,K)}$, $15\,\mathrm{kW/(m^2\,K)}$ and

[2] By measuring the temperature before and after the evaporator, the specific enthalpy is known. This allows to determine the mass flow rate according to: $\dot{Q} = \dot{m}\,(h(T_4) - h(T_3))$

[3] If the coolant is pure water, it is limited to the freezing temperature ($0\,^{\circ}\mathrm{C}$) including some margin.

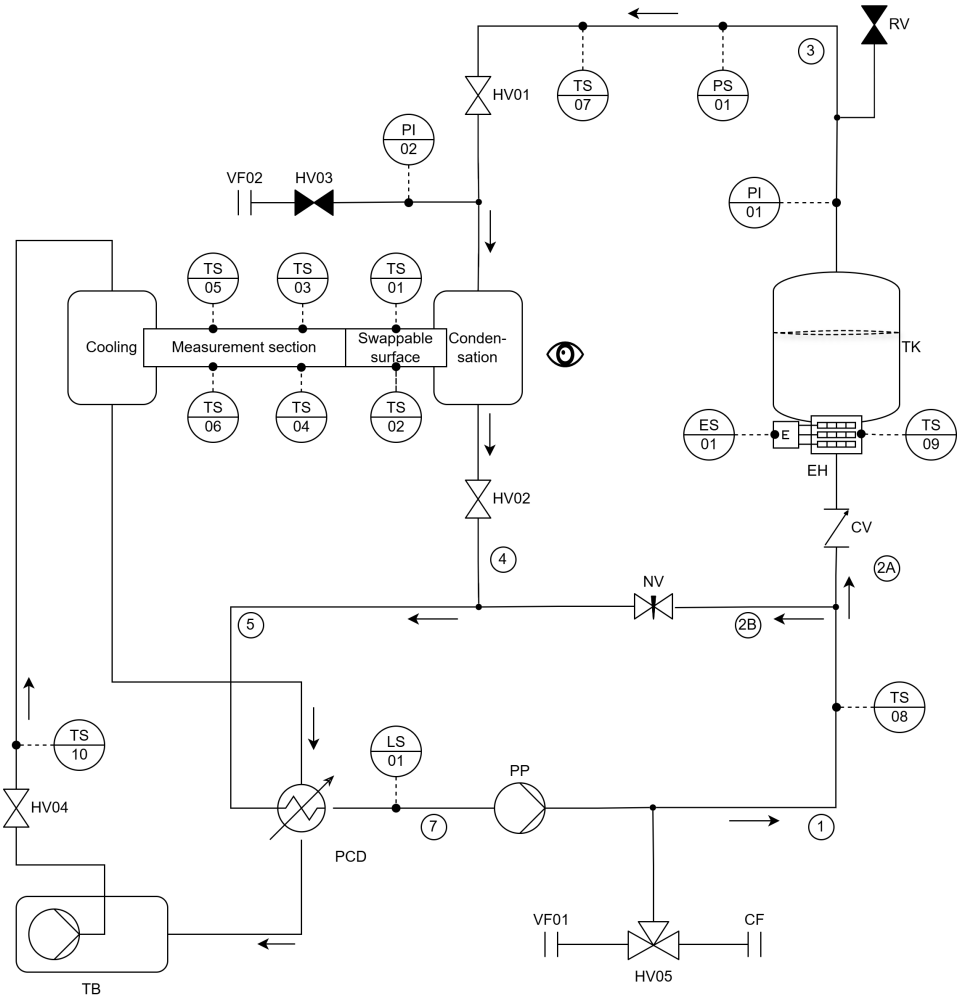

Figure 3.10: Process and instrumentation diagram for auxiliary setup loop. HV: hand-valve; NV: needle-valve; CV: check-valve; RV: relief-valve, refer to Chapter A for a description of (other) components.

$25\,\mathrm{kW/(m^2\,K)}$. As the true HTC is to be estimated in the setup, the chosen values are a range of possible HTCs. These determines an hypothetical heat input due to condensation. If the cooling surface temperature is set to the coolant temperature (in $[^\circ\mathrm{C}]$) by assuming sufficient cooling capacity, the coolant temperature (in $[^\circ\mathrm{C}]$) can be determined with the total thermal resistance of the rod ($\sum R_{rod}$, in $[\mathrm{K/W}]$) by:

$$\dot{Q} = UA(T_{surface} - T_{coolant}) = \frac{T_{surface} - T_{coolant}}{\sum R_{rod}} \tag{3.5}$$

Since the HTC is not known, and thus the amount of condensation is also unknown, the amount of vapour available to condensate should be enough to facilitate every (reasonable) HTC. As the latent heat of vapourisation differs between fluids, the amount of vapour is unique. The liquid flow to the evaporator was found iteratively by looking at the vapour quality after the condensation chamber. For R245fa, the liquid flow needed is $50\,\mathrm{mL/min}$, for R717 this is $15\,\mathrm{mL/min}$. Resulting in a vapour quality after the condensation chamber higher than 0.4 for all pressures and HTCs in the defined range. More elaboration on the simulation of the test section can be found in Chapter A. The relevant results are shown in Figures 3.11 to 3.12.

Figure 3.11 shows the heat flow to the condensation surface in the condensation chamber at different pressures and HTCs. The saturation temperature is low at lower pressures and the coolant is limited to $5\,^\circ\mathrm{C}$. Therefore, for most HTC's the total heat flow rises with pressure. Once it stabilises, coolant

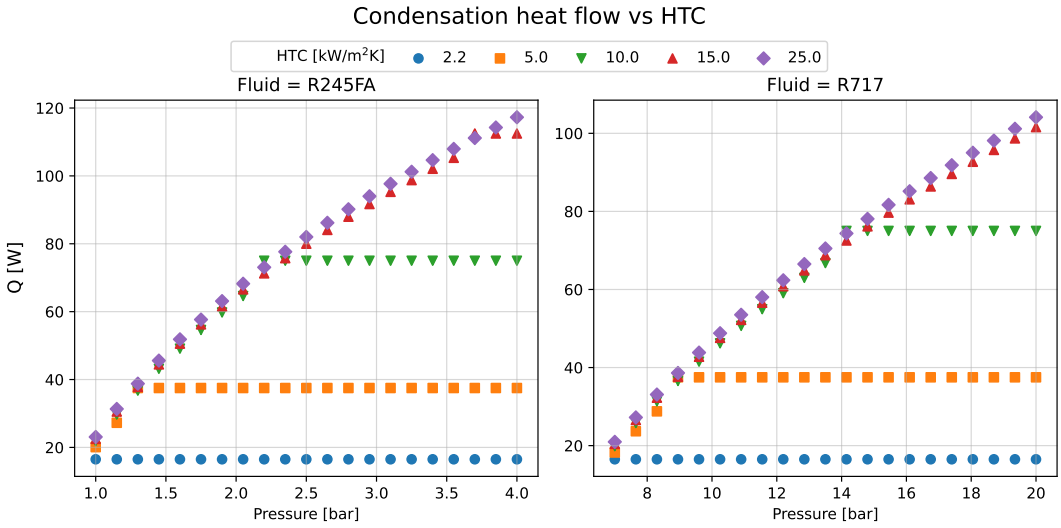

Figure 3.11: Simulated heat transfer by condensation at different pressures.

temperature can facilitate the desired degree of subcooling ($3\,\mathrm{K}$). For a HTC of $2.2\,\mathrm{kW/(m^2\,K)}$, the cooling temperature allows for the desired degree of subcooling at every pressure. For $15.0\,\mathrm{kW/(m^2\,K)}$ and $25.0\,\mathrm{kW/(m^2\,K)}$, the coolant temperature limits the degree of subcooling and does not allow for stabilisation of the heat flow.

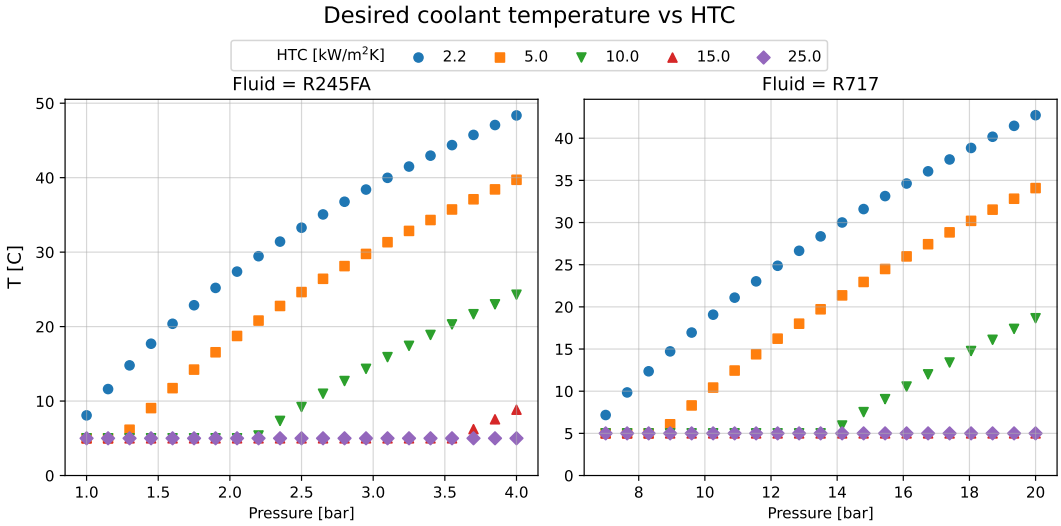

Figure 3.12: Simulated desired coolant temperature at different pressures.

This effect is shown in Figure 3.12, here the desired coolant temperatures are shown for different pressures and HTCs. For $2.2\,\mathrm{kW/(m^2\,K)}$, $5.0\,\mathrm{kW/(m^2\,K)}$ and $10.0\,\mathrm{kW/(m^2\,K)}$, the coolant temperature does allow for the desired degree of subcooling of $3\,\mathrm{K}$ in both fluids from a certain pressure. Again, for $15\,\mathrm{kW/(m^2\,K)}$ and $25.0\,\mathrm{kW/(m^2\,K)}$, the coolant is (mostly) bounded to $5\,^{\circ}\mathrm{C}$ for both fluids.

Resulting from the heat transfer rate, a temperature difference should be measured between the measurement points. Figure 3.13 shows the expected temperature difference measured across the measurement section for different pressures and HTCs. As shown, the temperature difference is measurable. The temperature differences stabilises when the desired degree of subcooling is reached, as this stabilises the heat transfer rate. At increased HTCs, the measurable temperature difference is increased due to enhanced heat transfer rates.

The heat load of the electric evaporator for different pressures and HTCs is shown in Figure 3.14. As the

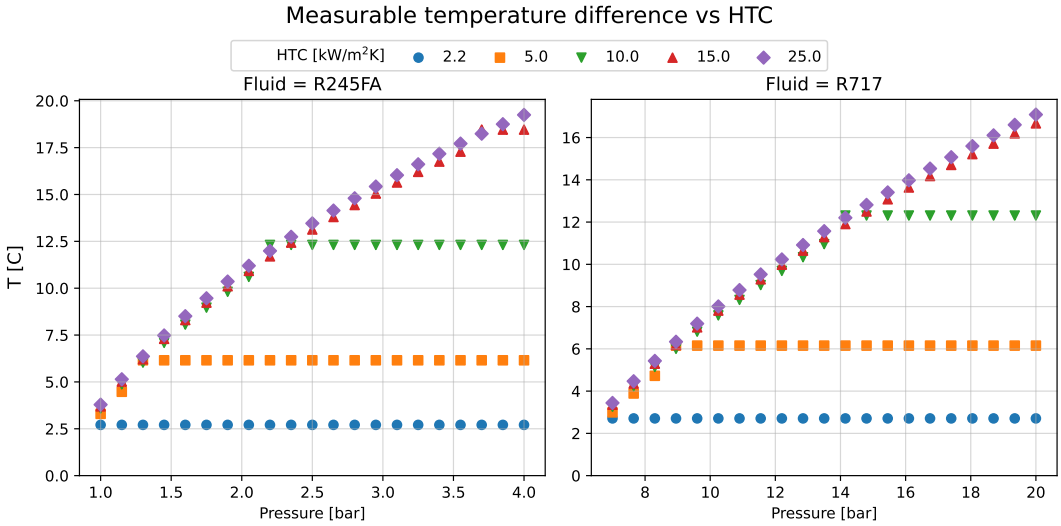

Figure 3.13: Simulated expected temperature difference measurement at different pressures.

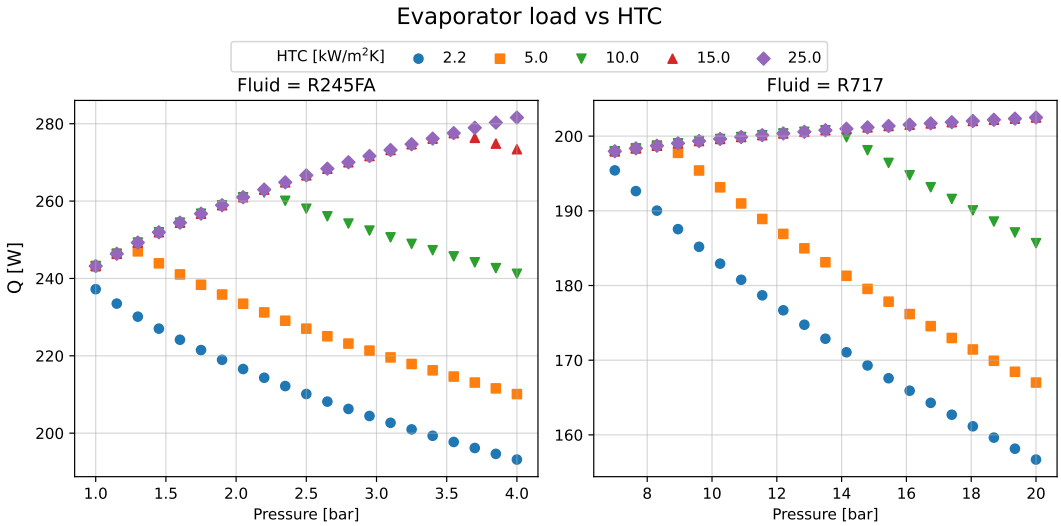

Figure 3.14: Simulated evaporator load at different pressures.

temperature of the liquid entering the evaporator is dependent on the coolant temperature (Figure 3.12) and the saturation temperature increases with pressure, the heat load of the evaporator rises at first. When the coolant temperature is not bounded to the limit, the heat load changes and decreases as the latent heat of vapourisation declines with pressure.

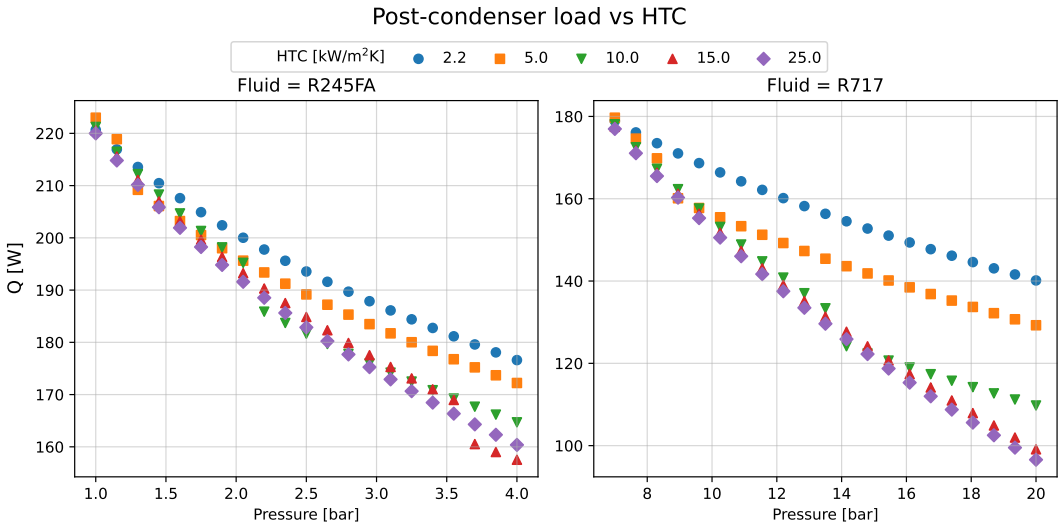

Figure 3.15: Simulated post-condenser load at different pressures.

Similarly, the heat load of the post-condenser for different pressures and HTCs is shown in Figure 3.15. The heat load stabilises when the coolant temperature can increase (Figure 3.12). Before this, the heat load shows a strong decrease because of increased condensation due to increased heat flow rates at higher pressures (Figure 3.11).

3.7. Pressure control

The setup dynamics discussed before elaborate the energy flows when system is in steady state, meaning that the pressure is constant. However, experiments are to be conducted at different pressures, so controllability is required.

At steady state, the heat input of the evaporator is equal to the heat flow in the test-section and post-condenser. This way, the temperature of the system is steady. To reach different pressures, the reduced second law of thermodynamics is utilized[4]:

$$\frac{dU}{dt} = \dot{Q}_{\text{net}} \tag{3.6}$$

Here, U is the internal energy (in [J]), which changes with time (t in [s]). The net heat supplied to the system is noted by $\dot{Q}_{\text{net}}$ (in [W]). The change in internal energy of the system is equal to: $dU = mc_v dT$. Here, m is the total mass of the system (in [kg]), c_v is the specific heat at constant volume (in [J/(kg K)]), and dT is the temperature change (in [K]).

By applying excess heat to the system by the evaporator, the net heat is positive. This raises the internal energy of the system, and thus its temperature. Pressure is directly related to temperature, therefore the pressure of the system is increased. Similarly, when applying a shortage of heat, the net heat is negative. Therefore, the internal energy is decreased. Resulting in lowering the temperature and pressure.

So, the pressure of the system can be controlled by the balance of energy input and rejection. Therefore, by governing the heat supplied by the evaporator, the pressure is controlled. This allows for the

[4]As the system is closed and fixed volume, no mass flow in or out is present and negligible work is done to the system. Therefore, the second law of thermodynamics is reduced to the change in internal energy and heat flow.

integration of a proportional-integral-derivative (PID) controller with the pressure sensor (P1) as the process variable.

However, to ensure proper operation of the PID-pressure controller, the evaporator should contain a significant proportion of the fluid available in the system. If not, the system can be to cold for increasing the internal energy to reach a new pressure.

3.8. Component manufacturing

The components of the test-section are manufactured according to the design. The measurement section and swappable surfaces are machined out of oxygen-free copper, the result is shown in Figures 3.16 to 3.17, respectively. These parts can be attached by fastening bolts to the flanges on the far ends. In addition, the condensation chamber, consisting of a view-glass, tube, and flange with a square hole, is welded together out of stainless steel, grade 316. The result is shown in Figure 3.18. The metal assembly of the condensation chamber is bulky, therefore this may require electrical heat tracing to prevent long transient states. Moreover, the cooling chamber is shown in Figure 3.19, all welded out of 316 stainless steel. Here, the fins of the measurement section are inserted on one side for cooling. The other side allows for access whenever needed. The saturation tank, welded from 316 grade stainless steel parts, is shown in Figure 3.20. The evaporation takes place on the reduced diameter side, inside also baffles are present to enhance mixing. The large diameter part includes a view-glass to visually check the level in the tank.

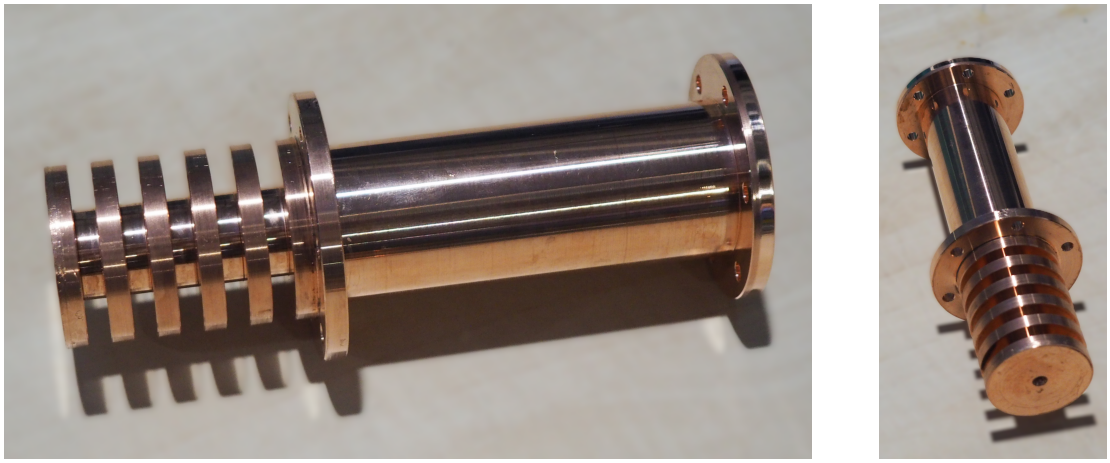

Figure 3.16: Manufactured copper measurement section, no temperature sensors holed drilled yet. Of the rod; cooling fins on the left, measurement rod in the middle, and swappable surface attachment flange on the right.

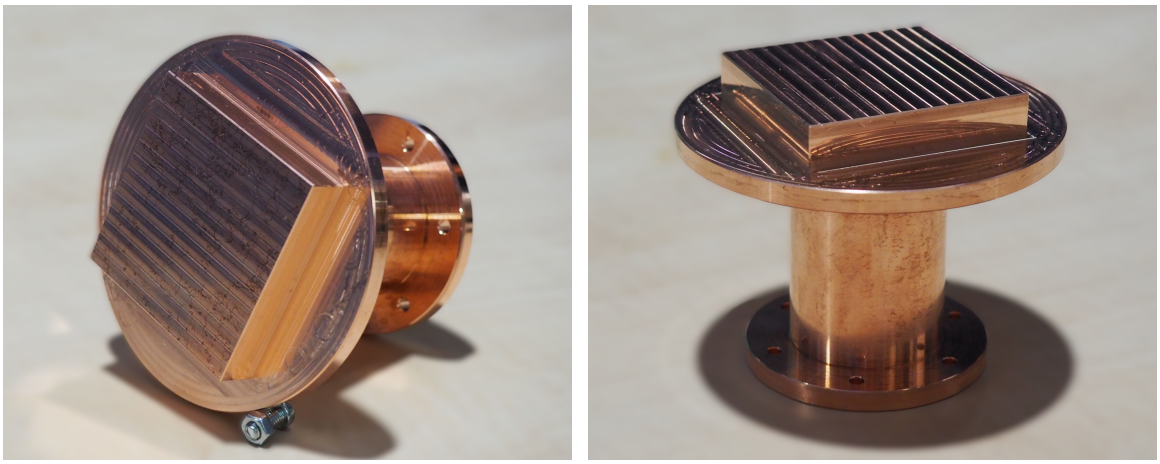

Figure 3.17: Manufactured copper swappable surface, no temperature sensor holes drilled yet. Including a square condensation surface, increased diameter squeeze flange, reduced diameter measurement section, and attachment flange for the measurement section.

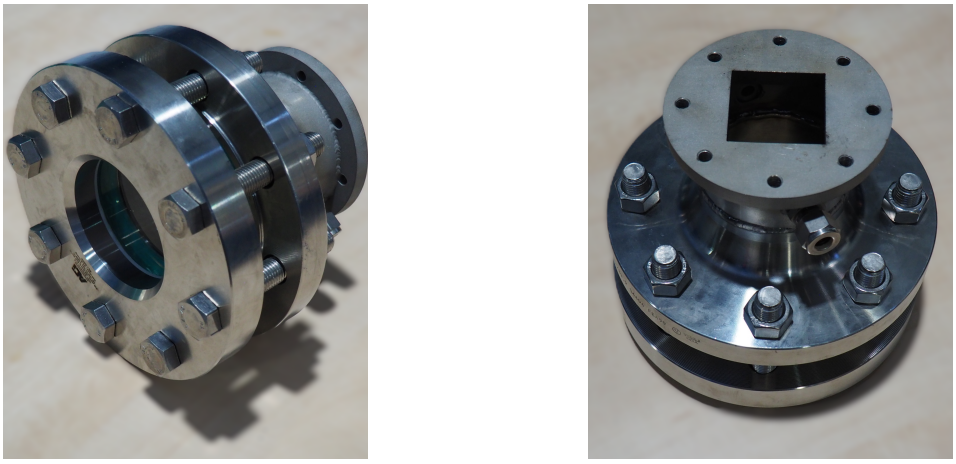

Figure 3.18: Manufactured condensation chamber. Here, the view-glass flange and the swappable surface flange (square hole) are welded to a tube. The sight-glass is attached by a fastened flange. Also, two tube fittings are welded on.

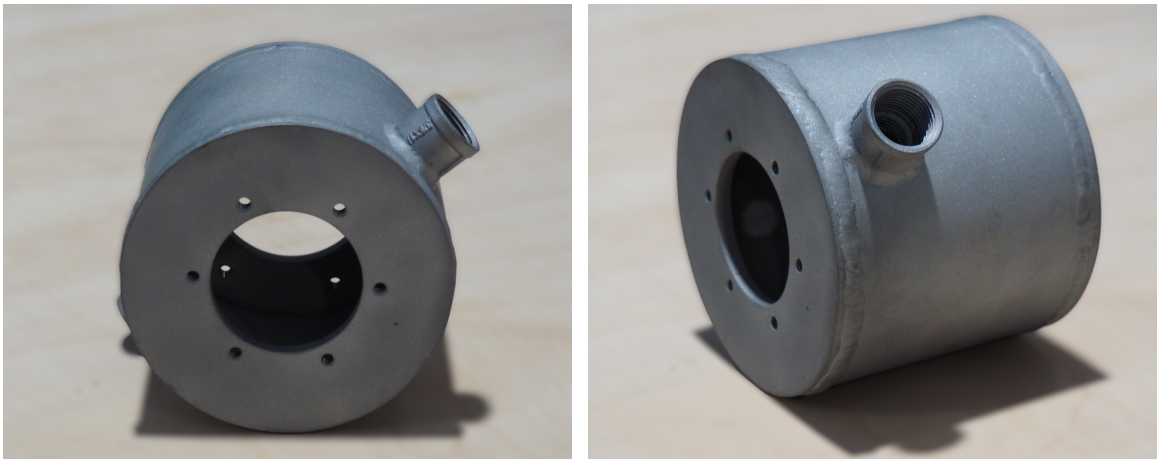

Figure 3.19: Manufactured cooling chamber. On one side, fins of the measurement section are inserted. The other side is closed by a plate. Two screw fittings are welded on to attach coolant hoses to.

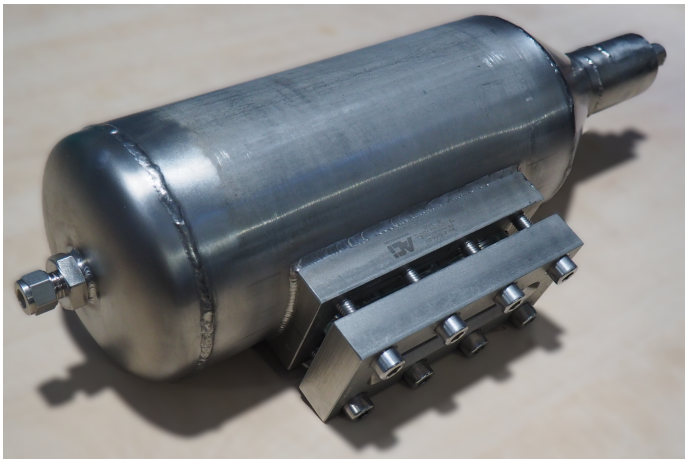

Figure 3.20: Manufactured saturation tank, the far end shows the reduced diameter for the evaporator. The rectangular attachment is a view-glass, and fittings are welded on both sides.

4

Methodology

The setup will be used to test multiple hydrophobic surfaces, the method on testing the hydrophobicity of these surfaces is discussed in Section 4.1. Next to this, the method of verifying the function of the setup is discussed in Section 4.2. Moreover, the uncertainty of the setup measurements is elaborated on in Section 4.3.

4.1. Measurement of contact angles

Several coatings are to be tested in the setup, some surfaces have already been manufactured on copper and aluminium substrates. To confirm its hydrophobicity with water and R245fa, the static and dynamic contact angles are measured.

4.1.1. Experimental surfaces

Three surfaces were received from `Nanyang Technological University of Singapore`. The first is a copper substrate with lubricant infused copper oxide nanostructures (referred to as: Cu-nano oxides). The second is an aluminium substrate with lubricant infused aluminium oxide nanostructures (Al-nano oxides). The third is also a aluminium substrate, the first tier are microstructures, the second tier are lubricant infused aluminium nanostructures (Al-micro & nano oxides). These surfaces are visualized in a scanning electron microscope (SEM). The resulting (micro &) nanostructures are shown in Figure 4.1. The infused lubricant is Krytox VFP 1525, for the fabrication of the surfaces, please refer to Chapter B

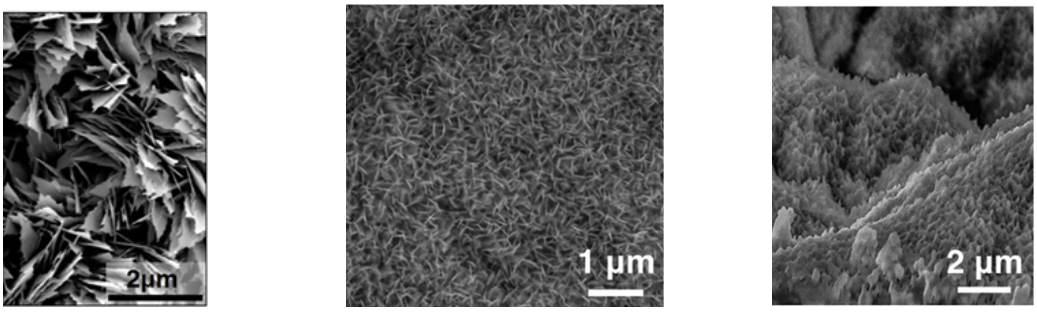

(a) Cu-nano oxides **(b)** Al-nano oxides **(c)** Al-micro & nano oxides

Figure 4.1: Nanostructures of experimental surface coatings in SEM [67, 68, 69, 70]

4.1.2. Experimental procedure

To measure the contact angle repeatedly with droplets of the same volume, an automatic dosing device is needed. Also, a camera should be steadily in place to capture the sessile droplet. Such a measurement device is shown in Figure 4.2. The device available is manufactured by `DataPhysics Instruments GmbH`.

(a) Overview **(b)** Close-up

Figure 4.2: Measurement device for automatic dosing of droplets and determining the (dynamic) contact angles.

Water measurements: On every surface, the static contact angle measurements are taken on different 5 different spots on the surface, with a droplet size of $2\,\mu\mathrm{L}$. For the dynamic contact angle measurements the droplet base size is $20\,\mu\mathrm{L}$, with a growth (and shrinking) rate of $0.4\,\mu\mathrm{L/s}$, up to $20\,\mu\mathrm{L}$. For dosing from or to the droplet, a needle of the measurement device is pushed into the droplet. This way, fluid can be added or removed from the droplet. This is repeated 5 times, the needle is $0.2\,\mathrm{mm}$ in diameter.

R245fa measurements: Due to the timeline of the project, no measurements have been conducted with R245fa. Considering the saturation temperature at atmospheric pressure ($14\,^\circ\mathrm{C}$–$15\,^\circ\mathrm{C}$), a similar experiment can be conducted in an environmental chamber to prevent evaporation of the fluid during experiments.

4.2. Computational conduction modelling of geometry.

To verify the chosen design of the swappable surface and measurement section, a computational model to determine the temperature profile is made in ANSYS, specifically the `Steady-State Thermal` toolbox. However, the boundary conditions need to be defined, four external heat flows in this case. From right to left (Figure 4.3): first the condensation on the condensation surface, then the surface resistance due to thermal paste between te parts and at the end the cooling in the cooling chamber. The heat flow from/to the environment is the forth.

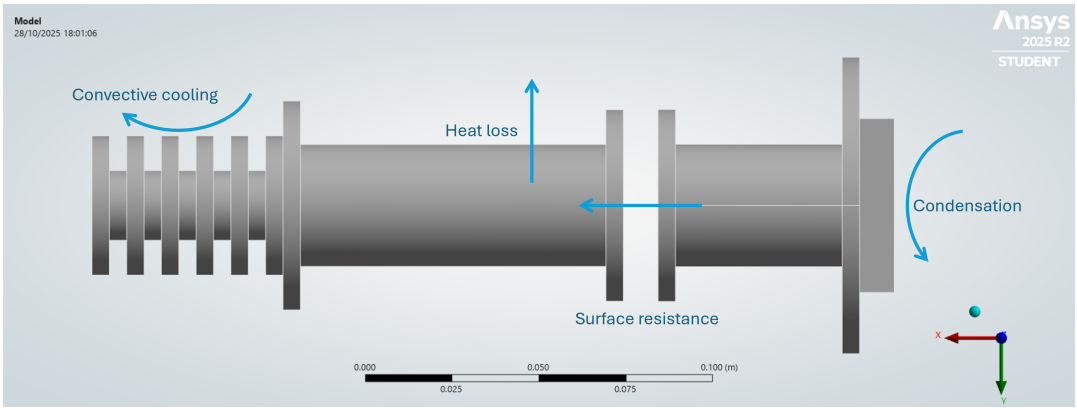

Figure 4.3: Visualised boundary conditions for the computational model. Convective cooling to the coolant on the left. Heat loss to the environment over the whole geometry. Surface resistance between the two parts. And, condensation on the right side.

In the setup, the goal is to measure the centreline temperature of the geometry. Therefore, a PATH is added to show the temperature profile along the centreline of the rod. By interpolation, the temperature at the measurement holes can be determined. Moreover, the average temperature of the condensation surface is determined by the computational model, this allows for accurate determination on the heat flow into this surface.

4.2.1. Boundary conditions

The said boundary conditions are explained and quantified accordingly:

Condensation: The saturation temperature of the vapour in condensation has been set to $45\,^{\circ}\mathrm{C}$. The equivalent saturation pressure for R245fa is $3\,\mathrm{bar}$, and for R717 that is $18\,\mathrm{bar}$. The same HTC's are used as in the simulation of the setup before: $2.2\,\mathrm{kW/(m^2\,K)}$, $5\,\mathrm{kW/(m^2\,K)}$, $10\,\mathrm{kW/(m^2\,K)}$, $15\,\mathrm{kW/(m^2\,K)}$ and $25\,\mathrm{kW/(m^2\,K)}$.

Cooling: For each HTC of condensation, a desired coolant temperature as function of pressure has been determined. Here, a cooling convective HTC should also be applied. The working fluid is water, and is forced through the cooling chamber at $5\,\mathrm{L/min}$. Due to entrance effects and the shape of the geometry, the flow can be turbulent. Literature gives a HTC of $500\,\mathrm{W/(m^2\,K)}$, for laminar forced convection in tubes [71, 72]. Making this the lower limit for the convective HTC in the cooling chamber. The chosen cooling temperatures are $40\,^{\circ}\mathrm{C}$, $30\,^{\circ}\mathrm{C}$, $15\,^{\circ}\mathrm{C}$, $5.0\,^{\circ}\mathrm{C}$ and $5.0\,^{\circ}\mathrm{C}$ for each HTC, respectively.

To show the behaviour of the temperature at the centreline, also several cooling temperatures are set for every HTC. These cooling temperatures are $40\,^{\circ}\mathrm{C}$, $25\,^{\circ}\mathrm{C}$, $10\,^{\circ}\mathrm{C}$ and $5\,^{\circ}\mathrm{C}$ and will determine the measurable temperature difference at different cooling temperatures and HTC's.

Thermal surface resistance: Thermal paste is to be applied between the swappable surface and measurement section. The paste available has a thermal conductivity of $8\,\mathrm{W/(m\,K)}$. The parts can be fastened together by bolts, here an effective thermal paste thickness of $0.1\,\mathrm{mm}$ is assumed. That results in a thermal conductance (inverse of resistance) of $80 \times 10^3\,\mathrm{W/(m^2\,K)}$.

Environmental heat or cooling: If the test-section is wrapped in $10\,\mathrm{cm}$ of rockwool, the effective heat transfer coefficient to the environment can be determined. For rockwool the thermal conductivity is roughly $0.04\,\mathrm{W/(m\,K)}$ at room-temperature of $25\,^{\circ}\mathrm{C}$[73]. Therefore the effective HTC for insulation loss is $0.4\,\mathrm{W/(m^2\,K)}$[1]. However, to allow for error margin and variable thickness of insulation, the effective HTC is set to $1.0\,\mathrm{W/(m^2\,K)}$.

4.2.2. Meshing

The meshing of the geometry is second order (quadratic) with a (normal) base element size of $1\times10^{-2}\,\mathrm{m}$. To verify meshing independency, also a coarser meshing of $2\times10^{-2}\,\mathrm{m}$ and a finer meshing of $5\times10^{-3}\,\mathrm{m}$ are applied. Then, the absolute difference along the centreline of the coarse and normal meshing compared to the fine meshing are determined. Chapter C shows additional meshing settings and the resulting meshing.

4.2.3. Summarized parameters

All parameters and factor discussed before are summarized in Table 4.1.

Table 4.1: Computational model settings and boundary conditions with regards to condensation, surface resistance, heat loss, and cooling.

Property	Setting/value
Saturation temperature	$45\,^{\circ}\mathrm{C}$
R245fa saturation pressure equivalent	$2.94\,\mathrm{bar}$
R717 saturation pressure equivalent	$17.82\,\mathrm{bar}$
HTC cooling	$0.5\,\mathrm{kW/(m^2\,K)}$

[1]The effective conductance equals the ratio of thermal conductivity and length scale ($U = k/L$)

Property	Setting/value
HTC insulation	$1.0\,\mathrm{W/(m^2\,K)}$
Ambient Temperature	$15\,^\circ\mathrm{C}$
Surface conductance	$80\,\mathrm{kW/(m^2\,K)}$
Mesh element size	$1 \times 10^{-2}\,\mathrm{m}$
Material	Oxygen-free Electronic Copper
Thermal conductivity material	$391\,\mathrm{W\,K/m}$
HTC condensation	$2.2\,\mathrm{kW/(m^2\,K)}$
Coolant temperature	$40\,^\circ\mathrm{C}$
HTC condensation	$5.0\,\mathrm{kW/(m^2\,K)}$
Coolant temperature	$30\,^\circ\mathrm{C}$
HTC condensation	$10.0\,\mathrm{kW/(m^2\,K)}$
Coolant temperature	$15\,^\circ\mathrm{C}$
HTC condensation	$15.0\,\mathrm{kW/(m^2\,K)}$
Coolant temperature	$5\,^\circ\mathrm{C}$
HTC condensation	$25.0\,\mathrm{kW/(m^2\,K)}$
Coolant temperature	$5\,^\circ\mathrm{C}$
Other coolant temperatures	$40.0\,^\circ\mathrm{C}$, $25.0\,^\circ\mathrm{C}$, $10.0\,^\circ\mathrm{C}$ and $5.0\,^\circ\mathrm{C}$

4.3. Sensor and heat transfer coefficient uncertainty analysis

Before experimental research can be conducted, the expected uncertainty due to sensor errors should be determined in advance. This will show if the chosen sensors and components are sufficient for experimental estimation of the HTC. Here, the temperature measurements in the rod, temperature sensor in the gas and the pressure sensor will serve as inputs for a one-dimensional model for estimating the HTC. The values found in the computational model mentioned before will serve as hypothetical numerical inputs for these sensors. Moreover, the sensors include a possible error range quantified by the manufacturer. This allows for uncertainty analysis to provide context to the estimated HTC. In this case, only uncertainty due to sensor errors can be obtained (Type B). The uncertainty due to measurement variations should be included after the experiments (Type A). The `GUM` [74] is used as a reference.

4.3.1. Sensor error and uncertainty

The sensor mentioned have a distinct error in their sensor reading, as shown in Table 4.2. As every value within the error limits has the same probability of being the actual value, an uniform or rectangular distribution is assumed. Therefore the uncertainty in the first confidence interval ($\sigma = 1$; $58\,\%$ confidence) of the sensor is found as:

$$u^2(x_i) = \frac{\varepsilon_i^2}{3} \tag{4.1}$$

Here, x_i is the parameter in question, ε_i is the error of this parameter and u is the uncertainty.

Table 4.2: Sensor error quantified by the manufactured relevant to HTC estimation.

Reference	Measurement, symbol	Error, ε	Additional information
TS01-04	Temperature, $T_{[1:4]}$	$\pm(0.3 + 0.005 \times \lvert T\rvert)$	Can be calibrated[2].
TS05-06	Temperature, $T_{[5:6]}$	$\pm(0.3 + 0.005 \times \lvert T\rvert)$	

[2]By calibrating these sensors at the same temperatures, the offset error (0.3) can be taken out. This results in a comparative/relative temperature reading, instead of an absolute. The temperature related error (0.005) remains.

Reference	Measurement, symbol	Error, ε	Additional information
TS07	Temperature, T_7	$\pm 1/10(0.3 + 0.005 \times \lvert T \rvert)$	
PS01	Pressure, P	$\pm 0.3\% P_{max}$	For R245fa: $P_{max} = 5\text{bar}$; for R717: $P_{max} = 25\text{bar}$

The sensor uncertainty is then used in equations to find the uncertainty of its product. Here y is the product of a function with sensor readings x as its input:

$$y = f(x) \qquad x = \{x_1, x_2, ..., x_N\} \tag{4.2}$$

To find the uncertainty of y, the equation below is used:

$$u^2(y) = \sum_{i=1}^{N} \left(\frac{\delta f}{\delta x_i} \right)^2 u^2(x_i) \tag{4.3}$$

4.3.2. Estimation of HTC and uncertainty

Based on sensor readings, the HTC can be estimated with a one dimensional model. As the sensor contain a possible error, also an uncertainty analysis is conducted into the HTC of condensation. The estimation and uncertainty is divided in four steps: 1) Estimation and uncertainty analysis of the total heat transfer, 2) Estimation and uncertainty analysis of the condensation wall temperature, 3) Estimation and uncertainty analysis of the saturation temperature of the vapour, and 4) Estimation and uncertainty analysis of the HTC. How these relate to the sensor readings of Table 4.2 is shown below. Certain functions also take the uncertainty in determining the length between temperature point into account (L):

$$\begin{aligned} \dot{Q} &= f\left(T_{[1:4]}, L_{[1:4]}\right) \\ T_w &= f\left(\dot{Q}, T_{[5:6]}, L_{[5:6]}\right) \\ T_{sat} &= f\left(P, T_7\right) \\ HTC &= f\left(\dot{Q}, T_w, T_{sat}\right) \end{aligned} \tag{4.4}$$

The exact functions and their application into the determining the uncertainty (Equation (4.3) is shown in Chapter D. The computational analysis of the setup results in hypothetical temperature measurements in the rod. These, and the settings for the saturation pressure and temperature, will be used as inputs to estimate the HTC and its uncertainty for different states.

5 Results

5.1. Contact angle results

The software associated with the measurement device determines the contact angle of a sessile droplet on the surface with the help of a photo. This results in figures such as the ones shown in Figure 5.1. Due to surface irregularities the droplet may have a different contact angle all around the base, (left & right in 2D). Therefore the mean between the left and right contact angle is used as a result.

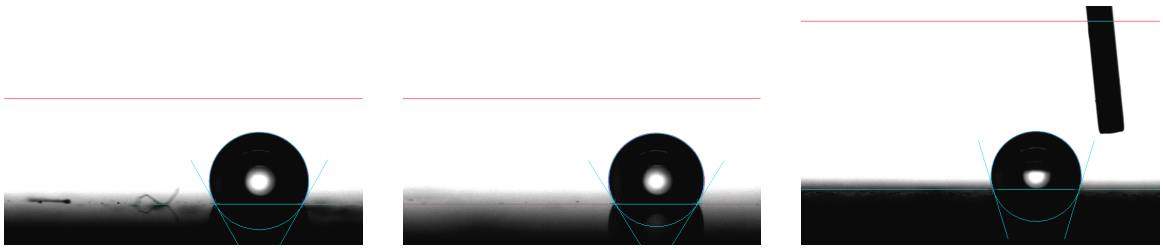

(a) Cu-nano oxides
CA left: $119.0°$, CA right: $119.0°$.

(b) Alu-nano oxides
CA left: $121.6°$, CA right: $121.6°$.

(c) Alu-micro & nano oxides
CA left: $106.8°$, CA right: $106.7°$.

Figure 5.1: Contact angle result figures of water on the test surfaces, with measured contact angle left and right.

From the measurements from each surface the mean contact angle is determined, as well as the standard deviation. The size of the data set is very small, only 5 measurements per surface. Therefore the standard deviation shows the approximation range of the contact angle.

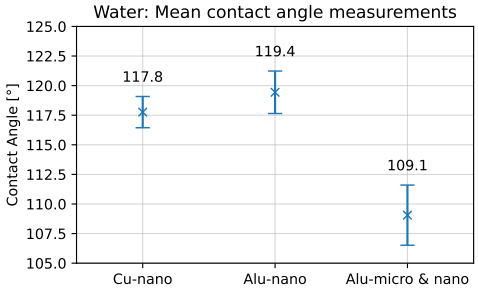

Figure 5.2: Static contact angle results for water on each surface.

These results are shown in Figure 5.2. Here the Alu-nano surface has the largest contact angle with water, approximately $119°$. The Cu-nano surface has a contact angle of approximately $118°$. Moreover, the Alu-micro & nano surface shows the lowest contact angle, at approximately $109°$ and the highest standard deviation. All contact angles are shown in Chapter B. All surfaces prove to by very hydrophobic, this was expected, as the surfaces were purposely fabricated.

For the dynamic contact angle measurements, advancing and receding contact angle must be manually extracted from the software measurements data. The advancing angle exists when the base-diameter of the droplet expands. Its receding counterpart should occurs when the base-diameter shrinks, but after a short pause. The raw measurements results are available in Chapter B.

Unfortunately, while the droplet grows or shrinks on the surface the contact angle measurements are dispersed. Therefore, no clear receding or advancing contact angle can be extracted from the measurement data. The following can be observed: in dynamics measurements, all contact angles observed were lower than the static contact angle measurement. Moreover, the overall contact angle differences during the dynamic measurements were rather low. Only approximately $3°$ for the Cu-nano surface, approximately $4°$ for the Alu-nano surface and approximately $6°$ for the Alu-micro & nano surface. Therefore, the hysteresis of water on these surfaces is very low.

5.2. Verification of setup performance

The result of the conduction calculation are visualized in contours showing the temperature profile along the surface of the geometry. Such a figure is shown in Figure 5.3, for a HTC of $10\,\mathrm{kW/(m^2\,K)}$. In this case a surface subcooling of roughly $1.6\,\mathrm{K}$ is reached, and the temperature difference along the geometry is $25\,\mathrm{K}$. The temperature difference between the cooling fins' surface and the coolant is $3.3\,\mathrm{K}$.

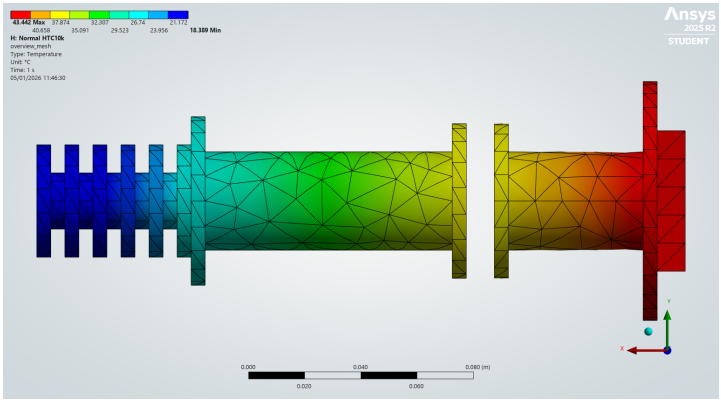

Figure 5.3: Surface temperature contour of the geometry with a condensation HTC of $10\,\mathrm{kW/(m^2\,K)}$ (normal meshing).

5.2.1. Centreline temperature profiles

The computational model results in a theoretical temperature profile along the centreline for fixed temperatures at the refrigerant and coolant side. This allows to check the temperatures and temperature differences that will be measured by the sensors and can thus be used to estimate the corresponding HTC and uncertainty. First, the centreline temperature profiles based on the determined coolant temperature based on the HTC are discussed. Then, results regarding different coolant temperatures for every HTC are shown.

Figure 5.4 shows the centreline temperature profiles for $2.2\,\mathrm{kW/(m^2\,K)}$ and $10.0\,\mathrm{kW/(m^2\,K)}$. In Chapter C the plots for the other HTCs are shown. These plots show the condensations surfaces subcooling relative to the saturation temperature. For all HTCs and corresponding coolant temperature, the degree of subcooling is between $1\,\mathrm{K}$–$2\,\mathrm{K}$. As of the measurement points, for $2.2\,\mathrm{kW/(m^2\,K)}$ all temperatures are very close to each other, all within $41.6\,°\mathrm{C}$–$43.2\,°\mathrm{C}$. When the HTC is increased, and the temperature difference between the saturation temperature and the coolant temperature grows, the range of temperature at the measurement points increases. For example, for $10.0\,\mathrm{kW/(m^2\,K)}$ the temperature range at the measurement points is $27.3\,°\mathrm{C}$–$39.3\,°\mathrm{C}$. This can be explained by the fact that a larger HTC allows for more heat transfer into the condensation surface, all heat must transfer through the same cross-sectional area at the measurement point. Fourier's law of conduction requires that the temperature difference increases. Moreover, the overall temperature difference over the geometry is larger due to a lower coolant temperature.

Moreover, a temperature drop across the surface gap can be observed. At lower HTCs this is a very

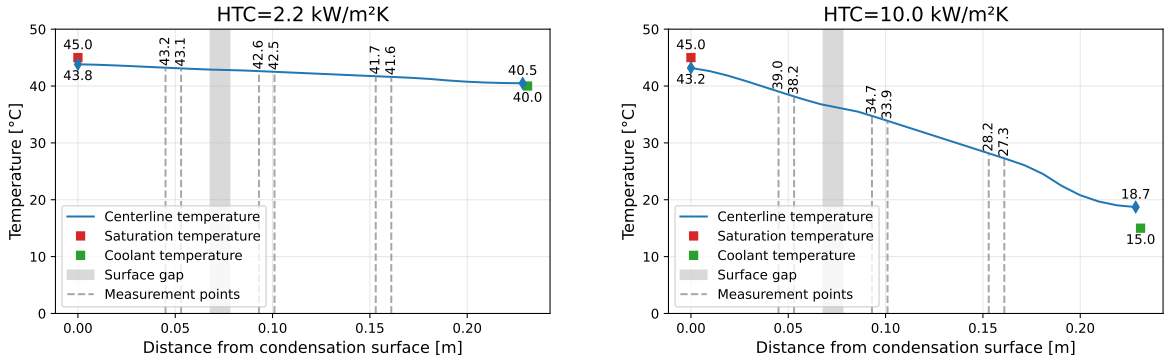

Figure 5.4: Centreline temperature profile of HTCs $2.2\,\mathrm{kW/(m^2\,K)}$ and $10.0\,\mathrm{kW/(m^2\,K)}$based on desired coolant temperature, including measurement points and surface gap.

slight drop, but it becomes more noticeable when looking at the higher HTC temperature profile. This can also be explained by the increase of heat transfer and larger temperature differences at higher HTCs.

As the HTC increases, the temperature difference between the end of the geometry and the coolant increases. At $2.2\,\mathrm{kW/(m^2\,K)}$ this difference is only $0.5\,\mathrm{K}$, but at $10.0\,\mathrm{kW/(m^2\,K)}$ this is increased to $1.7\,\mathrm{K}$ and at $25.0\,\mathrm{kW/(m^2\,K)}$ it is $5.1\,\mathrm{K}$. This means that effectiveness of cooling at the lower HTCs is sufficient with regards to the heat transfer area. However, at higher HTCs, either the area should be increased to reach lower surface temperatures or the cooling HTC should be increased.

One last noticeable characteristic about the temperature profiles is that it is curved in some areas and in some not. This this is due to the change in geometry of the swappable surface and measurement sections. Where the temperature profile appears to be linear, the cross sectional area is constant.

The result above are important to verify the calculation method in designing the setup. However, as the HTC is not known during experiments, a cooling temperature is chosen first. Then the degree is subcooling and HTC is determined. Therefore plotting the temperature profiles along the centreline for different cooling temperatures and HTC proves to be interesting.

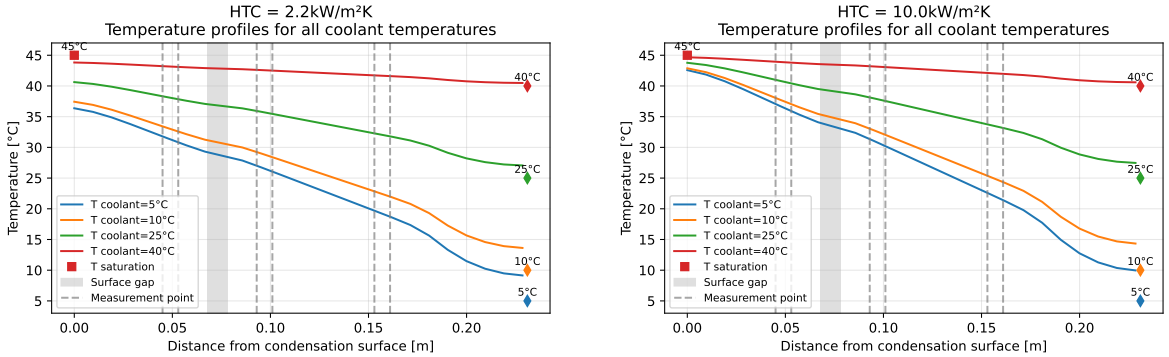

Figure 5.5: Centreline temperature profiles of HTCs $2.2\,\mathrm{kW/(m^2\,K)}$ and $10.0\,\mathrm{kW/(m^2\,K)}$for different coolant temperatures, including measurement points and surface gap.

Figure 5.5 shows the temperature profiles along the centreline for all set coolant temperatures and for an HTC of $2.2\,\mathrm{kW/(m^2\,K)}$ and $10.0\,\mathrm{kW/(m^2\,K)}$. Chapter C shows the same plots for all HTCs computed. As shown for an HTC of $2.2\,\mathrm{kW/(m^2\,K)}$, the degree of subcooling increases with a lower coolant temperature. This allows for more heat transfer into the condensation surface, therefore the temperature difference between the fins and the coolant increases relative to higher coolant temperatures. Moreover, due to the increase temperature difference between the far ends of the geometry, the temperatures at the measurement points lay in a greater range.

For an HTC of $10.0\,\mathrm{kW/(m^2\,K)}$ and others, similar effects are noticeable. However, the degree of subcooling is drastically decreased. Still, the total heat transfer is larger than at the lower HTCs, as is proven by the increased temperature difference at the end of the geometry and the coolant. However, this temperature difference is only slightly increased.

Moreover, the plotting of the temperature profiles along the centreline for all coolant temperatures and HTC proves the importance of the measurement in the swappable surface. As the temperature difference between measurement points are similar for different HTCs and the same coolant temperature are in close proximity to each other, an accurate determination of the condensations surface temperature is needed to accurately determine the HTC of condensation.

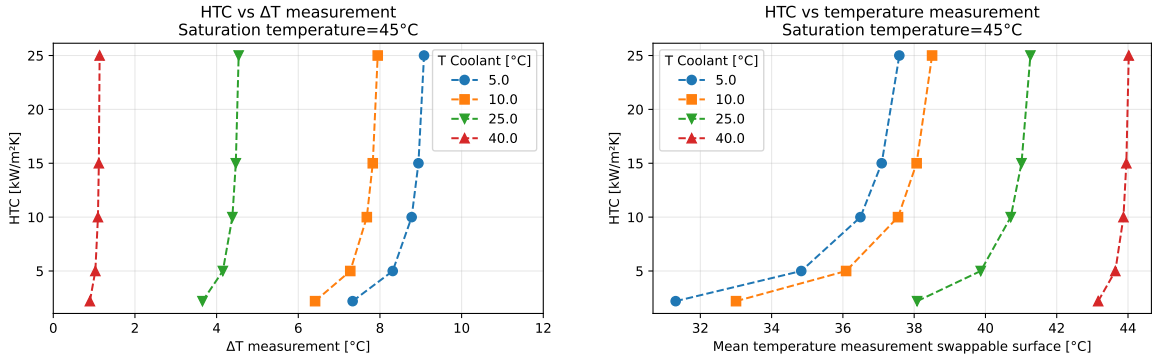

(a) Temperature difference to HTC relation.

(b) Temperature measurement to HTC relation.

Figure 5.6: Geometry temperature measurement points related to occurring HTC at different coolant temperatures.

Figure 5.6 shows this effect strongly. At higher coolant temperatures, the measurable temperature difference at all HTCs becomes small. At lower coolant temperatures, the measurable temperature difference increases (Figure 5.6a). As mentioned before, it is because of the increase in temperature difference between the far ends of the geometry, therefore increasing the heat transfer. As the measured temperature difference corresponds to a heat transfer through the rod, the temperature in the swappable surface is needed to determine the surface temperature (Figure 5.6b). This shows that at lower coolant temperature, there is a large variety in absolute temperature at the measurement points in the swappable surface. Therefore, each HTC has a distinct temperature at the condensation surface, allowing for determination of a unique HTC. At higher coolant temperatures, there is less variety. This makes sense due to a lower temperature difference between the far ends of the rod, meaning the range will be lower. This will result in less certain HTC determination. However, uncertainty analysis will show how certain the HTC estimation is.

5.2.2. Meshing dependency

The difference between the three meshing strategies is summarized in the absolute temperature difference at the centreline of the geometry. The absolute temperature difference is a result from interpolating the values of the fine meshing to the data points of the coarse and normal meshing. Then the coarse and normal values are subtracted from the fine meshing values.

Figure 5.7a shows the absolute difference between the fine and coarse meshing. It makes sense that an increased HTC results in a higher error, as the temperatures through the geometry span a larger range than smaller HTCs (Figure 5.4). Moreover, some distinct peaks are visible for every HTC relative to the rest of the data. These can be explained by the fact that the geometry changes over the length. Here the meshing itself differs significantly between meshing types. Therefore it is expected that the difference is enlarged here. In addition to this, the peak at the end of the geometry ($\geq 0.20\mathrm{m}$) occurs because of the geometry length-scale being smaller than the element size ($0.005\,\mathrm{m}$ of the geometry to $0.02\,\mathrm{m}$ of the coarse mesh). This causes less accurate determination of the heat transfer to the coolant.

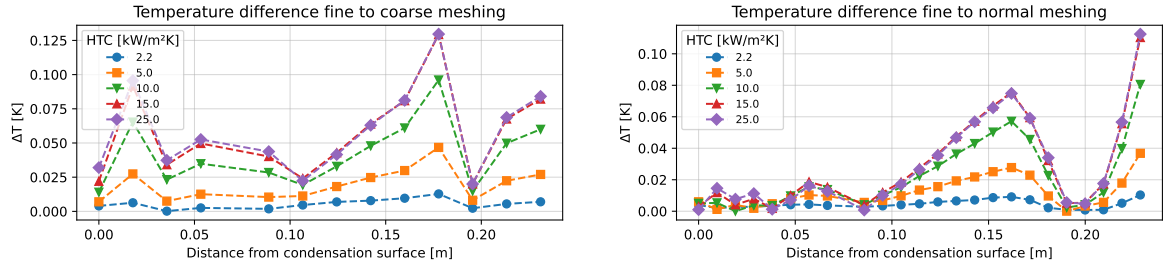

(a) Centreline temperature of coarse meshing compared to fine meshing.

(b) Centreline temperature of normal meshing compared to fine meshing.

Figure 5.7: Centreline temperature differences of normal and coarse meshing compared to the fine-meshing baseline.

5.3. Estimation and uncertainty analysis results

The one dimensional estimation and uncertainty functions of the heat transfer, saturation temperature, condensation wall temperature and ultimately the HTC can be read in Chapter D. Here the interpolated temperature measurements of the computational analysis are used as input in estimating the HTC and comparing it to the computational model settings.

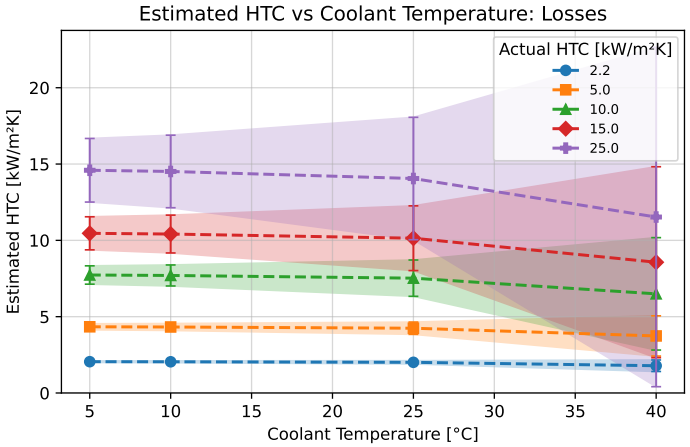

Figure 5.8: Estimated HTC with uncertainty based on computational-results ($\sigma = 1$). Each color represents the HTC used in the computational-modelling.

Figure 5.8 shows the estimated HTC and uncertainty range for every HTC input in the computational model. At a coolant temperature of $5\,^{\circ}\mathrm{C}$, the HTC estimations are $2.05\,\mathrm{kW/(m^2\,K)}$, $4.34\,\mathrm{kW/(m^2\,K)}$, $7.73\,\mathrm{kW/(m^2\,K)}$, $10.46\,\mathrm{kW/(m^2\,K)}$ and $14.59\,\mathrm{kW/(m^2\,K)}$ for their corresponding HTC respectively[1]. With an uncertainty ($\sigma = 1$) of $0.05\,\mathrm{kW/(m^2\,K)}$, $0.20\,\mathrm{kW/(m^2\,K)}$, $0.60\,\mathrm{kW/(m^2\,K)}$, $1.08\,\mathrm{kW/(m^2\,K)}$ and $2.08\,\mathrm{kW/(m^2\,K)}$. This means that the model is underestimating the HTC with regards to the input of the computational model. At other coolant temperatures ($10\,^{\circ}\mathrm{C}$, $25\,^{\circ}\mathrm{C}$ and $40\,^{\circ}\mathrm{C}$) the HTC is also underestimated. This effect is more severe at higher coolant temperatures. This is probably due to increased losses to the environment at higher temperatures. At high coolant temperatures, the average temperature of the rod is increased compared to lower coolant temperatures, therefore increasing heat loss to the environment.

The effect of losses are visualized in Figure 5.9, here the difference between the estimated heat transfer rate between measurement points and the actual heat transfer into the condensation surface is shown. At low coolant temperatures, the difference is very small, seen in very small over- or underestimation of the heat transfer rate. The error is increased for higher HTC values. At higher coolant values, the error lays in the same range as for lower coolant temperatures. However, due to a low total heat transfer, the relative difference is significant. As shown by increased relative errors up to $10\,\%$. Thus causing an increased underestimation at higher coolant temperatures.

[1] These are: $2.2\,\mathrm{kW/(m^2\,K)}$, $5.0\,\mathrm{kW/(m^2\,K)}$, $10.0\,\mathrm{kW/(m^2\,K)}$, $15.0\,\mathrm{kW/(m^2\,K)}$ and $25.0\,\mathrm{kW/(m^2\,K)}$

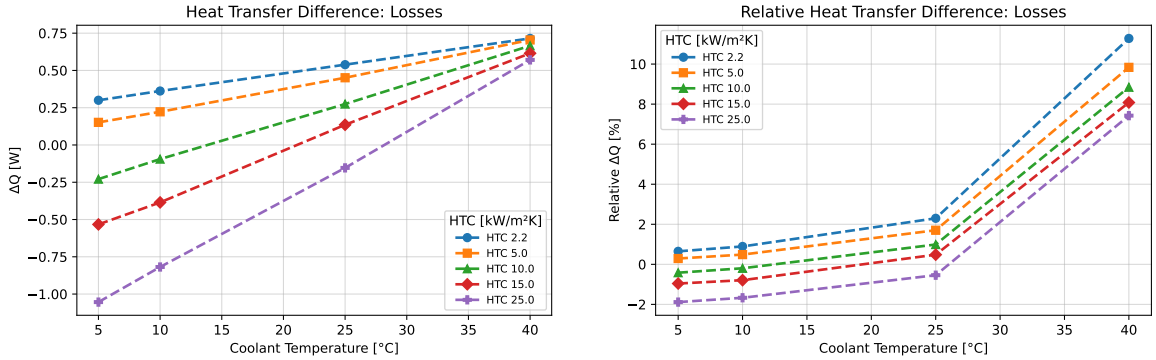

(a) Absolute difference

(b) Relative difference

Figure 5.9: Errors in estimated heat transfer as a function of coolant temperature.

This explains the increased underestimation of the HTC at increased coolant temperatures, the fault in estimated heat transfer is large here. For lower coolant temperatures, the fault in heat transfer estimation cannot cause this error alone. For this, the wall temperature estimation is explored.

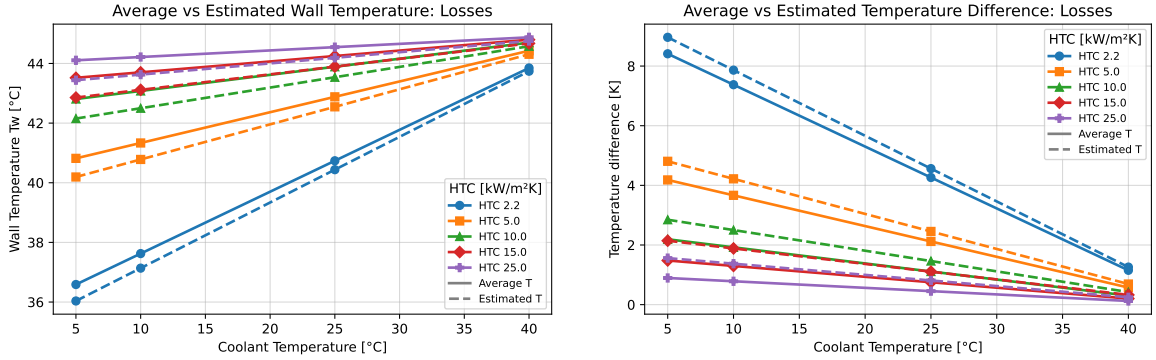

(a) Absolute temperature

(b) Difference with saturation temperature

Figure 5.10: Wall temperature estimation and relative to saturation temperature.

Figure 5.10 shows the estimated (centreline) wall temperature compared to the average wall temperature. The latter is needed for accurately determining the HTC. As shown, the wall temperature is underestimated from the actual wall temperature (Figure 5.10a). This increases the estimated degree of subcooling between the vapour and the condensation surface (Figure 5.10b). When applying the function for estimating the HTC, the result is decreased[2]. The wall temperature is estimated along the centreline of the geometry, thus one dimensional. However, the computational model is three dimensional. Therefore, the wall temperature of the condensation surface behaves differently.

Figure 5.11 shows the effect of a three dimensional model. At the centreline of the geometry, the temperature is the lowest (depicted in blue). At the corners of the condensation surface, the temperature is increased. At the conditions shown in the figure, the temperature is ranged over $40.63\,^{\circ}\mathrm{C}$–$40.80\,^{\circ}\mathrm{C}$ for HTC of $2.2\,\mathrm{kW/(m^2\,K)}$ and coolant temperature of $25\,^{\circ}\mathrm{C}$. For an HTC of $10\,\mathrm{kW/(m^2\,K)}$ and coolant temperature of $5\,^{\circ}\mathrm{C}$ the range is $42.58\,^{\circ}\mathrm{C}$–$42.93\,^{\circ}\mathrm{C}$. Therefore, a $0.17\,\mathrm{K}$ and $0.35\,\mathrm{K}$ temperature gradient exists over each condensation surface, respectively. Also, the estimated centreline temperature is still off by a view fractions of a degree: $0.31\,\mathrm{K}$ and $0.66\,\mathrm{K}$ for the figures shown, respectively.

[2] If the heat flow (Q) is accurately determined, the area (A) is known and the temperature difference (ΔT) is overestimated; the result is an underestimated HTC. This is because $HTC \propto 1/\Delta T$

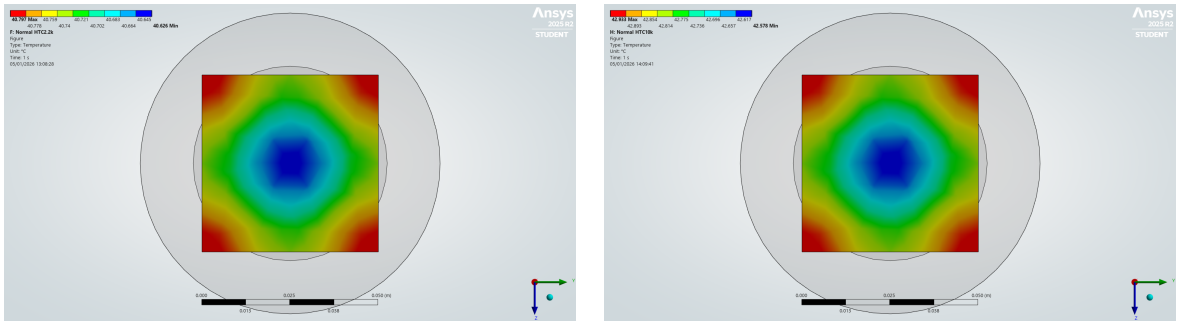

(a) Input: $HTC = 2.2\text{kW}/(\text{m}^2\,\text{K})$, $T_{coolant} = 25°\text{C}$; Results: $T_{w,avg} = 40.74°\text{C}$, $T_{w,est} = 40.44°\text{C}$

(b) Input: $HTC = 10.0\text{kW}/(\text{m}^2\,\text{K})$, $T_{coolant} = 5°\text{C}$; Results: $T_{w,avg} = 42.81°\text{C}$, $T_{w,est} = 42.15°\text{C}$

Figure 5.11: Temperature profile of condensation surface resulting from computational model under different inputs

To summarize, based on (interpolated) temperature readings at the measurement points in the geometry resulting from a computational model, the HTC is being underestimated. This is because the heat transfer taken place is overestimated, and the wall temperature of the condensation surface is underestimated, resulting in an underestimated HTC. To see if heat transfer losses to the environment play a significant role in the underestimation, the same computational model is conducted with no losses taken into account.

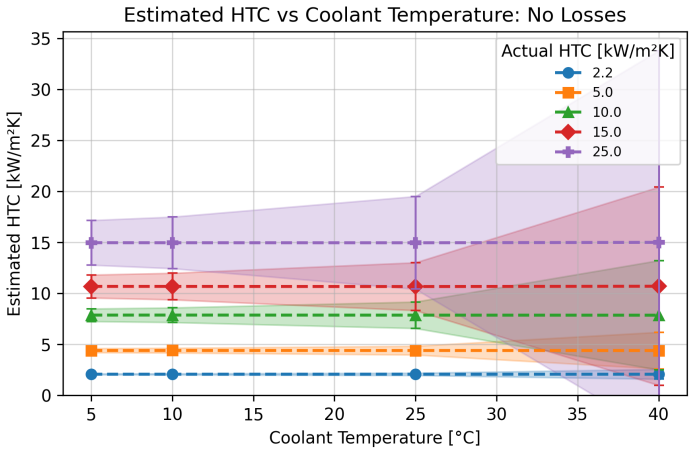

Figure 5.12: Estimated HTC with uncertainty based on computational model with no losses ($\sigma = 1$).

Figure 5.12 shows the estimated HTC at the condensation surface based on centreline temperatures with no losses taken into account. As shown, the estimated HTCs is at a coolant temperature of $5\,°\text{C}$ are $2.07\,\text{kW}/(\text{m}^2\,\text{K})$, $4.40\,\text{kW}/(\text{m}^2\,\text{K})$, $7.87\,\text{kW}/(\text{m}^2\,\text{K})$, $10.69\,\text{kW}/(\text{m}^2\,\text{K})$ and $14.97\,\text{kW}/(\text{m}^2\,\text{K})$ for their corresponding HTC, respectively. These have an uncertainty of $0.05\,\text{kW}/(\text{m}^2\,\text{K})$, $0.20\,\text{kW}/(\text{m}^2\,\text{K})$, $0.62\,\text{kW}/(\text{m}^2\,\text{K})$, $1.13\,\text{kW}/(\text{m}^2\,\text{K})$ and $2.19\,\text{kW}/(\text{m}^2\,\text{K})$ at this coolant temperature, respectively. The estimation is approximately the same for every coolant temperature. This is expected, as no losses are present. Still, a sever underestimation is occurring. The uncertainty becomes is very significant at higher HTCs and coolant temperatures. Therefore experiments at these coolant temperatures should be avoided if an increased HTC is expected.

In Figure 5.13, the difference between the actual heat transfer and the estimated heat transfer without taking losses into account, also the relative fault is shown. In fact, the heat transfer is marginally overestimated, as shown in negative values for both the absolute and relative difference.

Figure 5.14 shows the wall temperature estimation and the average actual wall temperature, both absolute and relative to the saturation temperature. Here the issue persists: the wall temperature is underestimated thus increasing the temperature difference to the saturation temperature.

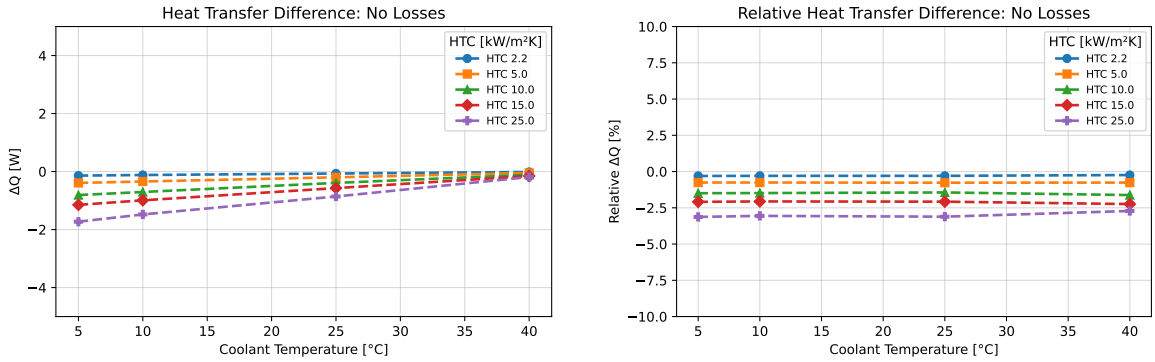

(a) Absolute difference

(b) Relative difference

Figure 5.13: Errors in estimating heat transfer as function of coolant temperature for model without losses.

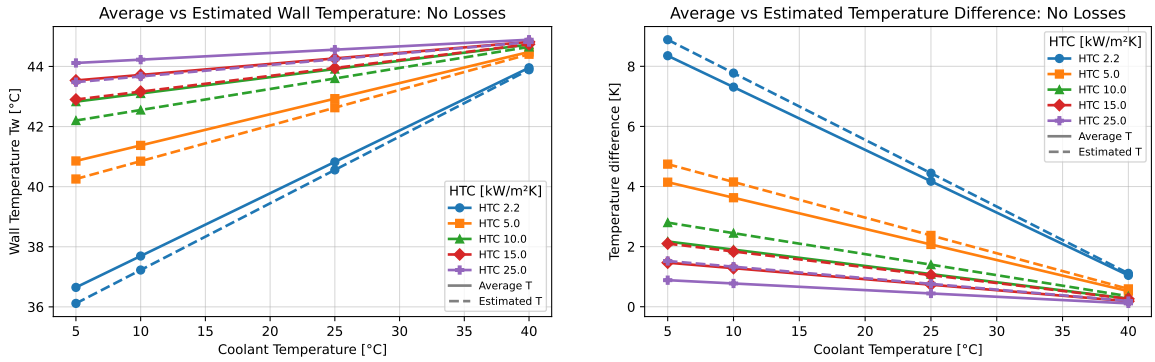

(a) Absolute temperature

(b) Difference with saturation temperature

Figure 5.14: Wall temperature estimation and relative to saturation temperature for model with no losses.

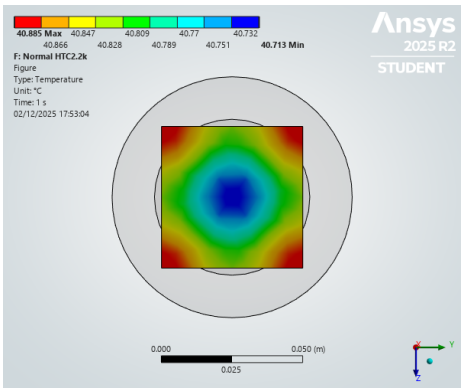

(a) Input: $HTC = 2.2\text{kW}/(\text{m}^2\,\text{K})$, $T_{coolant} = 25°\text{C}$;
Results: $T_{w,avg} = 40.82°\text{C}$, $T_{w,est} = 40.56°\text{C}$

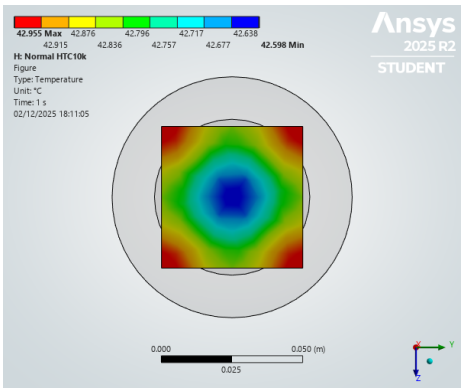

(b) Input: $HTC = 10.0\text{kW}/(\text{m}^2\,\text{K})$, $T_{coolant} = 5°\text{C}$;
Results: $T_{w,avg} = 42.83°\text{C}$, $T_{w,est} = 42.20°\text{C}$

Figure 5.15: Temperature profile of condensation surface resulting from computational model with no losses under different inputs.

This is also shown by Figure 5.15, as the condensation surface still shows a temperature gradient over the surface. Again, the wall temperature estimation is off by a few fractions of a degrees from the actual centre temperature. Specifically in the figures shown: $0.15\,\mathrm{K}$ and $0.40\,\mathrm{K}$ for the left and right figure, respectively.

To summarize, the HTC is, in both a model with losses taken into account and a model without losses, severely underestimated from the actual HTC used as an input. At lower HTCs the underestimation is smaller than at increased HTC. Moreover, the coolant temperature chosen also influences the severity of the underestimation.

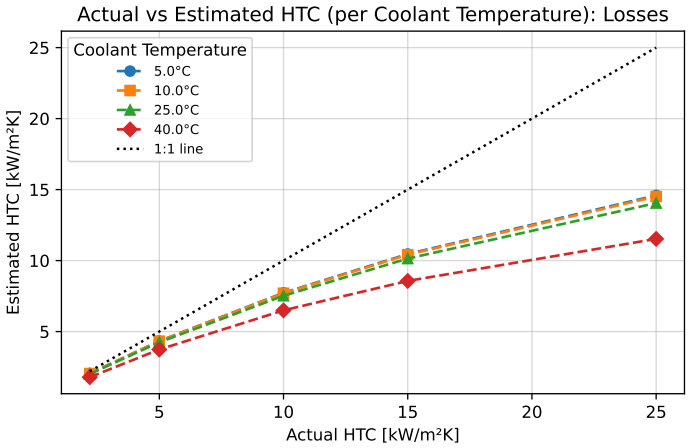

Figure 5.16: Relationship between the actual HTC model input to the estimated HTC, for every coolant temperature considered.

Figure 5.16 shows how the estimated HTC is related to the actual input HTC for the model with losses taken into account. The statements said before are clearly visible. For each distinct coolant temperature, the estimated HTC seem to be linear between the actual HTCs of $2.2\,\mathrm{kW/(m^2\,K)}$–$10.0\,\mathrm{kW/(m^2\,K)}$. This may allow for a translation from a estimated HTC to the actual HTC if the coolant temperature is known.

6 Discussion

The goal of this work is to design an experimental setup for estimating the HTC in DWC of a refrigerant. To achieve this, research is conducted into the relevant factors influencing DWC and its HTC, into the method of estimation, and into the verified of the design. Moreover, some experimental research was conducted into potential surface modifications to be used in the setup. All results are shown in the chapters before, here the interpretation and their meaning are discussed.

Setup design and verification

From literature, several significant factors influencing the formation of DWC and its HTC were found. These were translated into requirements for the experimental setup in design. Requirements relevant to findings in literature are: Uniform surface temperature to accurately estimate the HTC, control over the degree of subcooling, symmetric condensation surface, decreased presence of NCGs and regulation of saturation temperature & -pressure. Moreover, the design is required to allow for changing the condensation surface to experiment with different coatings.

Keeping these requirements in mind, three options arose to measure the heat transfer (coefficient) of a condensation process in a refrigerant. The first is based on the change in internal energy of the coolant fluid. The second is based on the enthalpy of phase change of the refrigerant. And the third is based on Fourier's law of conduction. The latter allows for the most control over design parameters, while keeping the temperature of the condensation surface (close to) constant. Therefore, this is the preferred design approach. This resulted in a novel test section design, allowing for changing the condensation surface to experiment with multiple coatings.

FWC is a baseline in determining the desired geometry of the test-section, as this is the lower limit in heat transfer taking place. Temperature measurements in the geometry are the foundation in determining the HTC, as these allow for determining the total heat transfer taking place. The measurement geometry was chosen to be a circular rod, its cross-section has a diameter of $35\,\mathrm{mm}$ and the distances between temperature measurement points is $60\,\mathrm{mm}$. The condensation surface has an area of $50\,\mathrm{mm} \times 50\,\mathrm{mm}$. Also, several pieces of equipment and sensors are chosen to design a process loop to facilitate the condensation of the refrigerant.

To confirm that the test-section functions accordingly, a computational model of the test-section is conducted. This allows for hypothetical centreline temperature measurements. Then, an estimation and uncertainty analysis is conducted to simulate an HTC estimation. The computational model takes into account a set HTC of convection, interfacial surface resistance, heat loss to the environment, and convective cooling to the coolant fluid.

The computational model proves that the test-section performs as designed at different heat transfer coefficients and chosen coolant temperatures. A measurable temperature difference occurs on the centreline of the geometry at the measurement points. However, the desired subcooling is not reached entirely. The goal was to set the condensation wall temperature $3\,\mathrm{K}$ below the saturation temperature

of the refrigerant (degree of subcooling). But, due to lower cooling capacity than expected, as shown by the temperature difference between the end of the rod and the coolant, the surface temperature lay closer to the saturation temperature than designed. This means that a lower coolant temperature is needed to increase the degree of subcooling; at high HTCs, specifically above $10\,\mathrm{kW/(m^2\,K)}$, the coolant reaching the lower limit of $5\,^{\circ}\mathrm{C}$ with water. While this issue arose for a saturation temperature of $45\,^{\circ}\mathrm{C}$, at lower temperature conditions this issue will occur at even lower HTCs.

Using (interpolated) centreline temperature at the measurements points, and simulated vapour pressure and temperature data, the HTC and its uncertainty were estimated. This showed that the HTC was underestimated for both a computational model with losses and without losses. The underestimation was more severe with higher initial HTCs used as input and higher coolant temperatures. This means that the losses are insignificant to the severe underestimation of the HTC. This can only be related to the underestimation of the condensation wall temperature. As the centreline temperature of the condensation surface is lower than the average, an overestimation is made in the temperature difference between the vapour and the wall temperature. This leads to an underestimation of the HTC, as it is inversely proportional to the temperature difference. The average temperature of the condensation surface is increased due to a temperature gradient towards the corners of the square condensation surface, the centre is the coolest, whereas the corners are the hottest. This makes the requirement of a homogeneous condensation surface in this design unachievable and results in an underestimation of the HTC. But, with the help of computational models the effect of in-homogeneous surface temperature can be further studied and possibly a correction function can be found to estimate the true HTC.

The uncertainty ($\sigma = 1$) grew substantially when applying increased coolant temperatures and HTC inputs. The rise in uncertainty can be explained by increased temperature measurements, as the error of these measurements are directly propositional to the measured temperature. In both the computational model with losses and without losses, the uncertainty is increased at higher coolant temperatures. This is caused by the small measurable temperature difference at the measurement points, possibly within the error of the sensors.

Initially, the working fluid chosen is R245fa. However, natural refrigerants are promising regarding fluorinated gasses legislation. Therefore, such substances, like R717, could be used in the future. However, possible safety precautions for each fluid should be examined and implemented beforehand.

Contact angles

Three potential test surfaces were received from `Nayang Technological University of Singapore`. One substrate consists of copper with oxide nanostructures, layered with coating. The other substrates are aluminium, one with oxide nanostructures only, the other with micro- & oxide nanostructures. To quantify the hydrophobicity, static and dynamic contact angle measurements were conducted with water. This concluded that the surfaces are hydrophobic, as the static contact angles are above 105° for all surfaces.

Regarding the dynamic contact angle measurements, no quantitative result was found. This is due to no observable constant contact angle measurement when receding or advancing. Multiple factors can contribute to this, for instance, the capillary length of water is $2.7\,\mathrm{mm}$, then gravitational forced become dominant over surface tension forces. If the (base) diameter of the droplet on the surface is higher than the capillary length, gravity squishes the droplet. Therefore, reducing the observable contact angle. As the base diameter of the droplets in all dynamic measurements are above the capillary length for water, the droplet is squished and thus the results are altered. Moreover, no hydrophobic needle was used, therefore the droplet could climb up the needle by surface tension forces. This also alters the results. In contrast to exceeding the capillary length, this would increase the contact angle. Also, surface irregularities can cause erratic movements of the droplet.

All of this could have resulted in no observable constant receding and advancing contact angle measurements. However, the overall trend of the contact angle during dynamic experiments lies in a small range, this shows that the hysteresis of water on these surfaces is low. Meaning the surface is not sticky and the droplet move quickly over the surface. This will enhance the achievability of DWC and increase the droplet departure rate and HTC.

Overall, the surfaces are hydrophobic with water. Therefore, nanostructures on the surface, coatings, and lubricant infusion prove to make hydrophilic surfaces hydrophobic. Due to the project timeline, unfortunately no measurements with R245fa were conducted, so no conclusions can be made regarding low surface tension fluids.

7

Recommendations

While the research questions can be answered in this work, the research itself is not finished. Therefore, recommendations are stated in this chapter for continuing this work and future research.

More research can be conducted into the behaviour of the test section at different saturation temperatures, HTCs and coolant temperatures. In this research only a saturation temperature of $45\,^{\circ}\mathrm{C}$ was used, other (lower) temperatures require different cooling capacities. Then, finding the family of functions to relate the estimated HTC to the actual HTC will introduce a correction for experimentally found estimations.

At a saturation temperature of $45\,^{\circ}\mathrm{C}$, it was shown that high HTCs require a low coolant temperature to facilitate adequate temperature measurement differences. At lower saturation temperatures the system will be limited to the freezing temperature of the coolant. This research assumed water as coolant, with a freezing limit of $5\,^{\circ}\mathrm{C}$. Future research or experiments may require other coolant solutions to lower this limit, for example coolant fluids like ethanol or water-glycerol mixture. Moreover, the HTC of coolant can differ from the value used in this research, if the amount of cooling is inadequate, actions should be taken to increase the heat transfer at the coolant side.

In addition, to accurately determine the total heat transfer and wall temperature, calibration of the thermal conductivity of the measurement section and swappable surface parts are needed. As the material properties may differ slightly from literature, the determined heat transfer and wall temperature can be inaccurate. As shown, errors in these parameters may cause severe under- or overestimation of the HTC, and should thus be prevented.

Moreover, the temperature gradient on the condensation surface needs more research. Here, it is assumed that a one dimensional estimation of the wall temperature can be used as an average. However, this work also shows that it is the lowest temperature of the surface, thereby decreasing the HTC estimation. Therefore, the temperature gradient must be researched to possibly find a correction to estimate the average wall temperature accurately. Also, the geometry of the swappable surface can be changed to prevent heat congestion in the corners of the condensation surface. For example by increasing the diameter of the rod.

Finally, the dynamic contact angle experiments with water can be repeated for droplets of decreased size. This, could result in an observable receding and advancing contact angle. Also, further research is needed into the contact angle of R245fa and possibly R717 (if safely) on the experimental surfaces. The results are an input in predictive modelling of the HTC in DWC. Therefore, this also allows for validation of these predictive models.

8

Conclusion

Condensation is a heat transfer process extensively used in a wide spread of applications, such as systems utilizing a refrigeration cycle. Here, working fluids (refrigerants) are currently responsible for approximately $7.8\,\%$ of global greenhouse gas emissions, of which $37\,\%$ are due to direct emissions of these substances into the environment. To reduce environmental impact, there is a global need for alternative refrigerants with a low global warming potential. Natural refrigerants are feasible, but can be toxic, flammable and/or require high pressure systems. By increasing the heat transfer coefficient of condensation processes in refrigeration cycles, the total refrigerant charge of the system can be decreased. Thereby decreasing the risks associated with natural refrigerants.

Dropwise condensation is shown to improve the heat transfer coefficient of condensation processes. In steam condensation, this is easily achieved, showing improvements up to seven fold. In refrigerants this is difficult to achieve, as droplets are hard to form due to low surface tension. Adding advantageous surface modifications, such as coatings and/or nanostructures, can improve the achievability of dropwise condensation by increasing the contact angle ($\geq 90°$). However, little experimental research is conducted into the heat transfer coefficient of dropwise condensation of refrigerants on different surfaces. Therefore, the purpose of this work is to find the optimal solution to experimentally estimate the heat transfer coefficient of a (dropwise) condensation process in a refrigerant. Subsequently, components to facilitate this are found, the setup is verified, literature research is conducted into the modelling of dropwise condensation, and the experimental contact angles are explored.

The optimal solution to estimate the heat transfer coefficient of a condensation process needs to comply with a set of requirements. For example, different condensation surfaces can be tested. Moreover, to accurately estimate the heat transfer coefficient, the condensation surface's temperature must be (close to) homogeneous. Also, the degree of subcooling has controllability. In addition, the condensation surface should be symmetric and be visually available, and the presence of non condensible gasses should be reduced. The setup is designed for a natural refrigerant, initial testing should be conducted with a conventional, safer, refrigerant.

At first, the refrigerant of choice is R245fa. This is a harmless option to validate the function of the setup, in the future a natural refrigerant (such as R717) can be used after taking necessary safety precautions. To estimate the heat transfer coefficient experimentally, the saturation temperature, condensation surface temperature, condensation surface area and total heat transfer are needed. To design the setup, filmwise condensation is used as a baseline for defining dimensions. Considering the setup requirements, it is concluded that Fourier's law of conduction is preferred for estimating the total heat transfer. This allows for flexibility regarding the condensation surface and keeps the condensation surface temperature homogeneous. The resulting design geometry consists of two rods. First a measurement section, at which the total heat transfer is estimated with temperature sensors according to Fourier's law of conduction. At the end of the rod, fins are placed for enhanced cooling by an auxiliary coolant loop. The second rod is a swappable surface, here the condensation process takes place, and the centreline temperature is measured to estimate the wall temperature. On the condensation side a pressure

chamber is installed, it has a view window to visually inspect the condensation surface.

To facilitate the condensation on the test-section, a pressurized loop is needed to produce saturated vapour. This consists of (following after the condensation chamber): a post-condenser to condensate the surplus of vapour. Next, a pump to generate liquid flow. Afterwards, an evaporator (and saturation tank) at which the liquid is turned into saturated vapour. Here, also a pressure sensor and temperature sensor are placed to control the heat input and to determine the saturation temperature. Also, a recirculation line between the outlet of the pump and the outlet of the condensation chamber is placed with a valve to control the amount of liquid being evaporated. At the coolant side, a thermal bath supplies cooled water to the test section and post-condenser.

A computational model verifies the function of the test-section design. At different heat transfer coefficients and coolant temperatures, a measurable temperature difference in the measurement section is shown. Moreover, a drop in temperature between the cooling surface and coolant is shown, meaning that the coolant temperature must be chosen accordingly to reach the desired degree of subcooling. This is especially required when the saturation temperature is low, and the heat transfer coefficient is high. From the computational model, hypothetical temperature measurements are extracted. These allow for a one dimensional estimation of the heat transfer coefficient. This proved that the heat transfer coefficient is severely underestimated due to overestimating the difference in saturation temperature and wall temperature. It also proved that the uncertainty of this result is too high when the temperature difference between saturated vapour and coolant is small. Therefore, it is paramount to lower the coolant temperature to reach sufficient temperature difference between measurement points.

While this work focusses mainly on the design of an experimental setup for estimating the heat transfer coefficient in dropwise condensation, predictive models exist. This requires several parameters of the fluid and condensation surface, such as the static and dynamic contact angles, and thermophysical properties. This quantizes the formation and interaction of droplets on the surface. Then, the heat transfer coefficient through a single droplet is statistically extrapolated over the whole surface to predict the overall average heat transfer coefficient.

In addition, three lubricant infused test surfaces were received from Nanyang Technological University of Singapore; one copper substrate with nanostructures, one aluminium substrate with nanostructures, and one aluminium substrate with both micro- and nanostructures. Using a sessile water droplet, it is concluded that all surfaces are hydrophobic. The static contact angles are $117.8°$, $119.4°$ & $109.1°$, respectively. Moreover, the hysteresis of the dynamic contact angles appears to be low. However, no quantitative result for the dynamic contact angles was found.

Bibliography

[1] Patricia B. Weisensee, Yunbo Wang, Hongliang Qian, Daniel Schultz, William P. King, and Nenad Miljkovic. Condensate droplet size distribution on lubricant-infused surfaces. *International Journal of Heat and Mass Transfer*, 109:187–199, June 2017. ISSN 0017-9310. doi: 10.1016/j.ijheatmasstransfer.2017.01.119.

[2] Bachir El Fil, Girish Kini, and Srinivas Garimella. A review of dropwise condensation: Theory, modeling, experiments, and applications. *International Journal of Heat and Mass Transfer*, 160:120172, October 2020. ISSN 00179310. doi: 10.1016/j.ijheatmasstransfer.2020.120172.

[3] José C. Jiménez-García, Alexis Ruiz, Alejandro Pacheco-Reyes, and Wilfrido Rivera. A Comprehensive Review of Organic Rankine Cycles. *Processes*, 11(7):1982, July 2023. ISSN 2227-9717. doi: 10.3390/pr11071982.

[4] Caesar Wu and Rajkumar Buyya. Chapter 7 - Data Center Cooling. In Caesar Wu and Rajkumar Buyya, editors, *Cloud Data Centers and Cost Modeling*, pages 249–284. Morgan Kaufmann, January 2015. ISBN 978-0-12-801413-4. doi: 10.1016/B978-0-12-801413-4.00007-6.

[5] Huijuan Chen, D. Yogi Goswami, and Elias K. Stefanakos. A review of thermodynamic cycles and working fluids for the conversion of low-grade heat. *Renewable and Sustainable Energy Reviews*, 14(9): 3059–3067, December 2010. ISSN 1364-0321. doi: 10.1016/j.rser.2010.07.006.

[6] Naeem Abas, Ali Raza Kalair, Nasrullah Khan, Aun Haider, Zahid Saleem, and Muhammad Shoaib Saleem. Natural and synthetic refrigerants, global warming: A review. *Renewable and Sustainable Energy Reviews*, 90:557–569, July 2018. ISSN 1364-0321. doi: 10.1016/j.rser.2018.03.099.

[7] James M. Calm. The next generation of refrigerants – Historical review, considerations, and outlook. *International Journal of Refrigeration*, 31(7):1123–1133, November 2008. ISSN 0140-7007. doi: 10.1016/j.ijrefrig.2008.01.013.

[8] U. N. Environment. About Montreal Protocol. https://www.unep.org/ozonaction/who-we-are/about-montreal-protocol, Mon, 10/29/2018 - 14:03.

[9] IIF-IIR, Morlet V, Coulomb D, and Dupont J. L. The impact of the refrigeration sector on climate change, 35th Informatory Note on refrigeration technologies. https://iifiir.org/en/fridoc/the-impact-of-the-refrigeration-sector-on-climate-change-141135, 2017.

[10] Zhao Yang, Biao Feng, Haiyun Ma, Lei Zhang, Chenjun Duan, Bing Liu, Yong Zhang, Siyi Chen, and Zongyu Yang. Analysis of lower GWP and flammable alternative refrigerants. *International Journal of Refrigeration*, 126:12–22, June 2021. ISSN 0140-7007. doi: 10.1016/j.ijrefrig.2021.01.022.

[11] EU F-Gas Regulation: The beginning of the end for climate-damaging fluorinated gases - ECOS. https://ecostandard.org/news_events/eu-f-gas-regulation-the-beginning-of-the-end-for-climate-damaging-fluorinated-gases/, October 2023.

[12] Regulation - EU - 2024/573 - EN - EUR-Lex. https://eur-lex.europa.eu/eli/reg/2024/573/oj/eng, February 2024.

[13] Mark O. McLinden, J. Steven Brown, Riccardo Brignoli, Andrei F. Kazakov, and Piotr A. Domanski. Limited options for low-global-warming-potential refrigerants. *Nat Commun*, 8(1):14476, February 2017. ISSN 2041-1723. doi: 10.1038/ncomms14476.

[14] Adrian Mota-Babiloni and Pavel Makhnatch. Predictions of European refrigerants place on the market following F-gas regulation restrictions. *International Journal of Refrigeration*, 127:101–110, July 2021. ISSN 0140-7007. doi: 10.1016/j.ijrefrig.2021.03.005.

[15] Mark O. McLinden, Andrei F. Kazakov, J. Steven Brown, and Piotr A. Domanski. A thermodynamic analysis of refrigerants: Possibilities and tradeoffs for Low-GWP refrigerants. *International Journal of Refrigeration*, 38:80–92, February 2014. ISSN 0140-7007. doi: 10.1016/j.ijrefrig.2013.09.032.

[16] Adrián Mota-Babiloni, Joaquín Navarro-Esbrí, Ángel Barragán-Cervera, Francisco Molés, and Bernardo Peris. Analysis based on EU Regulation No 517/2014 of new HFC/HFO mixtures as alternatives of high GWP refrigerants in refrigeration and HVAC systems. *International Journal of Refrigeration*, 52:21–31, April 2015. ISSN 0140-7007. doi: 10.1016/j.ijrefrig.2014.12.021.

[17] Ankitkumar Tejani, Harsh Gajjar, Vinay Toshniwal, and Rashi Kandelwal. The Impact of Low-GWP Refrigerants on Environmental Sustainability: An Examination of Recent Advances in Refrigeration Systems. *ESP IJACT*, Volume 2(Issue 2):62–77, 2022. ISSN 2583-2646.

[18] Anthony F. Mills and Carlos F. M. Coimbra. *Basic Heat and Mass Transfer*. Prentice Hall, San Diego, California, third edition edition, 2015. ISBN 978-0-9963053-0-3.

[19] Sameer Khandekar and Krishnamurthy Muralidhar. *Dropwise Condensation On Inclined Textured Surfaces*. Number 10305 in SpringerBriefs in Thermal Engineering and Applied Science. Springer, 2024. ISBN 978-1-4614-8446-2.

[20] J. W. Rose. Dropwise condensation theory and experiment: A review. *Proceedings of the Institution of Mechanical Engineers, Part A*, 216(2):115–128, January 2002. ISSN 0957-6509. doi: 10.1243/09576500260049034.

[21] E. Schmidt, W. Schurig, and W. Sellschopp. Versuche über die Kondensation von Wasserdampf in Film- und Tropfenform. *Technische Mechanik und Thermodynamik*, 1(2):53–63, February 1930. ISSN 1434-0860. doi: 10.1007/BF02641051.

[22] Sunwoo Kim and Kwang J. Kim. Dropwise Condensation Modeling Suitable for Superhydrophobic Surfaces. *Journal of Heat Transfer*, 133(081502), May 2011. ISSN 0022-1481. doi: 10.1115/1.4003742.

[23] J. W. Rose. Dropwise condensation theory. *International Journal of Heat and Mass Transfer*, 24(2):191–194, February 1981. ISSN 0017-9310. doi: 10.1016/0017-9310(81)90026-0.

[24] James L McCormick and Eric Baer. On the mechanism of heat transfer in dropwise condensation. *Journal of Colloid Science*, 18(3):208–216, March 1963. ISSN 0095-8522. doi: 10.1016/0095-8522(63)90012-6.

[25] Mousa Abu-Orabi. Modeling of heat transfer in dropwise condensation. *International Journal of Heat and Mass Transfer*, 41(1):81–87, January 1998. ISSN 00179310. doi: 10.1016/S0017-9310(97)00094-X.

[26] E. J. Le Fevre and John W. Rose. A THEORY OF HEAT TRANSFER BY DROPWISE CONDENSATION. In *International Heat Transfer Conference 3*, pages 362–375. Begel House Inc., 1966. doi: 10.1615/IHTC3.180.

[27] A. Umur and P. Griffith. Mechanism of Dropwise Condensation. *Journal of Heat Transfer*, 87(2):275–282, May 1965. ISSN 0022-1481. doi: 10.1115/1.3689090.

[28] Gary A. O'neill and J. W. Westwater. Dropwise condensation of steam on electroplated silver surfaces. *International Journal of Heat and Mass Transfer*, 27(9):1539–1549, September 1984. ISSN 0017-9310. doi: 10.1016/0017-9310(84)90266-7.

[29] Song Yongji, Xu Dunqi, Lin Jifang, and Tsian Siexong. A study on the mechanism of dropwise condensation. *International Journal of Heat and Mass Transfer*, 34(11):2827–2831, November 1991. ISSN 0017-9310. doi: 10.1016/0017-9310(91)90243-8.

[30] Shoukat Alim Khan, Furqan Tahir, Ahmer Ali Bozdar Baloch, and Muammer Koc. Review of Micro–Nanoscale Surface Coatings Application for Sustaining Dropwise Condensation. *Coatings*, 9(2):117, February 2019. ISSN 2079-6412. doi: 10.3390/coatings9020117.

[31] Frank P. Incropera, David P. DeWitt, Theodore L. Bergman, and Adrienne S. Lavine, editors. *Fundamentals of Heat and Mass Transfer*. Wiley, Hoboken, NJ, 6. ed edition, 2007. ISBN 978-0-471-45728-2.

[32] Stefano Bortolin, Marco Tancon, and Davide Del Col. Heat Transfer Enhancement During Dropwise Condensation Over Wettability-Controlled Surfaces. In Marco Marengo and Joel De Coninck, editors, *The Surface Wettability Effect on Phase Change*, pages 29–67. Springer International Publishing, Cham, 2022. ISBN 978-3-030-82991-9 978-3-030-82992-6. doi: 10.1007/978-3-030-82992-6_3.

[33] Xuechao Hu, Qiujie Yi, Xiangqiang Kong, and Jianwei Wang. A Review of Research on Dropwise Condensation Heat Transfer. *Applied Sciences*, 11(4):1553, February 2021. ISSN 2076-3417. doi: 10.3390/app11041553.

[34] J. L. McCormick and J. W. Westwater. Nucleation sites for dropwise condensation. *Chemical Engineering Science*, 20(12):1021–1036, December 1965. ISSN 0009-2509. doi: 10.1016/0009-2509(65)80104-X.

[35] A. W. Neumann, A. H. Abdelmessih, and A. Hameed. The role of contact angles and contact angle hysteresis in dropwise condensation heat transfer. *International Journal of Heat and Mass Transfer*, 21(7):947–953, July 1978. ISSN 0017-9310. doi: 10.1016/0017-9310(78)90186-2.

[36] Robert N. Wenzel. RESISTANCE OF SOLID SURFACES TO WETTING BY WATER. *Ind. Eng. Chem.*, 28(8):988–994, August 1936. ISSN 0019-7866. doi: 10.1021/ie50320a024.

[37] A. B. D. Cassie and S. Baxter. Wettability of porous surfaces. *Trans. Faraday Soc.*, 40(0):546–551, January 1944. ISSN 0014-7672. doi: 10.1039/TF9444000546.

[38] Shreyas Chavan, Hyeongyun Cha, Daniel Orejon, Kashif Nawaz, Nitish Singla, Yip Fun Yeung, Deokgeun Park, Dong Hoon Kang, Yujin Chang, Yasuyuki Takata, and Nenad Miljkovic. Heat Transfer through a Condensate Droplet on Hydrophobic and Nanostructured Superhydrophobic Surfaces. *Langmuir*, 32(31):7774–7787, August 2016. ISSN 0743-7463. doi: 10.1021/acs.langmuir.6b01903.

[39] Clark Graham and Peter Griffith. Drop size distributions and heat transfer in dropwise condensation. *International Journal of Heat and Mass Transfer*, 16(2):337–346, February 1973. ISSN 0017-9310. doi: 10.1016/0017-9310(73)90062-8.

[40] Hai Wu Wen and Ru Maa Jer. On the heat transfer in dropwise condensation. *The Chemical Engineering Journal*, 12(3):225–231, January 1976. ISSN 0300-9467. doi: 10.1016/0300-9467(76)87016-5.

[41] E. J. Le Fevre and J. W. Rose. An experimental study of heat transfer by dropwise condensation. *International Journal of Heat and Mass Transfer*, 8(8):1117–1133, August 1965. ISSN 0017-9310. doi: 10.1016/0017-9310(65)90139-0.

[42] Bong June Zhang, Cheng Kuok, Kwang Jin Kim, Taeseon Hwang, and Hyungkee Yoon. Dropwise steam condensation on various hydrophobic surfaces: Polyphenylene sulfide (PPS), polytetrafluoroethylene (PTFE), and self-assembled micro/nano silver (SAMS). *International Journal of Heat and Mass Transfer*, 89:353–358, October 2015. ISSN 0017-9310. doi: 10.1016/j.ijheatmasstransfer.2015.05.060.

[43] Riccardo Parin, Marco Tancon, Matteo Mirafiori, Stefano Bortolin, Lorenzo Moro, Leonardo Zago, Francesco Carraro, Alessandro Martucci, and Davide Del Col. Heat transfer and droplet population during dropwise condensation on durable coatings. *Applied Thermal Engineering*, 179:115718, October 2020. ISSN 1359-4311. doi: 10.1016/j.applthermaleng.2020.115718.

[44] J. Jagielski, A. Piatkowska, P. Aubert, L. Thomé, A. Turos, and A. Abdul Kader. Ion implantation for surface modification of biomaterials. *Surface and Coatings Technology*, 200(22):6355–6361, June 2006. ISSN 0257-8972. doi: 10.1016/j.surfcoat.2005.11.005.

[45] Robert Erb and Edmund Thelen. PROMOTING PERMANENT DROPWISE CONDENSATION. *Ind. Eng. Chem.*, 57(10):49–52, October 1965. ISSN 0019-7866, 1541-5724. doi: 10.1021/ie50670a009.

[46] Sachin Sharma Ashok Kumar, Shahid Bashir, K. Ramesh, and S. Ramesh. A comprehensive review: Super hydrophobic graphene nanocomposite coatings for underwater and wet applications to enhance corrosion resistance. *FlatChem*, 31:100326, January 2022. ISSN 2452-2627. doi: 10.1016/j.flatc.2021.100326.

[47] Wenyan Geng, Anmin Hu, and Ming Li. Super-hydrophilicity to super-hydrophobicity transition of a surface with Ni micro–nano cones array. *Applied Surface Science*, 263:821–824, December 2012. ISSN 0169-4332. doi: 10.1016/j.apsusc.2012.09.006.

[48] Nenad Miljkovic, Ryan Enright, Youngsuk Nam, Ken Lopez, Nicholas Dou, Jean Sack, and Evelyn N. Wang. Jumping-Droplet-Enhanced Condensation on Scalable Superhydrophobic Nanostructured Surfaces. *Nano Lett.*, 13(1):179–187, January 2013. ISSN 1530-6984. doi: 10.1021/nl303835d.

[49] Youngsuk Nam and Y. Sungtaek Ju. A comparative study of the morphology and wetting characteristics of micro/nanostructured Cu surfaces for phase change heat transfer applications. *Journal of Adhesion Science and Technology*, 27(20):2163–2176, October 2013. ISSN 0169-4243. doi: 10.1080/01694243.2012.697783.

[50] B. H. Luo, P. W. Shum, Z. F. Zhou, and K. Y. Li. Preparation of hydrophobic surface on steel by patterning using laser ablation process. *Surface and Coatings Technology*, 204(8):1180–1185, January 2010. ISSN 0257-8972. doi: 10.1016/j.surfcoat.2009.10.043.

[51] Gun-Tae Kim, Su-Ji Gim, Seung-Min Cho, Nikhil Koratkar, and Il-Kwon Oh. Wetting-Transparent Graphene Films for Hydrophobic Water-Harvesting Surfaces. *Advanced Materials*, 26 (30):5166–5172, 2014. ISSN 1521-4095. doi: 10.1002/adma.201401149.

[52] Daniel J. Preston, Daniela L. Mafra, Nenad Miljkovic, Jing Kong, and Evelyn N. Wang. Scalable Graphene Coatings for Enhanced Condensation Heat Transfer. *Nano Lett.*, 15(5):2902–2909, May 2015. ISSN 1530-6984. doi: 10.1021/nl504628s.

[53] Marco Tancon, Matteo Mirafiori, Stefano Bortolin, Maria Basso, Elena Colusso, and Davide Del Col. Dropwise condensation mechanisms when varying vapor velocity. *Applied Thermal Engineering*, 216: 119021, November 2022. ISSN 1359-4311. doi: 10.1016/j.applthermaleng.2022.119021.

[54] Xi Chen and Melanie M. Derby. Droplet departure modeling and a heat transfer correlation for dropwise flow condensation in hydrophobic mini-channels. *International Journal of Heat and Mass Transfer*, 125:1096–1104, October 2018. ISSN 0017-9310. doi: 10.1016/j.ijheatmasstransfer.2018.04.140.

[55] Xue-Hu Ma, Xing-Dong Zhou, Zhong Lan, Yi-Ming Li, and Yu Zhang. Condensation heat transfer enhancement in the presence of non-condensable gas using the interfacial effect of dropwise condensation. *International Journal of Heat and Mass Transfer*, 51(7):1728–1737, April 2008. ISSN 0017-9310. doi: 10.1016/j.ijheatmasstransfer.2007.07.021.

[56] Surface Tension. https://www.engineeringtoolbox.com/surface-tension-d_962.html, 2005.

[57] Chieko Kondou, Ryuichi Nagata, Noriko Nii, Shigeru Koyama, and Yukihiro Higashi. Surface tension of low GWP refrigerants R1243zf, R1234ze(Z), and R1233zd(E). *International Journal of Refrigeration*, 53:80–89, May 2015. ISSN 0140-7007. doi: 10.1016/j.ijrefrig.2015.01.005.

[58] Yee Jack Lai, Pei Ching Oh, Thiam Leng Chew, and Abdul Latif Ahmad. Surface Repellency beyond Hydrophobicity: A Review on the Latest Innovations in Superomniphobic Surfaces. *ACS Omega*, 10(6):5172–5192, February 2025. doi: 10.1021/acsomega.4c08269.

[59] Johannes Köhler Mendizábal, Bakhshish Preet Singh, Kazi Fazle Rabbi, Nithin Vinod Upot, Kashif Nawaz, Anthony Jacobi, and Nenad Miljkovic. Enhanced internal condensation of R1233zd(E) on micro- and nanostructured copper and aluminum surfaces. *International Journal of Heat and Mass Transfer*, 207:124012, June 2023. ISSN 0017-9310. doi: 10.1016/j.ijheatmasstransfer.2023.124012.

[60] Konrad Rykaczewski, Adam T. Paxson, Matthew Staymates, Marlon L. Walker, Xiaoda Sun, Sushant Anand, Siddarth Srinivasan, Gareth H. McKinley, Jeff Chinn, John Henry J. Scott, and Kripa K. Varanasi. Dropwise Condensation of Low Surface Tension Fluids on Omniphobic Surfaces. *Sci Rep*, 4(1):4158, March 2014. ISSN 2045-2322. doi: 10.1038/srep04158.

[61] Soumyadip Sett, Peter Sokalski, Kalyan Boyina, Longnan Li, Kazi Fazle Rabbi, Harpreet Auby, Thomas Foulkes, Allison Mahvi, George Barac, Leslie W. Bolton, and Nenad Miljkovic. Stable Dropwise Condensation of Ethanol and Hexane on Rationally Designed Ultrascalable Nanostructured Lubricant-Infused Surfaces. *Nano Lett.*, 19(8):5287–5296, August 2019. ISSN 1530-6984. doi: 10.1021/acs.nanolett.9b01754.

[62] Kazi Fazle Rabbi, Siavash Khodakarami, Jin Yao Ho, Muhammad Jahidul Hoque, and Nenad Miljkovic. Dynamic omniphobic surfaces enable the stable dropwise condensation of completely wetting refrigerants. *Nat Commun*, 16(1):1105, January 2025. ISSN 2041-1723. doi: 10.1038/s41467-025-56338-3.

[63] Deepak Monga, Pavan Sai Dosawada, Dylan Boylan, Kuwin Wyke, Pengtao Wang, and Xianming Dai. Designing slippery rough surfaces to enhance dropwise condensation of low surface tension fluid. *International Journal of Heat and Mass Transfer*, 247:127105, September 2025. ISSN 0017-9310. doi: 10.1016/j.ijheatmasstransfer.2025.127105.

[64] Karim Khalil, Dan Soto, Taylor Farnham, Adam Paxson, Asli Ugur Katmis, Karen Gleason, and Kripa K. Varanasi. Grafted Nanofilms Promote Dropwise Condensation of Low-Surface-Tension Fluids for High-Performance Heat Exchangers. *Joule*, 3(5):1377–1388, May 2019. ISSN 2542-4785, 2542-4351. doi: 10.1016/j.joule.2019.04.009.

[65] Ian H. Bell, Jorrit Wronski, Sylvain Quoilin, and Vincent Lemort. Pure and pseudo-pure fluid thermophysical property evaluation and the open-source thermophysical property library coolprop. *Industrial & Engineering Chemistry Research*, 53(6):2498–2508, 2014. doi: 10.1021/ie4033999. URL `http://pubs.acs.org/doi/abs/10.1021/ie4033999`.

[66] Betrouwbare emissiefactoren voor bedrijven en consumenten in nederland, 2025. URL `https://co2emissiefactoren.nl/`. Accessed: 20 october 2025.

[67] J. Y. Ho, K. F. Rabbi, S. Sett, T. N. Wong, and N. Miljkovic. Dropwise condensation of low surface tension fluids on lubricant-infused surfaces: Droplet size distribution and heat transfer. *International Journal of Heat and Mass Transfer*, 172:121149, June 2021. ISSN 0017-9310. doi: 10.1016/j.ijheatmasstransfer.2021.121149.

[68] Huanyu Zhao, Hanyang Ye, Kazi Fazle Rabbi, Xinrui Wang, Nenad Miljkovic, and Jin Yao Ho. Micro- and Nanoengineered Metal Additively Manufactured Surfaces for Enhanced Anti-Frosting Applications. *ACS Appl. Mater. Interfaces*, 16(27):35697–35715, July 2024. ISSN 1944-8244. doi: 10.1021/acsami.4c02765.

[69] Leymus Yong Xiang Lum, Pengfei Liu, and Jin Yao Ho. Micro/nanostructuring of metal additively manufactured aluminum alloy for enhanced pool boiling of dielectric fluids. *International Journal of Heat and Mass Transfer*, 221:125090, April 2024. ISSN 0017-9310. doi: 10.1016/j.ijheatmasstransfer.2023.125090.

[70] Leymus Yong Xiang Lum, Pengfei Liu, Hanyang Ye, and Jin Yao Ho. Revealing Microstructured Surface Critical Heat Flux Degradation Mechanisms and Synergistic Pool Boiling Enhancement in Fluorinated Fluids. *ACS Appl. Mater. Interfaces*, 17(18):27331–27350, May 2025. ISSN 1944-8244. doi: 10.1021/acsami.4c22543.

[71] Engineers Edge and Engineers Edge LLC. Convective Heat Transfer Coefficients Table Chart. https://www.engineersedge.com/heat_transfer/convective_heat_transfer_coefficients__13378.htm.

[72] Convection. https://www.dspe.nl/knowledge/thermomechanics/chapter-1-basics/1-2-heat-transfer/convection/.

[73] Mineral Wool Insulation. https://www.engineeringtoolbox.com/mineral-wool-insulation-k-values-d_815.html.

[74] Evaluation of measurement data — Guide to the expression of uncertainty in measurement, 2008.

A

Test section calculations

Refrigerants properties visualisation.

The properties of water, R245fa & R717 are relevant to the project. All properties have been extracted from `CoolProp` [65].

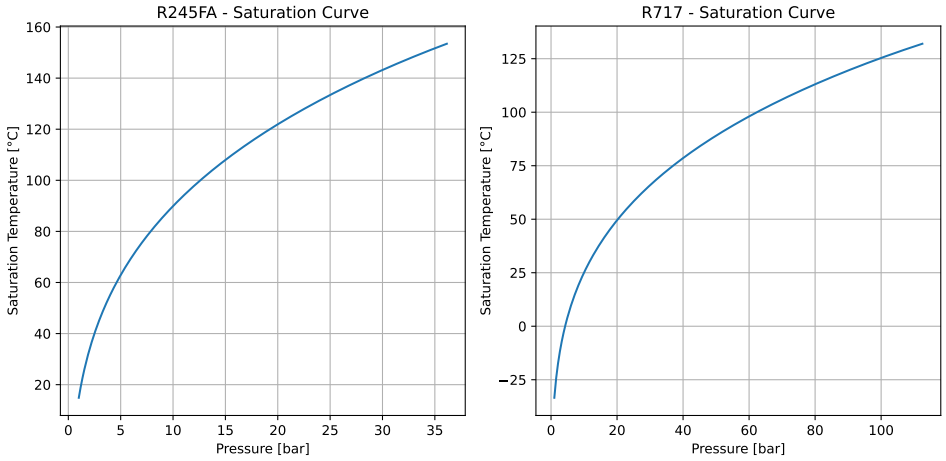

Figure A.1: Saturation curve of R245fa and R717 [65].

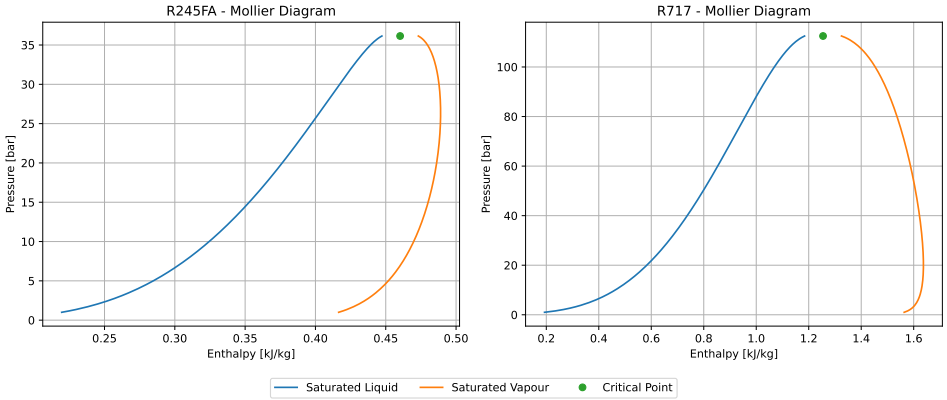

Figure A.2: Mollier diagram of R245fa and R717 [65].

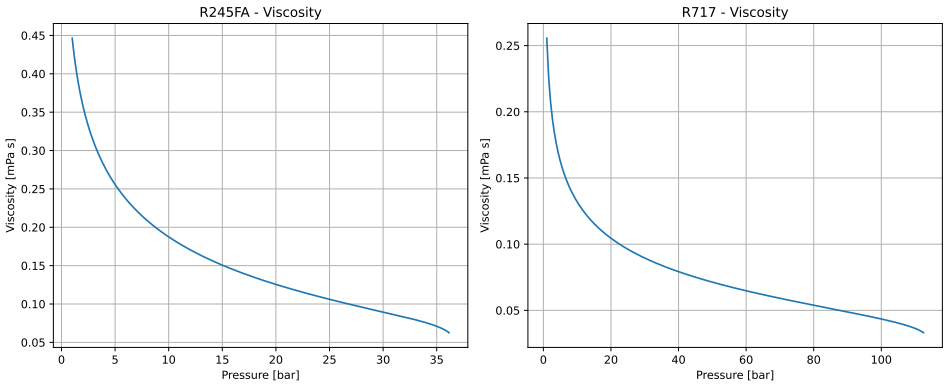

Figure A.3: Viscosity of R245fa and R717 [65].

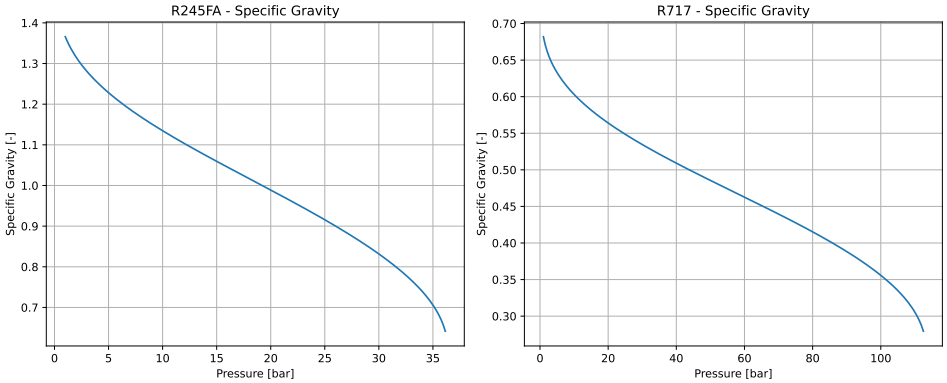

Figure A.4: Specific gravity of R245fa and R717 [65].

Modelling the heat transfer coefficient in Filmwise condensation

To model the average HTC in FWC, the method proposed by Mills and Coimbra [18] is followed. Its steps and equations are described in short below.

In the laminar regime ($Re_{film} < 30$), the equation for the average HTC for a vertical plate is quite straightforward:

$$\bar{h} = 0.943 \left[\frac{h_{\mathrm{fg}} g \left(\rho_l - \rho_v\right) k_l^3}{L \left(T_{\mathrm{sat}} - T_w\right) \nu_l} \right]^{1/4} \tag{A.1}$$

Due to applying this method to a refrigerant with low enthalpy of phase change, a modified latent heat is needed (h'_{fg}) instead of h_{fg}:

$$h'_{fg} = h_{fg} + \frac{3}{8} c_{p,l} \left(T_{sat} - T_w\right) \tag{A.2}$$

The total heat transfer can then be determined by:

$$\dot{Q} = \bar{h} A \Delta T \tag{A.3}$$

However, the amount of condensation may cause the condensate to behave wavy laminar or turbulent. Therefore it is essential to determine the regime. Here, first the amount of condensate is determined ($\dot{m}$):

$$\dot{Q} = \dot{m} h_{fg} \tag{A.4}$$

Once found, the mass flow rate per unit width (L [m]) of the film (Γ [kg/(s m)]):

$$\Gamma = \dot{m}/L \tag{A.5}$$

This can determine the reynolds number (Re_{film} [-]) at the bottom of the plate. If $Re < 30$ the regime is laminar, if $30 < Re_\delta < Re_{turb}$ the regime is wavy laminar, if $Re_{turb} < Re_{film}$ the regime is turbulent. Here Re_{turb} is the reynolds number when transitioning to the turbulent regime. Depending on the resulting reynold number, the turbulent regime is probably not needed.

$$Re_{film} = \frac{4\Gamma}{\mu_l} \tag{A.6}$$

If $30 < Re_{film}$, the nusselt number (Nu) correlation can be used to determine the average HTC:

$$\bar{Nu} = \frac{\bar{h}\left(\nu_l^2/g\right)^{1/3}}{k_l} \tag{A.7}$$

Here, ν_l is the kinematic viscosity of the fluid (μ_l/ρ_l). The nusselt number is correlated by the Prandtl number (Pr) and Jacob number (Ja).

$$\bar{Nu} = \left[\frac{Pr_l}{4\,Ja_l}\frac{\left(\nu_l^2/g\right)^{1/3}}{L}\right]^{0.18} \tag{A.8}$$

The Prandtl number is determined as:

$$Pr_l = \frac{c_{p,l}\mu_l}{k_l} \tag{A.9}$$

And the Jacob number is determined as:

$$Ja_l = \frac{c_{p,l}\left(T_{sat} - T_w\right)}{h_{fg}} \tag{A.10}$$

The results are shown in Figures A.5 to A.7. As shown, the reynolds number does not exceed 100 for the desired degree of subcooling. Therefore, it is expected that the flow regime will not reach turbulence, but maintain laminar or wavy flow patterns.

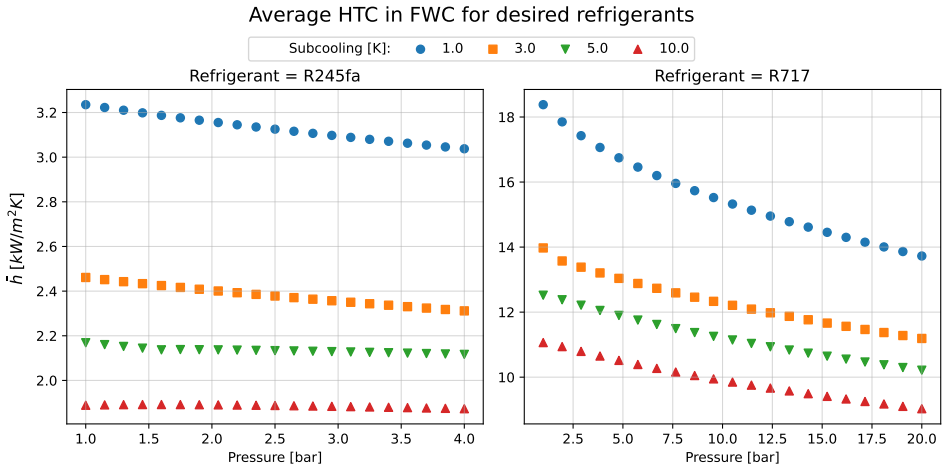

Figure A.5: HTC of FWC at different pressures for R245fa and R717 side by side

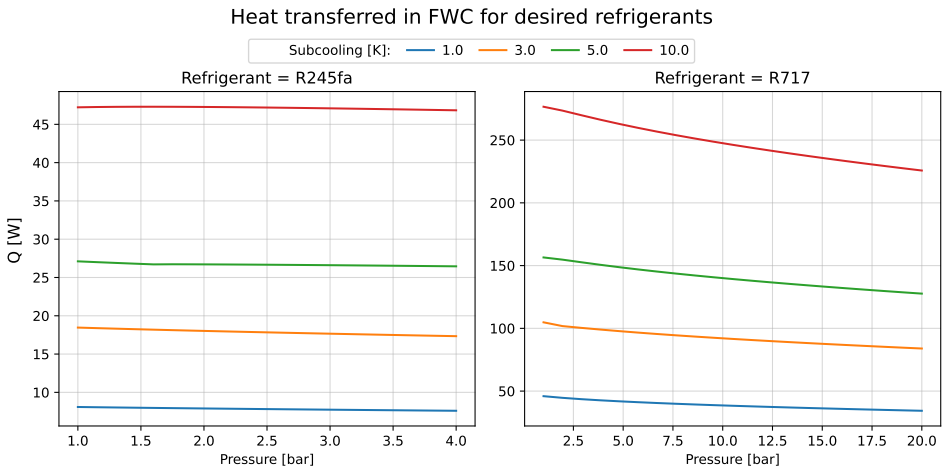

Figure A.6: Total heat transfer of FWC at different pressures for R245fa and R717 side by side

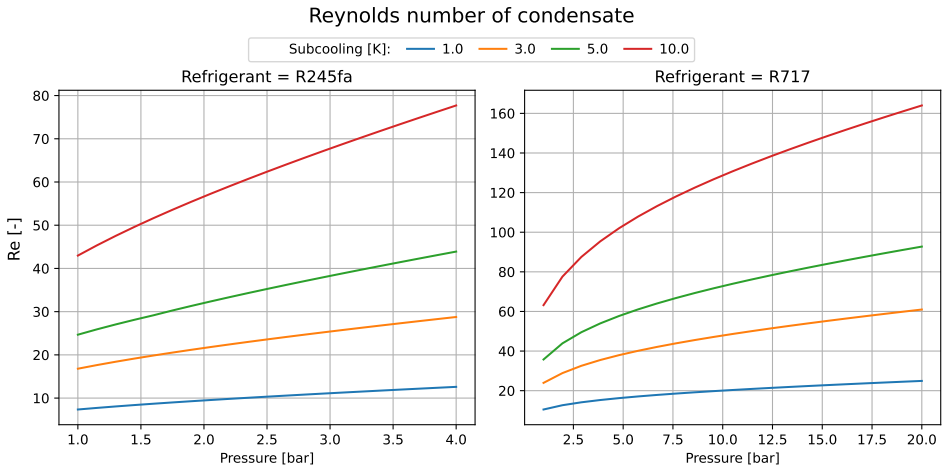

Figure A.7: Reynolds of FWC at different pressures for R245fa and R717 side by side

Temperature difference modelling to find desired measuring geometry

The lowest expected heat transfer should be measurable. That is when FWC occurs in R245fa (Chapter A). The total heat transfer is calculated as such:

$$\dot{Q} = hA\Delta T \tag{A.11}$$

Here the area is set to $50 \times 50\text{mm}^2$, and the average HTC to $2.2\text{kW}/(\text{m}^2\,\text{K})$. And a degree of subcooling in R245fa of 5K.

Then, the temperature difference is determined for different cross-sections (A depending on diameter) and measurements lengths (L).

$$\Delta T = \frac{\dot{Q}L}{kA} \tag{A.12}$$

The resulting temperature difference for these variable geometries are shown in Figure A.8.

Dimensionalized geometry of test section components (scaled)

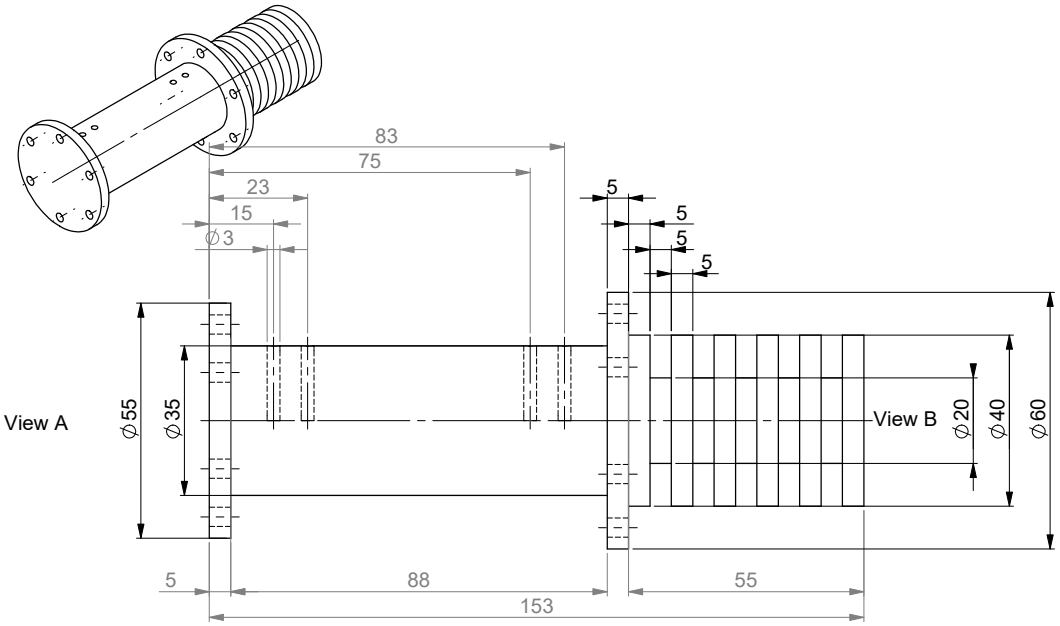

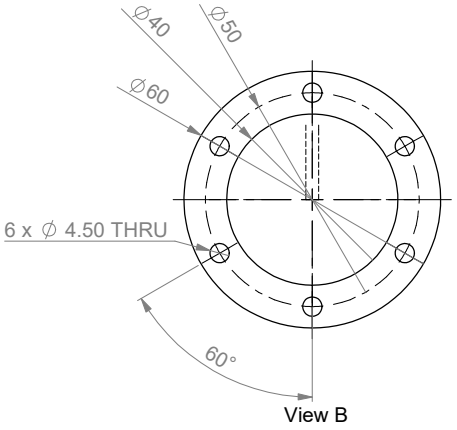

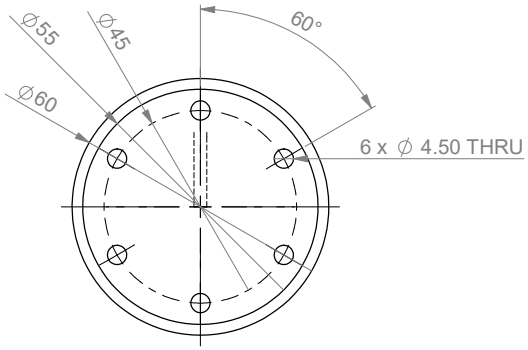

View A

	units mm	scale 1:1	quantity 1	date 08/12/2025	remark ISO-2768 standard Part 1/2
material			Copper	mass	gr
author	Ruben Caan			group ME-P&E	

name: **Construction drawings copper testsection**

TU Delft Delft University of Technology

format: A3

drawing no.: 1/2

Dimensionalized geometry of test section components (scaled)

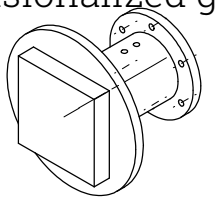

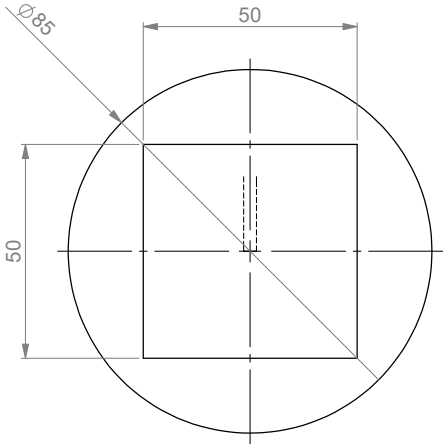

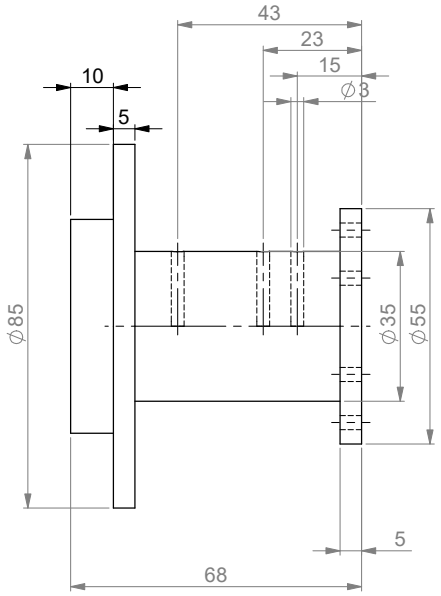

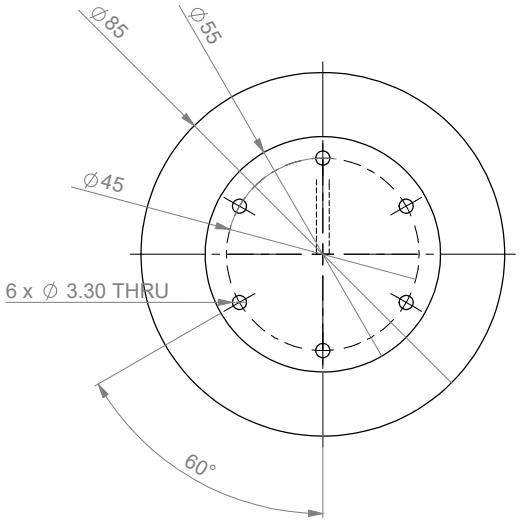

	units mm	scale 1:1	quantity 1	date 08/12/2025	remark ISO-2768 standard Part 2/2
material			Copper	mass	gr
author	Ruben Caan r.j.caan@student.tudelft.nl			group ME-P&E	
name	Construction drawings copper testsection				
TU Delft Delft University of Technology				format A3	drawing no. 2/2

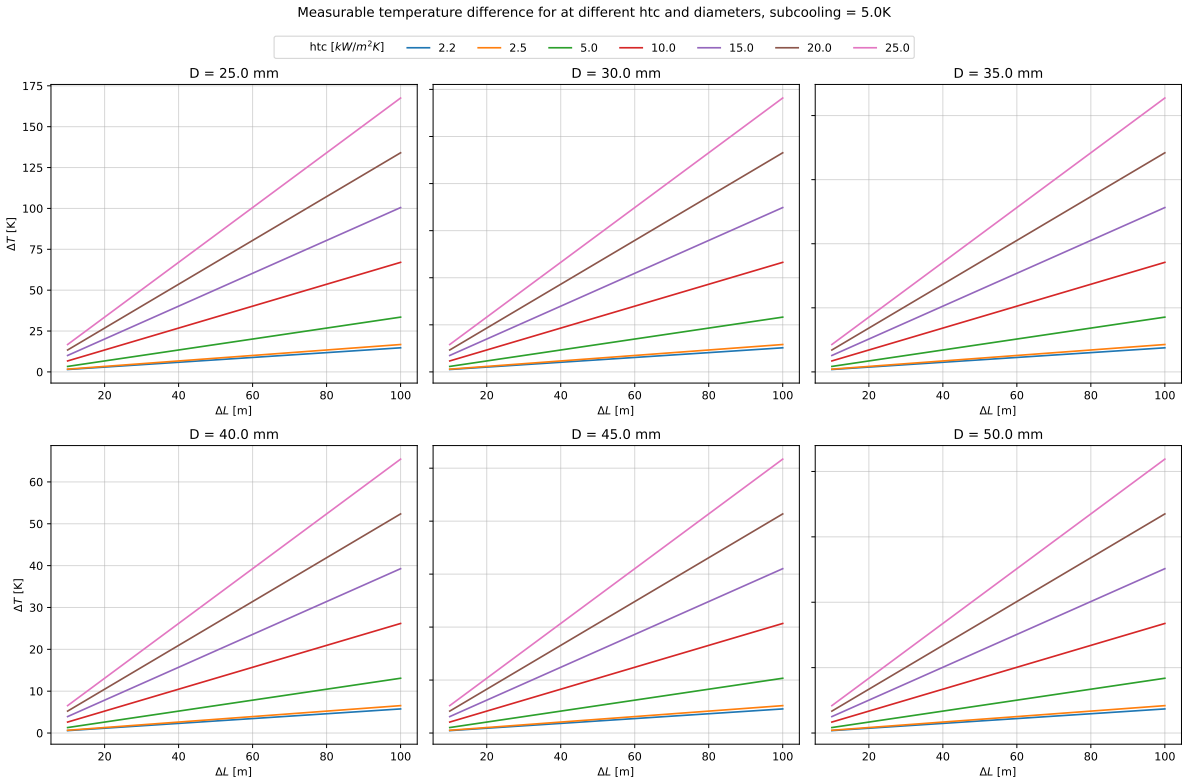

Figure A.8: Expected measurable temperature difference at different diameters and lengths between measurement points.

P&ID components

Table A.1: Instrumentation of conceptual P&ID (Figure 3.10)

Ref	Type	Description/purpose	Rating	Accuracy
TS01	Temperature sensor	Temperature measurement in the swappable condensation surface section, to backtrack the condensation surface temperature.	$-25-250°C$	$\pm(0.3+0.005\|T\|)°C$
TS02	Temperature sensor	Backup temperature measurement of *TS01*.	$-25-250°C$	$\pm(0.3+0.005T\|)°C$
TS03	Temperature sensor	First temperature measurement to determine the heat transfer in the measurement section.	$-25-250°C$	$\pm(0.3+0.005\|T\|)°C$
TS04	Temperature sensor	Backup temperature measurement of *TS03*.	$-25-250°C$	$\pm(0.3+0.005\|T\|)°C$
TS05	Temperature sensor	Second temperature measurement to determine the heat transfer in the measurement section.	$-25-250°C$	$\pm(0.3+0.005\|T\|)°C$

Ref	Type	Description/purpose	Rating	Accuracy
TS06	Temperature sensor	Backup temperature measurement of *TS05*.	$-25 - 250°C$	$\pm(0.3+0.005\|T\|)°C$
TS07	Temperature sensor	Measuring the saturation temperature of the vapour. As a validation and backup to *PS01*.	$-5 - 250°C$	$\pm(0.03 + 0.0002\|T\|)°C$
TS08	Temperature sensor	Temperature measurement of the post condensed liquid before entering the evaporator.	$-5 - 250°C$	$\pm(0.03 + 0.0002\|T\|)°C$
TS09	Temperature sensor	Safety temperature measurement to prevent the *EH* from overheating.	$-35 - 350°C$	$\pm 2.2\|T\|°C$
TS10	Temperature sensor	Temperature measurement of the coolant before entering the cooling chamber of the test section.	$-25 - 250°C$	$\pm(0.3+0.005\|T\|)°C$
PI01	Pressure indicator	Visual pressure indicator after evaporation, this way the operator can see if the system is pressurised.	$0 - 20\text{bar}$	2.5% of max
PI02	Pressure indicator	Visual pressure indicator of the condensation chamber, this way the operator can make sure the condensation chamber is depressurised when changing the condensation surface.	$0 - 20\text{bar}$ (rel.)	2.5% of max
PS01	Pressure sensor	Pressure reading of the pressure after evaporation, for data logging and to control the *EH*.	$0 - 5\text{bar}$ (abs.)	$\pm 0.3\%$ of max
ES01	Power sensor	Measuring the power input into the *EH* over time.	N/A	N/A
PP	Magnetically coupled gear pump	Positive displacement sealed gear pump, for moving the liquid refrigerant around the loop.	$0.38\text{mL}/rev$	N/A
NV	Needle valve	By altering the opening the flow towards the evaporator/saturation tank can be controlled.	N/A	N/A
LS01	Level sensor	Safety switch to prevent the pump from running dry.	N/A	N/A
CV	Check valve	One way valve to prevent the tank from emptying towards the rest of the system.	N/A	N/A

Ref	Type	Description/purpose	Rating	Accuracy
EH	Electrical heater	Means of supplying energy for evaporation. Its energy input also controls the pressure.	375 W	N/A
TK	Saturation tank	Tank with liquid refrigerant at saturation pressure, ensures only saturated vapour leaves the evaporator. Here also a sight glass is present to help with charging the system, and to give the operator indication about the evaporation rate.	N/A	N/A
RV	Relief valve	Relief to ventilation ducts to prevent a pressure build up in the system.	N/A	N/A
HV01	Hand valve	Allows for isolation of the condensation chamber to swap the condensation surface.	N/A	N/A
HV02	Hand valve	Same function as *HV01*	N/A	N/A
HV03	Hand valve	Normally closed valve, but needed to attach a vacuum pump to the condensation chamber. This way the presence of NCG's is kept to a minimum when changing condensation surfaces.	N/A	N/A
HV04	Hand valve	Allows for control over the flow rate of coolant.	N/A	N/A
HV05	Hand valve	Three way valve to allow for pulling a vacuum of the system and charging it.	N/A	N/A
PCD	Post condenser	Plate heat exchanger to condense the left over vapour from the condensation chamber.	N/A	N/A
TB	Thermal bath	Source of coolant, with integrated cooling and heating at the desired temperature. Includes a pump.	N/A	N/A
CF	Charge fitting	Mechanical fitting for coupling to a charging tank of refrigerant.	N/A	N/A
VF01	Vacuum fitting	Mechanical fitting for coupling to a vacuum pump. A vacuum pump reduces the presence of NCG's	N/A	N/A
VF02	Vacuum fitting	Same purpose as *VF02*, but for the condensation chamber.	N/A	N/A

Setup heat flow dynamics

To simulate the heat transfer in the test section and the state of the refrigerant at different places in the loop at different pressures, the following has been assumed:

- The volumetric flow rate of the pump is always constant, set at $150\,\mathrm{mL/min}$.
- The lower limit of the thermal bath is $5\,^{\circ}\mathrm{C}$.
- The thermal conductivity of the rod is $380\,\mathrm{W/(m\,K)}$.
- The degree of subcooling desired is $3\,\mathrm{K}$.
- All thermal resistances and cross-sections are determined from the designed geometries.
- The pressure range for R245fa is $1\,\mathrm{bar}$–$4\,\mathrm{bar}$, for R717 this is $7\,\mathrm{bar}$–$20\,\mathrm{bar}$.
- The volumetric liquid flow needed for R245fa is $50\,\mathrm{mL/min}$, for R717 this is $15\,\mathrm{mL/min}$.
- The HTCs used are: $2.2\,\mathrm{kW/(m^2\,K)}$, $5.0\,\mathrm{kW/(m^2\,K)}$, $10.0\,\mathrm{kW/(m^2\,K)}$, $15.0\,\mathrm{kW/(m^2\,K)}$ and $25.0\,\mathrm{kW/(m^2\,K)}$.
- The wall of the test-section releasing heat to the coolant has the same temperature of the coolant. Thus, no fins are included in the model.
- The system has no losses.

Then, for every pressure, the saturation temperature is determined with CoolProp. And the temperature of the substrate is set to the saturation temperature minus the desired degree of subcooling: $T_{substrate} = T_{sat} - T_{subcooling}$.

The amount of heat transfer taking place equals:

$$\dot{Q} = HTC \times A \times T_{subcooling} \tag{A.13}$$

This allows for the determination for the desired coolant temperature, according to the total thermal resistance, the heat flow and the saturation temperature:

$$T_{coolant} = T_{sat} - \dot{Q} \sum R_{tot} \tag{A.14}$$

If the desired temperature of the coolant is lower than the limit, it is set to the limit. Then a new heat flow is determined according to a rewritten equation of the one above. This determines the new degree of subcooling, substrate temperature. Then, with the acquired heat flow, the measured temperature difference at the measurement points is determined according to Fourier's law of conduction:

$$\Delta T = \frac{\Delta L}{kA}\dot{Q} \tag{A.15}$$

Then, the state at all points (Figure 3.10) is determined, including the mass flow ($\dot{m}_i$), enthalpy (H_i), Temperature (T_i) and, if needed, heat input/rejection:

(1) After pump, fully liquid. The volumetric flow rate is set, this determines the mass flow based on the density. The temperature after the post-condenser is set to be the same as the coolant, that is here also the case. Enthalpy is based on temperature, mass flow and pressure.

(2A) After split, before saturation tank. The volumetric flow rate is iteratively determined. The temperature is the same as point 1, mass flow is determined based on density. Enthalpy is based on temperature, mass flow and pressure.

(2B) After split, recirculation loop. The volumetric flow rate is determined by the volumetric flow rate from the pump minus point 2A. The temperature is the same, mass flow rate based on density. Enthalpy is based on temperature, mass flow and pressure.

(3) After the saturation tank, before test-section, should only contain saturated vapour. Temperature is the saturation temperature according to the pressure. Mass flow rate is the same as at point 2A. Volumetric flow rate determined based on density of saturated vapour. Enthalpy based on pressure, mass flow and quality of saturated vapour.

(4) After test section, before joint. The enthalpy is based on the enthalpy of point 3, minus the amount of condensation taking place. The mass flow is the same as point 3. This allows for specific enthalpy calculation of point 3 and 4, to then determine the resulting vapour quality. The temperature is still at saturation conditions.

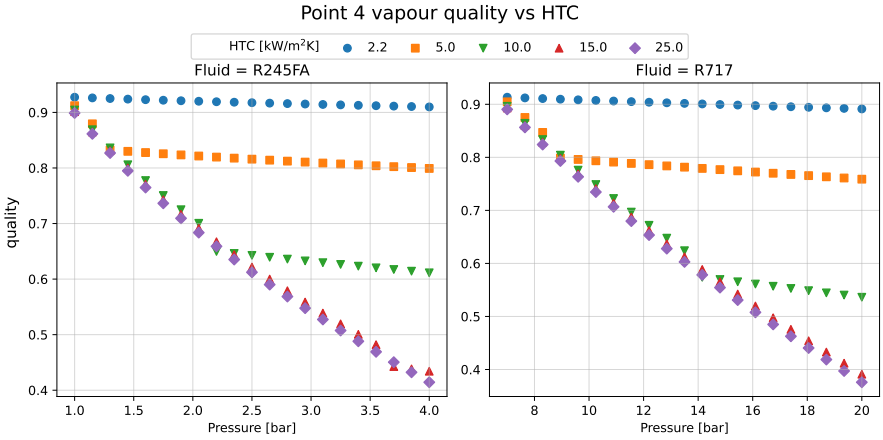

Figure A.9: Simulated vapour quality after the condensation chamber.

(5) After joint, before post-condenser. Because of mixing with cold (recirculation) liquid, the quality drops. The mass flow rate is the sum of point 2B and 4. The enthalpy is also summed, therefore the specific enthalpy is determined before the quality results. The temperature is determined by the pressure and the specific enthalpy.

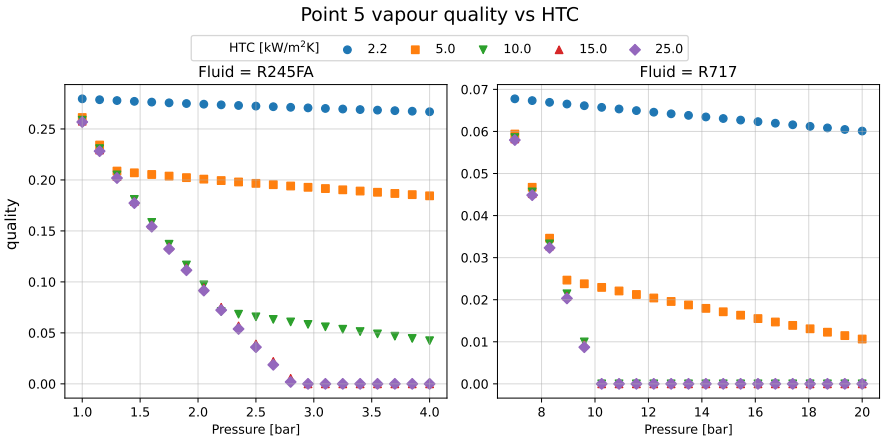

Figure A.10: Simulated vapour quality before entering the post-condenser.

(6) After post-condenser, before pump. The fluid is cooled down to the coolant temperature in the post-condenser due to the low flow rate. The mass flow rate is the same as point 5. The enthalpy is determined from the mass flow rate, pressure and temperature.

Evaporation heat input Because the fluid is not at saturation temperature yet, it first needs to be heated to this temperature (specific heat), then the latent heat of vapourisation needs to be supplied.

These are determined based on pressure. Then the temperature difference from subcooled to saturation conditions multiplied by the specific heat, then the latent heat is added. The result is then multiplied by the mass flow rate at point 3.

Post-condensor heat rejection This is the difference in total enthalpy in point 5 and 6.

B

Surfaces and contact angle measurements

Surface fabrication

The fabrication of the surfaces used has been done by Nanyang Technological University, Singapore. The fabrication procedure applied is listed below:

Cu-nano oxides: Initially, the as obtained Cu plates and tubes were cleaned by sonicating them sequentially in acetone (Sigma- Aldrich, CAS No. 6 4-6 4-1), ethanol (Sigma-Aldrich, CAS No. 6 4-17- 5) and isopropyl alcohol (Sigma-Aldrich, CAS No. 67-63-0) for $10\,\mathrm{min}$ at room temperature. After cleaning, the surfaces were thoroughly rinsed with deionized water (Sigma-Aldrich, CAS No. 7732-18-5) and dried with nitrogen. Subsequently, the samples were immersed in 2.0 M diluted hydrochloric acid (Sigma-Aldrich, CAS No. 7647-01-0) for $10\,\mathrm{min}$ to remove native oxides that were present on the surface and, thereafter, rinsed with deionized water and dried with nitrogen. The CuO nanostructure fabrication was carried out by immersing the cleaned copper samples for $15\,\mathrm{min}$ into a pool of alkaline solution maintained at $95(3)\,^{\circ}\mathrm{C}$. The alkaline solution consisted of a mixture of $3.75\,\mathrm{wt}\%$ NaClO 2 (Sigma-Aldrich, CAS No. 7758-19-2), $5\,\mathrm{wt}\%$ NaOH (Sigma-Aldrich, CAS No. 1310-73-2), $10\,\mathrm{wt}\%$ Na 3 PO 4 12H 2 O (Sigma-Aldrich, CAS No. 10101-89-0) and $100\,\mathrm{wt}\%$ deionized water.

Al-nano oxides: The specimens were first cleaned by deionized water, acetone (Sigma-Aldrich, CAS No. 64-64-1), ethanol (Sigma-Aldrich, CAS No. 64-17- 5) and isopropyl alcohol (Sigma-Aldrich, CAS No. 67-63-0) for $10\,\mathrm{min}$ each in an ultrasonic cleaner. Thereafter, the specimens were dried and immersed in a pool of hot deionized (DI) water at $95(5)\,^{\circ}\mathrm{C}$ for a duration of $1\,\mathrm{h}$. The hot water immersion process resulted in a self-limiting reaction of aluminum producing a thin layer of boehmite (γ-AlO(OH)) with needle-like structures having approximately $300\,\mathrm{nm}$ length scale.

Al-micro & nano oxides: The specimens were first cleaned by deionized water, acetone (Sigma-Aldrich, CAS No. 64-64-1), ethanol (Sigma-Aldrich, CAS No. 64-17- 5) and isopropyl alcohol (Sigma-Aldrich, CAS No. 67-63-0) for 10 min each in an ultrasonic cleaner. Thereafter, the specimens were dried and immersed in a pool of diluted (2M) hydrochloric acid (HCl) (Sigma-Aldrich CAS No. 7647-01-0) for $15\,\mathrm{min}$ at room temperature of $25\,^{\circ}\mathrm{C}$. After the HCl immersion process, the Al6061B treatment process was applied on this specimen.

All surfaces are then infused with Krytox VFP 1525 lubricant.

Static experimental results with Water

Table B.1: Mean static contact angle results of water on experimental surfaces.

Measurement	Substrate	CA left	CA Mean	CA right
1	Cu-nano	115.62°	115.51°	115.40°
2	Cu-nano	118.98°	118.99°	118.99°
3	Cu-nano	118.04°	117.99°	117.95°
4	Cu-nano	118.31°	118.26°	118.21°
5	Cu-nano	118.07°	118.06°	118.04°
1	Alu-nano	118.95°	118.87°	118.80°
2	Alu-nano	118.91°	118.94°	118.97°
3	Alu-nano	121.64°	121.62°	121.61°
4	Alu-nano	120.93°	120.74°	120.54°
5	Alu-nano	117.05°	117.02°	116.99°
1	Alu-micro & nano	106.13°	106.09°	106.06°
2	Alu-micro & nano	106.84°	106.77°	106.70°
3	Alu-micro & nano	109.56°	109.49°	109.41°
4	Alu-micro & nano	111.61°	111.59°	111.58°
5	Alu-micro & nano	111.67°	111.34°	111.02°

Dynamic experimental results with water

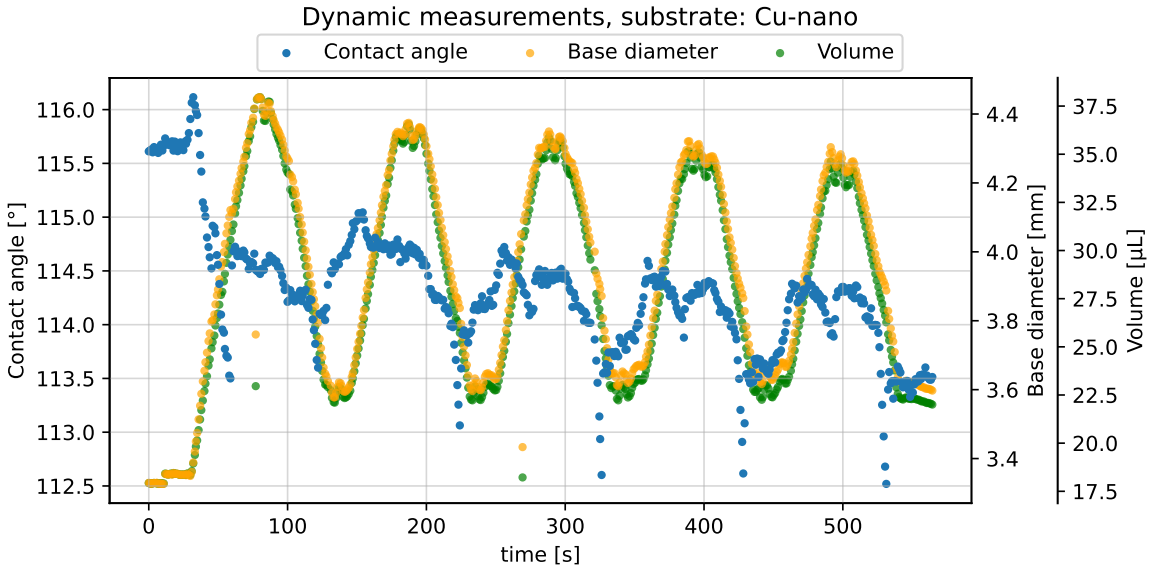

Figure B.1: Cu-nano: Raw dynamic contact angle measurements.

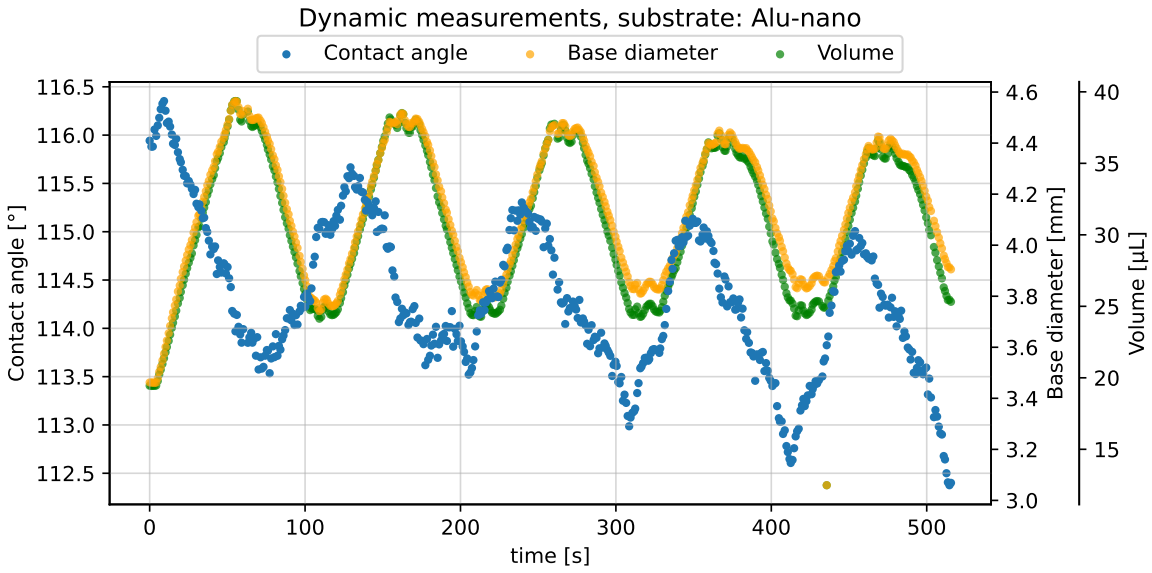

Figure B.2: Alu-nano: Raw dynamic contact angle measurements.

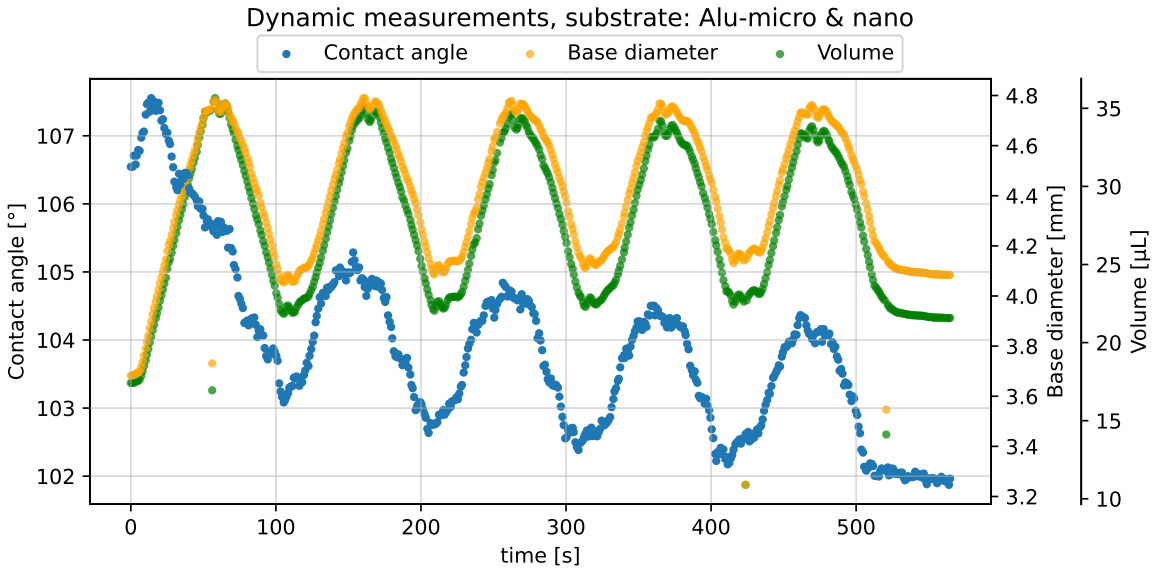

Figure B.3: Alu-micro & nano: Raw dynamic contact angle measurements.

C

Computational geometry verification

Boundary conditions calculations

Meshing settings

The following settings for mesh generation in the geometry were used:

- Physics Preference: Mechanical
- Element Order: Second order (quadratic)
- Element Size: $5 \times 10^{-2}\,\mathrm{m}$, $1 \times 10^{-2}\,\mathrm{m}$ and $5 \times 10^{-3}\,\mathrm{m}$
- Use Adaptive sizing: Yes
- Resolution: 3
- Mesh Defeaturing: Yes
- Defeature Size: Default
- Transition: Fast
- Span Angle Center: Coarse
- Initial Size Seed: Assembly
- Check Mesh Quality: Yes, Errors
- Error Limits: Aggressive Mechanical
- Target Element Quality: Default (5×10^{-2})
- Smoothing: Medium
- Mesh Metric: None
- Use Automatic Inflation: None
- Inflation Option: Smooth Transition
- Transition Ration: 0.272
- Maximum Layers: 5
- Growth Rate: 1.2
- Inflation Algorithm: Pre
- Inflation Element Type: Wedges
- Sheet Body Method: Prime Quad Dominant
- Sweepable Body Method: Sweep

Meshing result

Table C.1: Meshing element results for different meshing sizing settings.

Property	Normal mesh	Coarse mesh	Fine mesh
Element size	1×10^{-2} m	2×10^{-2} m	5×10^{-3} m
Nodes	3723	2266	12 769
Elements	1722	976	6705
Corner nodes	683	436	2147
Mid nodes	3040	1830	10 622
Solid elements	1722	976	6705
Tet10	1722	976	6705

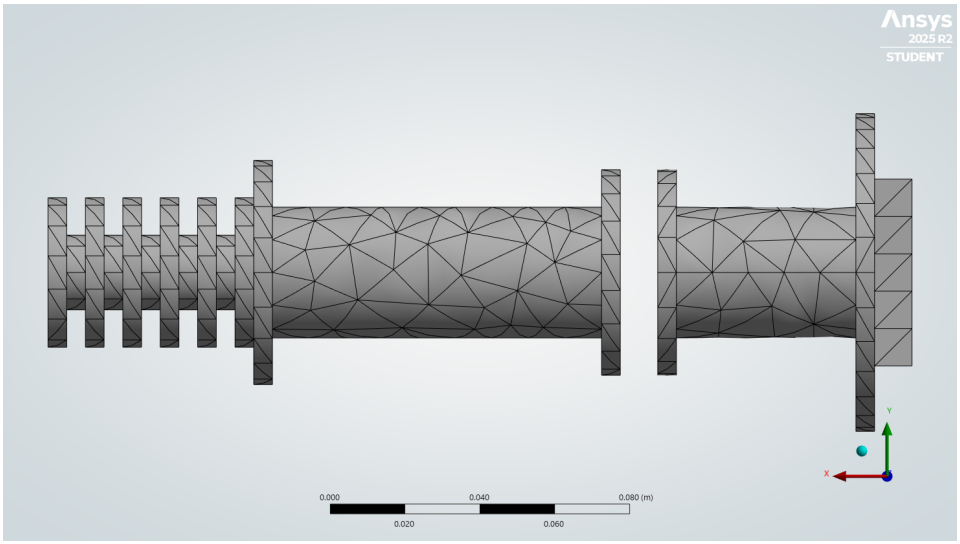

Figure C.1: Base meshing.

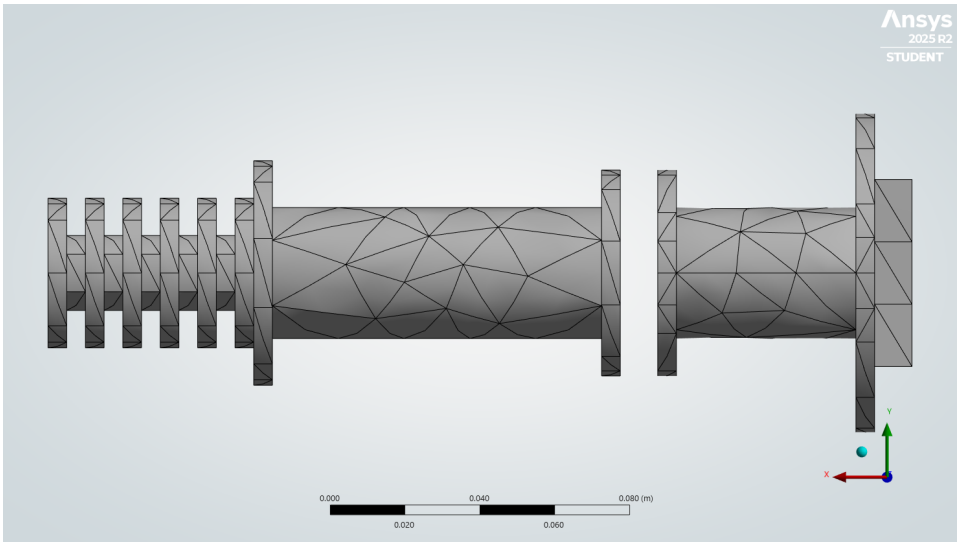

Figure C.2: Coarse meshing

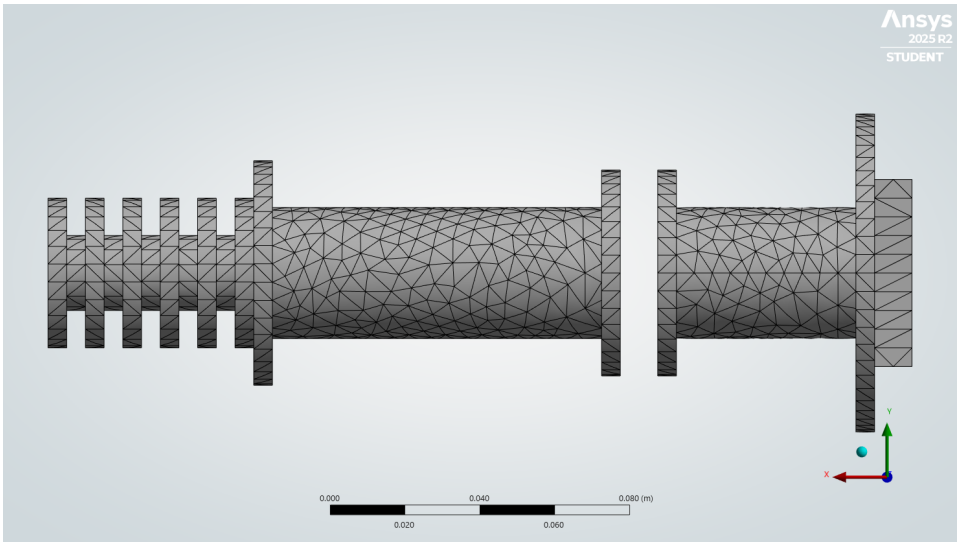

Figure C.3: Fine meshing

Temperature profile results

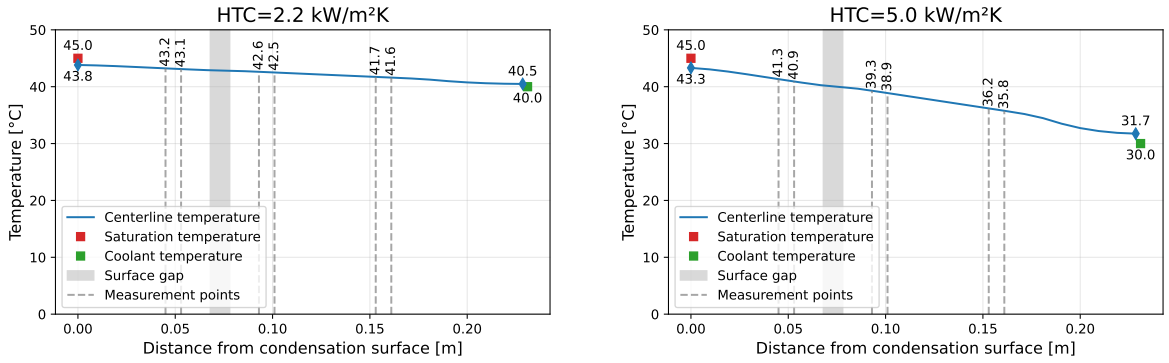

Figure C.4: Centreline temperature profile at different HTCs and corresponding desired coolant temperatures. Also, the temperatures at the measurement points are shown. (part 1)

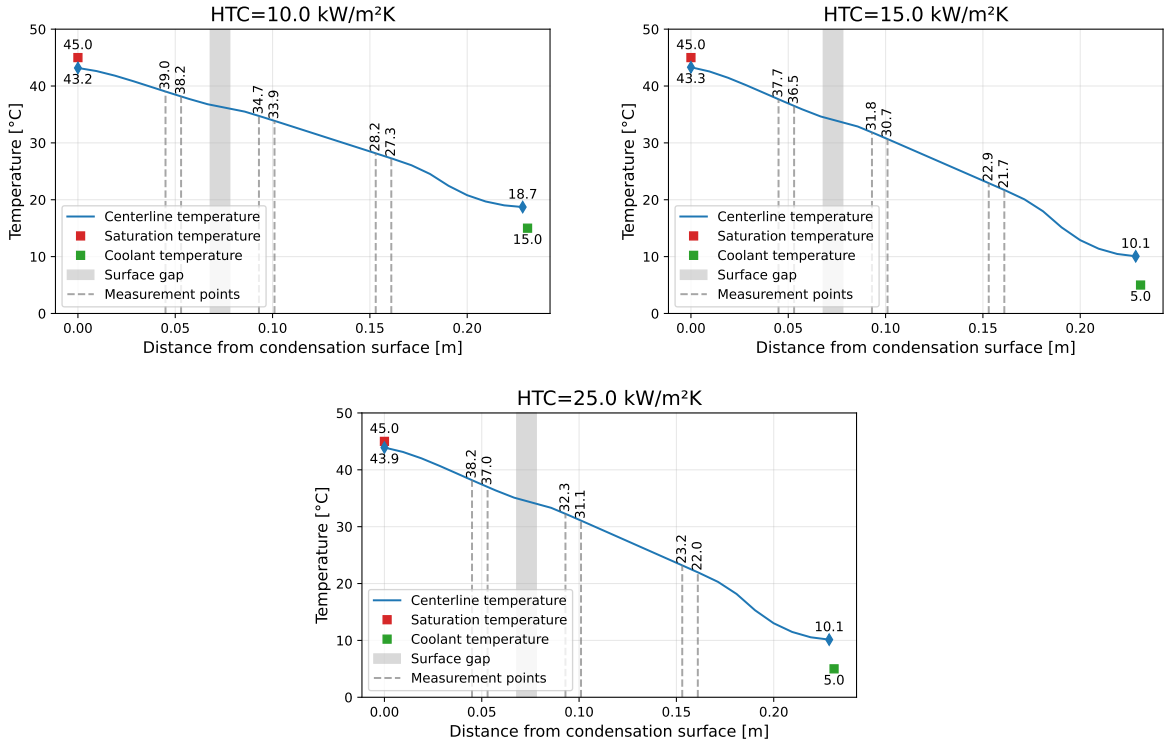

Figure C.4: Centreline temperature profile at different HTCs and corresponding desired coolant temperatures. Also, the temperatures at the measurement points are shown. (continued)

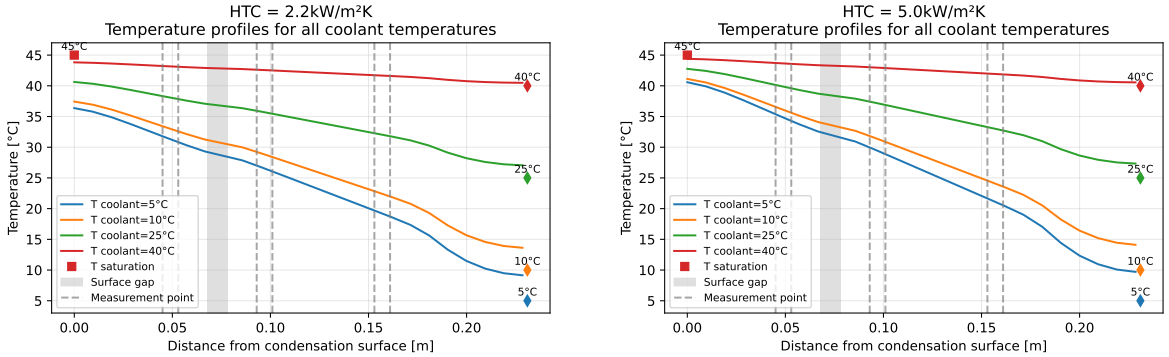

Figure C.5: Centreline temperature profile at different HTCs and coolant temperatures. (part 1)

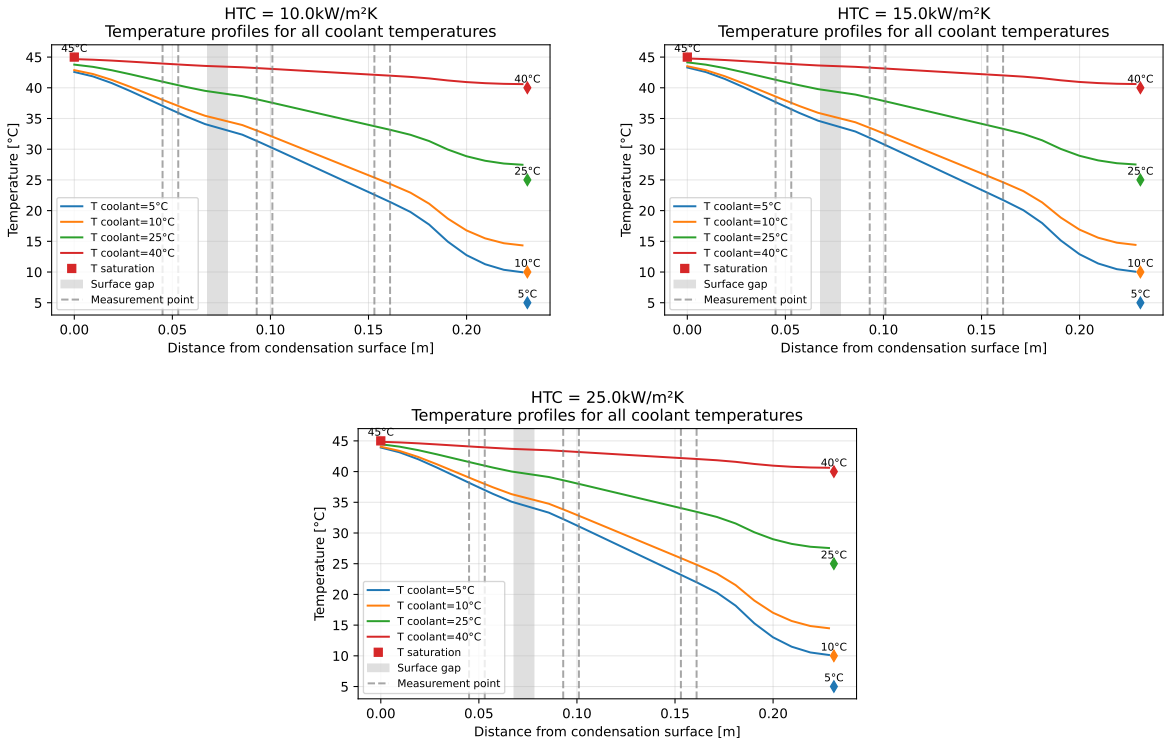

Figure C.5: Centreline temperature profile at different HTCs and coolant temperatures. (continued)

D

Estimation function and uncertainty analysis

Functions in determining the HTC and their uncertainty

Total heat transfer

$$\dot{Q} = \frac{1}{4}\left(\dot{Q}_{3,5} + \dot{Q}_{4,6} + \dot{Q}_{4,5} + \dot{Q}_{3,6}\right) \tag{D.1}$$

$$u^2(\dot{Q}) = \frac{1}{16}\left(u^2(\dot{Q}_{3,5}) + u^2(\dot{Q}_{4,6}) + u^2(\dot{Q}_{4,5}) + u^2(\dot{Q}_{3,6})\right) \tag{D.2}$$

$$\dot{Q}_{a,b} = \frac{kA}{L_{a,b}}\left(T_a - T_b\right) \tag{D.3}$$

$$u^2(\dot{Q}_{a,b}) = \left(\frac{\partial \dot{Q}_{a,b}}{\partial T_a}\right)^2 u^2(T_a) + \left(\frac{\partial \dot{Q}_{a,b}}{\partial T_b}\right)^2 u^2(T_b) + \left(\frac{\partial \dot{Q}_{a,b}}{\partial L_{a,b}}\right)^2 u^2(L_{a,b}) \tag{D.4}$$

(Condensation) Wall temperature

$$T_w = \frac{T_{w,1} + T_{w,2}}{2} \tag{D.5}$$

$$u^2(T_w) = \frac{1}{4}\left(u^2(T_{w,1}) + u^2(T_{w,2})\right) \tag{D.6}$$

for i equals 1 and 2

$$T_{w,i} = \frac{\dot{Q}L_i}{kA} + T_i \tag{D.7}$$

$$u^2(T_{w,i}) = \left(\frac{\partial T_{w,i}}{\partial L_i}\right)^2 u^2(L_i) + \left(\frac{\partial T_{w,i}}{\partial \dot{Q}}\right)^2 u^2(\dot{Q}) + \left(\frac{\partial T_{w,i}}{\partial T_i}\right)^2 u^2(T_i) \tag{D.8}$$

Saturation temperature

$$T_{sat,P} = T(P) \tag{D.9}$$

$$u^2(T_{sat,p}) = \left(\frac{\partial T_{sat,P}}{\partial P}\right)^2 u^2(P) \tag{D.10}$$

$$\frac{\partial T(P)}{\partial P} = \frac{T(P+\varepsilon) - T(P-\varepsilon)}{2\varepsilon} \tag{D.11}$$

$$T_{sat,T} = T_7 \tag{D.12}$$

$$u^2(T_{sat,T}) = u^2(T_7) \tag{D.13}$$

HTC Here, the HTC is estimated on T_{sat} of both the pressure ($T_{sat,P}$) and the temperature reading ($T_{sat,T}$).

$$HTC = \frac{\dot{Q}}{A\left(T_{sat} - T_w\right)} \tag{D.14}$$

$$u^2(HTC) = \left(\frac{\partial HTC}{\partial \dot{Q}}\right)^2 u^2(\dot{Q}) + \left(\frac{\partial HTC}{\partial T_{sat}}\right)^2 u^2(T_{sat}) + \left(\frac{\partial HTC}{\partial T_w}\right)^2 u^2(T_w) \tag{D.15}$$